

Advances in Civil Engineering

# Multi-Field Coupling and Deep Engineering Safety: New Theories and Methods 2022

Lead Guest Editor: Guang-Liang Feng

Guest Editors: Quan Jiang and Jun Xiong





---

**Multi-Field Coupling and Deep Engineering  
Safety: New Theories and Methods 2022**

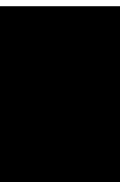
Advances in Civil Engineering

---

**Multi-Field Coupling and Deep  
Engineering Safety: New Theories and  
Methods 2022**

Lead Guest Editor: Guang-Liang Feng

Guest Editors: Quan Jiang and Jun Xiong



---

Copyright © 2023 Hindawi Limited. All rights reserved.

This is a special issue published in "Advances in Civil Engineering." All articles are open access articles distributed under the Creative Commons Attribution License, which permits unrestricted use, distribution, and reproduction in any medium, provided the original work is properly cited.


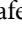
# Chief Editor

Cumaraswamy Vipulanandan, USA










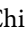



## Associate Editors

Chiara Bedon , Italy  
Constantin Chalioris , Greece  
Ghassan Chehab , Lebanon  
Ottavia Corbi, Italy  
Mohamed ElGawady , USA  
Husnain Haider , Saudi Arabia  
Jian Ji , China  
Jiang Jin , China  
Shazim A. Memon , Kazakhstan  
Hossein Moayedi , Vietnam  
Sanjay Nimbalkar, Australia  
Giuseppe Oliveto , Italy  
Alessandro Palmeri , United Kingdom  
Arnaud Perrot , France  
Hugo Rodrigues , Portugal  
Victor Yepes , Spain  
Xianbo Zhao , Australia

## Academic Editors

José A.F.O. Correia, Portugal  
Glenda Abate, Italy  
Khalid Abdel-Rahman , Germany  
Ali Mardani Aghabaglou, Turkey  
José Aguiar , Portugal  
Afaq Ahmad , Pakistan  
Muhammad Riaz Ahmad , Hong Kong  
Hashim M.N. Al-Madani , Bahrain  
Luigi Aldieri , Italy  
Angelo Aloisio , Italy  
Maria Cruz Alonso, Spain  
Filipe Amarante dos Santos , Portugal  
Serji N. Amirkhanean, USA  
Eleftherios K. Anastasiou , Greece  
Panagiotis Ch. Anastasopoulos , USA  
Mohamed Moafak Arbili , Iraq  
Farhad Aslani , Australia  
Siva Avudaiappan , Chile  
Ozgur BASKAN , Turkey  
Adewumi Babafemi, Nigeria  
Morteza Bagherpour, Turkey  
Qingsheng Bai , Germany  
Nicola Baldo , Italy  
Daniele Baraldi , Italy

Eva Barreira , Portugal  
Emilio Bastidas-Arteaga , France  
Rita Bento, Portugal  
Rafael Bergillos , Spain  
Han-bing Bian , China  
Xia Bian , China  
Huseyin Bilgin , Albania  
Giovanni Biondi , Italy  
Hugo C. Biscaia , Portugal  
Rahul Biswas , India  
Edén Bojórquez , Mexico  
Giosuè Boscato , Italy  
Melina Bosco , Italy  
Jorge Branco , Portugal  
Bruno Briseghella , China  
Brian M. Broderick, Ireland  
Emanuele Brunesi , Italy  
Quoc-Bao Bui , Vietnam  
Tan-Trung Bui , France  
Nicola Buratti, Italy  
Gaochuang Cai, France  
Gladis Camarini , Brazil  
Alberto Campisano , Italy  
Qi Cao, China  
Qixin Cao, China  
Iacopo Carnacina , Italy  
Alessio Cascardi, Italy  
Paolo Castaldo , Italy  
Nicola Cavalagli , Italy  
Liborio Cavaleri , Italy  
Anush Chandrappa , United Kingdom  
Wen-Shao Chang , United Kingdom  
Muhammad Tariq Amin Chaudhary, Kuwait  
Po-Han Chen , Taiwan  
Qian Chen , China  
Wei Tong Chen , Taiwan  
Qixiu Cheng, Hong Kong  
Zhanbo Cheng, United Kingdom  
Nicholas Chileshe, Australia  
Prinya Chindaprasirt , Thailand  
Corrado Chisari , United Kingdom  
Se Jin Choi , Republic of Korea  
Heap-Yih Chong , Australia  
S.H. Chu , USA  
Ting-Xiang Chu , China

Zhaofei Chu , China  
Wonseok Chung , Republic of Korea  
Donato Ciampa , Italy  
Gian Paolo Cimellaro, Italy  
Francesco Colangelo, Italy  
Romulus Costache , Romania  
Liviu-Adrian Cotfas , Romania  
Antonio Maria D'Altri, Italy  
Bruno Dal Lago , Italy  
Amos Darko , Hong Kong  
Arka Jyoti Das , India  
Dario De Domenico , Italy  
Gianmarco De Felice , Italy  
Stefano De Miranda , Italy  
Maria T. De Risi , Italy  
Tayfun Dede, Turkey  
Sadik O. Degertekin , Turkey  
Camelia Delcea , Romania  
Cristoforo Demartino, China  
Giuseppe Di Filippo , Italy  
Luigi Di Sarno, Italy  
Fabio Di Trapani , Italy  
Aboelkasim Diab , Egypt  
Thi My Dung Do, Vietnam  
Giulio Dondi , Italy  
Jiangfeng Dong , China  
Chao Dou , China  
Mario D'Aniello , Italy  
Jingtao Du , China  
Ahmed Elghazouli, United Kingdom  
Francesco Fabbrocino , Italy  
Flora Faleschini , Italy  
Dingqiang Fan, Hong Kong  
Xueping Fan, China  
Qian Fang , China  
Salar Farahmand-Tabar , Iran  
Ilenia Farina, Italy  
Roberto Fedele, Italy  
Guang-Liang Feng , China  
Luigi Fenu , Italy  
Tiago Ferreira , Portugal  
Marco Filippo Ferrotto, Italy  
Antonio Formisano , Italy  
Guoyang Fu, Australia  
Stefano Galassi , Italy

Junfeng Gao , China  
Meng Gao , China  
Giovanni Garcea , Italy  
Enrique García-Macías, Spain  
Emilio García-Taengua , United Kingdom  
DongDong Ge , USA  
Khaled Ghaedi, Malaysia  
Khaled Ghaedi , Malaysia  
Gian Felice Giaccu, Italy  
Agathoklis Giaralis , United Kingdom  
Ravindran Gobinath, India  
Rodrigo Gonçalves, Portugal  
Peilin Gong , China  
Belén González-Fonteboa , Spain  
Salvatore Grasso , Italy  
Fan Gu, USA  
Erhan Güneyisi , Turkey  
Esra Mete Güneyisi, Turkey  
Pingye Guo , China  
Ankit Gupta , India  
Federico Gusella , Italy  
Kemal Hacıfendioglu, Turkey  
Jianyong Han , China  
Song Han , China  
Asad Hanif , Macau  
Hadi Hasanzadehshooiili , Canada  
Mostafa Fahmi Hassanein, Egypt  
Amir Ahmad Hedayat , Iran  
Khandaker Hossain , Canada  
Zahid Hossain , USA  
Chao Hou, China  
Biao Hu, China  
Jiang Hu , China  
Xiaodong Hu, China  
Lei Huang , China  
Cun Hui , China  
Bon-Gang Hwang, Singapore  
Jijo James , India  
Abbas Fadhil Jasim , Iraq  
Ahad Javanmardi , China  
Krishnan Prabhakan Jaya, India  
Dong-Sheng Jeng , Australia  
Han-Yong Jeon, Republic of Korea  
Pengjiao Jia, China  
Shaohua Jiang , China

MOUSTAFA KASSEM , Malaysia  
Mosbeh Kaloop , Egypt  
Shankar Karuppannan , Ethiopia  
John Kechagias , Greece  
Mohammad Khajehzadeh , Iran  
Afzal Husain Khan , Saudi Arabia  
Mehran Khan , Hong Kong  
Manoj Khandelwal, Australia  
Jin Kook Kim , Republic of Korea  
Woosuk Kim , Republic of Korea  
Vaclav Koci , Czech Republic  
Loke Kok Foong, Vietnam  
Hailing Kong , China  
Leonidas Alexandros Kouris , Greece  
Kyriakos Kourousis , Ireland  
Moacir Kripka , Brazil  
Anupam Kumar, The Netherlands  
Emma La Malfa Ribolla, Czech Republic  
Ali Lakirouhani , Iran  
Angus C. C. Lam, China  
Thanh Quang Khai Lam , Vietnam  
Luciano Lamberti, Italy  
Andreas Lampropoulos , United Kingdom  
Raffaele Landolfo, Italy  
Massimo Latour , Italy  
Bang Yeon Lee , Republic of Korea  
Eul-Bum Lee , Republic of Korea  
Zhen Lei , Canada  
Leonardo Leonetti , Italy  
Chun-Qing Li , Australia  
Dongsheng Li , China  
Gen Li, China  
Jiale Li , China  
Minghui Li, China  
Qingchao Li , China  
Shuang Yang Li , China  
Sunwei Li , Hong Kong  
Yajun Li , China  
Shun Liang , China  
Francesco Liguori , Italy  
Jae-Han Lim , Republic of Korea  
Jia-Rui Lin , China  
Kun Lin , China  
Shibin Lin, China

Tzu-Kang Lin , Taiwan  
Yu-Cheng Lin , Taiwan  
Hexu Liu, USA  
Jian Lin Liu , China  
Xiaoli Liu , China  
Xuemei Liu , Australia  
Zaobao Liu , China  
Zhuang-Zhuang Liu, China  
Diego Lopez-Garcia , Chile  
Cristiano Loss , Canada  
Lyan-Ywan Lu , Taiwan  
Jin Luo , USA  
Yanbin Luo , China  
Jianjun Ma , China  
Junwei Ma , China  
Tian-Shou Ma, China  
Zhongguo John Ma , USA  
Maria Macchiaroli, Italy  
Domenico Magisano, Italy  
Reza Mahinroosta, Australia  
Yann Malecot , France  
Prabhat Kumar Mandal , India  
John Mander, USA  
Iman Mansouri, Iran  
André Dias Martins, Portugal  
Domagoj Matesan , Croatia  
Jose Matos, Portugal  
Vasant Matsagar , India  
Claudio Mazzotti , Italy  
Ahmed Mebarki , France  
Gang Mei , China  
Kasim Mermerdas, Turkey  
Giovanni Minafò , Italy  
Masoomah Mirrashid , Iran  
Abbas Mohajerani , Australia  
Fadzli Mohamed Nazri , Malaysia  
Fabrizio Mollaioli , Italy  
Rosario Montuori , Italy  
H. Naderpour , Iran  
Hassan Nasir , Pakistan  
Hossein Nassiraei , Iran  
Satheeskumar Navaratnam , Australia  
Ignacio J. Navarro , Spain  
Ashish Kumar Nayak , India  
Behzad Nematollahi , Australia

Chayut Ngamkhanong , Thailand  
Trung Ngo, Australia  
Tengfei Nian, China  
Mehdi Nikoo , Canada  
Youjun Ning , China  
Olugbenga Timo Oladinrin , United Kingdom  
Oladimeji Benedict Olalusi, South Africa  
Timothy O. Olawumi , Hong Kong  
Alejandro Orfila , Spain  
Maurizio Orlando , Italy  
Siti Aminah Osman, Malaysia  
Walid Oueslati , Tunisia  
SUVASH PAUL , Bangladesh  
John-Paris Pantouvakis , Greece  
Fabrizio Paolacci , Italy  
Giuseppina Pappalardo , Italy  
Fulvio Parisi , Italy  
Dimitrios G. Pavlou , Norway  
Daniele Pellegrini , Italy  
Gatheeshgar Perampalam , United Kingdom  
Daniele Perrone , Italy  
Giuseppe Piccardo , Italy  
Vagelis Plevris , Qatar  
Andrea Pranno , Italy  
Adolfo Preciado , Mexico  
Chongchong Qi , China  
Yu Qian, USA  
Ying Qin , China  
Giuseppe Quaranta , Italy  
Krishanu ROY , New Zealand  
Vlastimir Radonjanin, Serbia  
Carlo Rainieri , Italy  
Rahul V. Ralegaonkar, India  
Raizal Saifulnaz Muhammad Rashid, Malaysia  
Alessandro Rasulo , Italy  
Chonghong Ren , China  
Qing-Xin Ren, China  
Dimitris Rizos , USA  
Geoffrey W. Rodgers , New Zealand  
Pier Paolo Rossi, Italy  
Nicola Ruggieri , Italy  
JUNLONG SHANG, Singapore

Nikhil Saboo, India  
Anna Saetta, Italy  
Juan Sagaseta , United Kingdom  
Timo Saksala, Finland  
Mostafa Salari, Canada  
Ginevra Salerno , Italy  
Evangelos J. Sapountzakis , Greece  
Vassilis Sarhosis , United Kingdom  
Navaratnarajah Sathiparan , Sri Lanka  
Fabrizio Scozzese , Italy  
Halil Sezen , USA  
Payam Shafigh , Malaysia  
M. Shahria Alam, Canada  
Yi Shan, China  
Hussein Sharaf, Iraq  
Mostafa Sharifzadeh, Australia  
Sanjay Kumar Shukla, Australia  
Amir Si Larbi , France  
Okan Sirin , Qatar  
Piotr Smarzewski , Poland  
Francesca Sollecito , Italy  
Rui Song , China  
Tian-Yi Song, Australia  
Flavio Stochino , Italy  
Mayank Sukhija , USA  
Piti Sukontasukkul , Thailand  
Jianping Sun, Singapore  
Xiao Sun , China  
T. Tafsirojjaman , Australia  
Fujiao Tang , China  
Patrick W.C. Tang , Australia  
Zhi Cheng Tang , China  
Weerachart Tangchirapat , Thailand  
Xiixin Tao, China  
Piergiorgio Tataranni , Italy  
Elisabete Teixeira , Portugal  
Jorge Iván Tobón , Colombia  
Jing-Zhong Tong, China  
Francesco Trentadue , Italy  
Antonello Troncone, Italy  
Majbah Uddin , USA  
Tariq Umar , United Kingdom  
Muahmmad Usman, United Kingdom  
Muhammad Usman , Pakistan  
Mucteba Uysal , Turkey



Ilaria Venanzi , Italy  
Castorina S. Vieira , Portugal  
Valeria Vignali , Italy  
Claudia Vitone , Italy  
Liwei WEN , China  
Chunfeng Wan , China  
Hua-Ping Wan, China  
Roman Wan-Wendner , Austria  
Chaohui Wang , China  
Hao Wang , USA  
Shiming Wang , China  
Wayne Yu Wang , United Kingdom  
Wen-Da Wang, China  
Xing Wang , China  
Xiuling Wang , China  
Zhenjun Wang , China  
Xin-Jiang Wei , China  
Tao Wen , China  
Weiping Wen , China  
Lei Weng , China  
Chao Wu , United Kingdom  
Jiangyu Wu, China  
Wangjie Wu , China  
Wenbing Wu , China  
Zhixing Xiao, China  
Gang Xu, China  
Jian Xu , China  
Panpan , China  
Rongchao Xu , China  
HE YONGLIANG, China  
Michael Yam, Hong Kong  
Hailu Yang , China  
Xu-Xu Yang , China  
Hui Yao , China  
Xinyu Ye , China  
Zhoujing Ye, China  
Gürol Yildirim , Turkey  
Dawei Yin , China  
Doo-Yeol Yoo , Republic of Korea  
Zhanping You , USA  
Afshar A. Yousefi , Iran  
Xinbao Yu , USA  
Dongdong Yuan , China  
Geun Y. Yun , Republic of Korea

Hyun-Do Yun , Republic of Korea  
Cemal YİĞİT , Turkey  
Paolo Zampieri, Italy  
Giulio Zani , Italy  
Mariano Angelo Zanini , Italy  
Zhixiong Zeng , Hong Kong  
Mustafa Zeybek, Turkey  
Henglong Zhang , China  
Jiupeng Zhang, China  
Tingting Zhang , China  
Zengping Zhang, China  
Zetian Zhang , China  
Zhigang Zhang , China  
Zhipeng Zhao , Japan  
Jun Zhao , China  
Annan Zhou , Australia  
Jia-wen Zhou , China  
Hai-Tao Zhu , China  
Peng Zhu , China  
QuanJie Zhu , China  
Wenjun Zhu , China  
Marco Zucca, Italy  
Haoran Zuo, Australia  
Junqing Zuo , China  
Robert Černý , Czech Republic  
Süleyman İpek , Turkey

# Contents


---

**Investigation on Mining-Induced Floor Water Inrush from Column and Its Control Based on Microseismic Monitoring**

Run Liu, Guojun Zhi, Shilei Yang, and Xiaowei Xu 


Research Article (16 pages), Article ID 3754079, Volume 2023 (2023)

**Progressive Failure of Surrounding Rock in Underground Engineering and Size Effect of Numerical Simulation**

Daning Zhong , Jianlin Chen, Hui Zhou , Xiangrong Chen, and Yali Jiang

Research Article (12 pages), Article ID 9454079, Volume 2023 (2023)

**Experimental Study on Dynamic Compression Mechanics of Sandstone after Coupled Alkali-Chemical-Dynamic Interaction**

Qi Ping , Chen Wang, Qi Gao, Kaifan Shen, Yulin Wu, Shuo Wang, and Xiangyang Li

Research Article (10 pages), Article ID 1970591, Volume 2022 (2022)

**Study on Strength Enhancement Factors of Cement-Stabilized Recycled Aggregate**

Congcong Su  and Lihui Li 

Research Article (11 pages), Article ID 9997483, Volume 2022 (2022)

## Research Article

# Investigation on Mining-Induced Floor Water Inrush from Column and Its Control Based on Microseismic Monitoring

Run Liu,<sup>1,2</sup> Guojun Zhi,<sup>1</sup> Shilei Yang,<sup>1</sup> and Xiaowei Xu <sup>2</sup>

<sup>1</sup>Wanli No. 1 Coal Mine, Shenhua Baotou Energy Company with Limited Liability, Eerduosi 017000, Neimenggu, China

<sup>2</sup>School of Mechanics and Civil Engineering, University of Mining and Technology, Beijing 100083, China

Correspondence should be addressed to Xiaowei Xu; xxw@student.cumtb.edu.cn

Received 27 August 2022; Revised 14 December 2022; Accepted 15 April 2023; Published 20 May 2023

Academic Editor: Guang-Liang Feng

Copyright © 2023 Run Liu et al. This is an open access article distributed under the Creative Commons Attribution License, which permits unrestricted use, distribution, and reproduction in any medium, provided the original work is properly cited.

Water inrush is the biggest threat for safe mining in the Ruifeng coalmine, located in North China. In the study mining area, the floor water inrush is mainly caused by mining activities and collapse column. In this article, the mechanical criteria of floor water inrush are obtained based on cusp catastrophe theory, which is used to assess floor water inrush risk in the Ruifeng coalmine. Theoretical analysis shows that floor water inrush is very likely to occur during coal mining without the influence of geological structures. Additionally, FLAC<sup>3D</sup> was used to simulate the damage of floor strata during the mining face advances. Numerical results show that the water inrush channel occurs in front of the mining face due to the influence of stress concentration. Therefore, a microseismic monitoring system was applied to monitor the formation of water inrush pathway. Field monitoring results show that two water inrush pathways were accurately predicted and positioned. Based on the microseismic monitoring results, target grouting was adopted to prevent water inrush. This study provides significant guidance for the prevention of floor water inrush.

## 1. Introduction

Most coalmines located in the Permo-Carboniferous coalfields in North China are threatened by the Ordovician limestone aquifer under the coal seams [1–3]. The Ordovician limestone strata are confined aquifer containing a large amount of water with a high hydraulic pressure [4]. The floor strata between the confined aquifer and the coal seam, normally comprising mixed impermeable clay layers with high strength sandstone or carbonate layers, can serve as the water-resisting strata that prevent the upward migration of confined water. But the water-resisting strata are relatively thin and usually damaged by the geological structures, such as faults and collapse columns. Furthermore, the water-resisting strata may break under the combined action of hydraulic and mining-induced pressures during coal mining above the aquifer. And a dramatic increase in permeability may occur in the broken water-resisting floor strata and finally result in water bursting into mining excavations [5, 6]. Water inrush hazard not only

leads to grievous casualties and heavy economic losses for coal mines but also seriously pose a potential threat to society stability [7–14]. According to incomplete official statistics, about 285 major coalmines involve a risk of water inrush in China, which approximately accounts for 47.5% of all state-owned coalmines [15]. And more than 473 water inrush hazards have occurred in the past two decades killing 2635 workers [16]. Therefore, the study of prediction and prevention on floor water inrush has important practical significance.

In recent decades, many researches on floor water inrush mechanism have been conducted. A few empirical criteria and models, such as the water inrush index, hypothesis of three zones in floor strata, and floor key strata model, have been proposed for predicting water inrushes [1, 14, 17–21]. These studies played an important role in evaluating the risk of water inrush hazards in engineering practice. However, there is a lack of methods to accurately predict and prevent water inrush hazards in a timely manner [22]. This has limited our ability to address the crucial issue for safer

mining above confined aquifers. After coal mining, the redistribution of stress field may result in a fractured zone with high conductivity in the floor strata, which provides a pathway for confined water inflow [23–25].

In general, the formation of water inrush pathway is directly related to the fracture of floor rock strata, which induces a series of microseismic to occur [26]. Currently, microseismic has been widely used to monitor the rock failure process in landslide, coal and gas outbursts, and coal bumps and predict these hazards [27–31]. However, microseismic was seldom applied to monitor the formation process of water inrush pathway, which is a requirement of water inrush. In this article, the mechanics criteria of floor water inrush are derived based on cusp catastrophe theory and the criteria are utilized to assess floor water inrush risk in the Ruifeng coalmine. Floor water inrush is more likely to occur during mining because the geological structures are complex in the study area. Therefore, ESG microseismic monitoring system was applied to monitor the formation process of water inrush pathway, which provides an important guide for the prevention of water inrush. The field monitoring results show that two water inrush pathways were accurately positioned. Then, two targeted grouting holes were drilled from the ground surface and the water inrush was effectively prevented by injecting 900 tons of cement slurry. This provides significant guidance for safe coal excavation above confined aquifers.

## 2. General Situation of the Study Area

Ruifeng coalmine located in Handan-Xingtai mining area of North China is severely threatened by water inrush hazards. In Handan-Xingtai mining area, more than 10 collieries involve the risk of water bursting into the mining excavation through fractured floor strata and more than 30 heavy water inrush hazards occurred in the past, as shown in Figure 1 and Table 1. The main influencing factors causing water inrush are collapse columns, faults, and mining. As can be seen from Figure 1 and Table 1, 14 water inrush hazards were caused by faults which accounted for forty-seven percent and 11 water inrush hazards were caused by collapse columns which accounted for thirty-seven percent. Besides, 2 water inrush hazards were caused by the combined action of faults and collapse columns and other 2 water inrush hazards were caused by floor failure due to mining. Furthermore, the most serious water inrush accident occurred on April 12, 2003 in the Dongpang coalmine and the maximum water inrush rate was 70000 m<sup>3</sup>/h, which caused the coalmine to submerge, and there were a large number of casualties. Therefore, geological structures, mainly including insidious faults and collapse columns, are the main influencing factors of water inrush in Handan-Xingtai mining area.

In the Ruifeng coalmine, there are Ordovician limestone strata under the No. 5 coal seam, which contains a large amount of water with a 1.33~1.73 MPa pressure. The average thickness of No. 5 coal seam is about 8.0 m and is located in the level at a depth of -460 m. The distance between Ordovician limestone strata and No. 5 coal seam is about 49 m. More than 30 collapse columns have been exposed during

the past mining. There are three main faults and two collapse columns in the study area, as shown in Figure 1. Besides, a total of 17 water inrush hazards have occurred in the past. The most serious water inrush occurred in 1942 and the maximum water inrush rate was about 4080 m<sup>3</sup>/h, causing the coalmine to submerge in half an hour.

## 3. Risk Assessment of Floor Water Inrush Based on the Cusp Catastrophe Theory

In order to reduce floor water inrush hazards, the vulnerability assessment of floor aquifuge is necessary [32, 33]. The roof caving did not occur behind the mining face within a certain range. Therefore, the unloading failure of floor aquifuge happens, which may cause floor water inrush.

Simplifying the unbroken floor aquifuge as a rock beam, as shown in Figure 2, the length of the rock beam is equal to the length of the mining face. The width of the rock beam is the unit length and the thickness of the rock beam can be calculated by the following formula [34]:

$$h_2 = h - h_1, \quad (1)$$

where  $h_2$  is the thickness of the rock beam,  $h$  is the thickness of floor aquifuge, and  $h_1$  is the depth of floor failure zone due to mining activities, which can be determined by the following empirical formula:

$$h_1 = \frac{0.015H \cos \varphi}{2 \cos(\pi/4 + \varphi/2)} e^{(\pi/4 + \varphi/2) \tan \varphi}, \quad (2)$$

where  $H$  is the buried depth of the coal seam and  $\varphi$  is the internal friction angle.

Based on the definition of the elastic strain energy and the beam bending theory, the elastic strain energy  $U$  can be calculated by the following formula [35]:

$$U = \frac{EI}{2} \int_0^L k^2 ds, \quad (3)$$

where  $s$  is the arc length between the original point of the beam and the arbitrary point,  $k$  is the curvature of the rock beam. Due to  $\omega' \ll 1$ , therefore the curvature  $k$  can be approximately written as follows:

$$k = \frac{\omega''}{(1 + \omega'^2)^{3/2}} \approx \omega'' (1 + \omega'^2)^{1/2}, \quad (4)$$

where  $\omega$  is the deflection of the arbitrary point, which can be defined as follows:

$$\omega \approx \delta \sin \frac{\pi}{L} s, \quad (5)$$

where  $L$  is the length of the beam and  $\delta$  is the deflection of the beam midpoint.

Substituting equations (4) and (5) into equation (3), the elastic strain energy  $U$  can be written as follows:

$$U \approx \frac{EI}{2} \int_0^L \omega''^2 (1 + \omega'^2) ds = \frac{EI\pi^6 \delta^4}{16L^5} + \frac{EI\pi^4 \delta^2}{4L^3}, \quad (6)$$

where  $I = h_2^3/12$ .

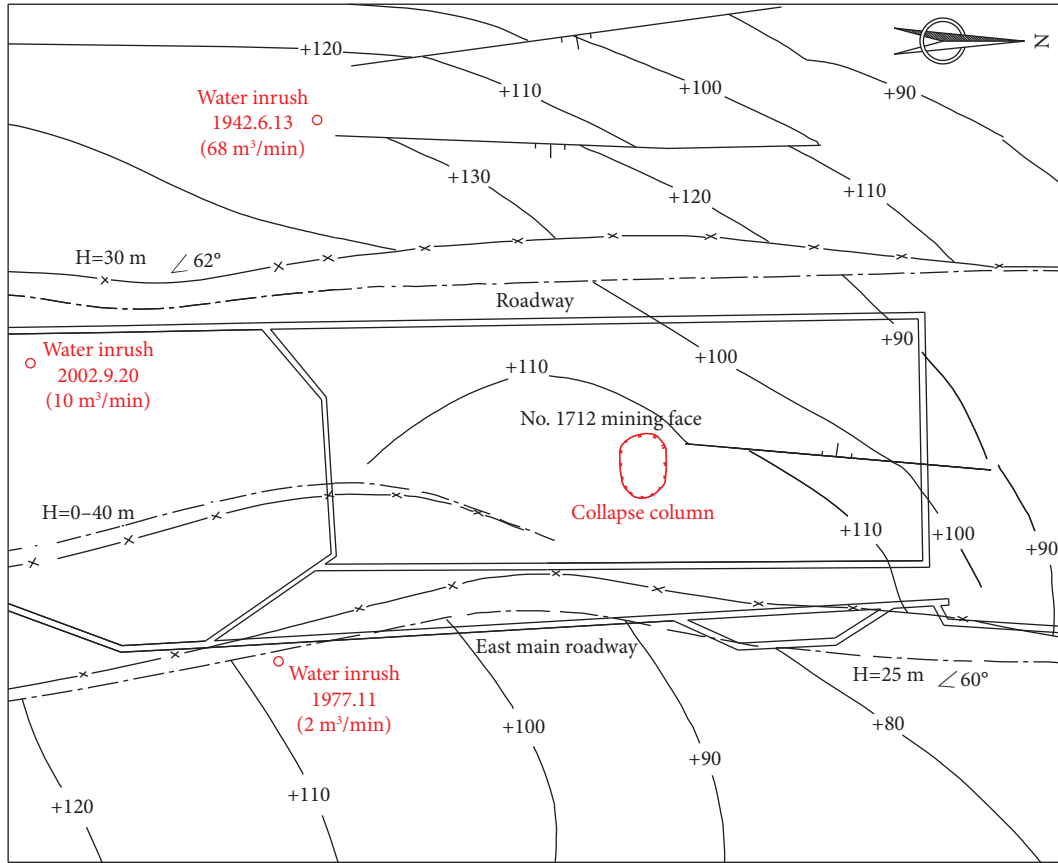


FIGURE 1: Geological structures in the study area of the Ruifeng coalmine.

The work done  $W_1$  by the horizontal forces can be expressed as follows:

$$W_1 = \sigma_3 h_2 \Delta L = \sigma_3 h_2 \left( L - \int_0^L \sqrt{1 - \omega'^2} ds \right), \quad (7)$$

where  $\Delta L$  is the horizontal shortened length of the beam because of the action of horizontal force.

Utilizing Taylor series expansion and ignoring the higher order term, we can get the following equation:

$$\sqrt{1 - \omega'^2} \approx 1 - \frac{\omega'^2}{2}. \quad (8)$$

Substituting equation (8) into equation (7),  $W_1$  can be written as follows:

$$W_1 \approx \frac{\sigma_3 h_2}{2} \int_0^L \omega'^2 ds = \frac{\sigma_3 h_2 \pi^2 \delta^2}{4L}. \quad (9)$$

Likewise, the work done  $W_2$  by vertical forces can be represented as follows:

$$W_2 = \int_0^L (p - q)\omega ds = \frac{2(p - q)L}{\pi} \delta, \quad (10)$$

where  $q = \gamma h_1$ .

The behaviour of a system is usually continuous, but sometimes exhibits discontinuities, which needs to be studied by bifurcation or catastrophe theory. Based on

Thom's classification theorem, there are seven elementary catastrophes, where the number of state variables is one or two and the number of control parameters (equal to the codimension) is four. One of the simple catastrophes is cusp catastrophe which involves two control parameters and one state variable. The maxima, minima, and inflection points of the potential function are known as stationary points. These points may be a singularity at which the value of the potential function can jump [36]. Therefore, the potential function should be established first. According to the catastrophe theory, the total potential energy  $V$  of the beam can be written as follows:

$$V = U - W_1 - W_2. \quad (11)$$

Substituting equations (6), (9), and (10) into equation (11), the total potential energy  $V$  can be approximated as follows:

$$V \approx \frac{EI\pi^6}{16L^5} \delta^4 + \frac{\pi^2}{4L} \left( \frac{EI\pi^2}{L^2} - \sigma_3 h_2 \right) \delta^2 - \frac{2(p - q)L}{\pi} \delta. \quad (12)$$

Equation (12) is the steady-state model of the rock beam and can be further transformed as the following standard form [35]:

$$V = x^4 + ax^2 + bx, \quad (13)$$

where

TABLE 1: Incomplete statistics of serious water inrush hazards in Handan-Xingtai mining area.

Number	Coal mine	Date	Maximum water inrush rate (m <sup>3</sup> /h)	Water inrush types
1	Wutongzhuang	1995-12-3	34000	Fault
2	Wutongzhuang	2001-3-10	156	Collapse column
3	Wutongzhuang	2002-6-7	480	Fault
4	Wutongzhuang	2002-3-21	120	Fault
5	Wutongzhuang	2000-5-14	130	Collapse column
6	Wutongzhuang	2006-1-26	3900	Fault
7	Wutongzhuang	2014-7-25	11250	Collapse column
8	Huangsha	2010-11-19	6000	Fault
9	Huangsha	2011-12-11	24000	Fault and collapse column
10	Huangsha	1996-12-19	1320	Mining activities
11	Huangsha	2010-11-19	6000	Fault
12	Jiulong	2009-1-8	7200	Collapse column
13	Jiulong	2007-9-29	5400	Collapse column
14	Jiulong	2007-10-21	720	Collapse column
15	Jiulong	2009-1-1	900	Collapse column
16	Jiulong	2009-1-11	7200	Collapse column
17	Xin'an	2010-11-19	6000	Fault
18	Xin'an	2011-12-11	24000	Collapse column
19	Xin'an	2011-12-11	2600	Fault and collapse column
20	Ruifeng	2002-9-20	600	Fault
21	Ruifeng	1977-11	120	Collapse column
22	Ruifeng	1932-8	480	Fault
23	Ruifeng	1942-6-13	4080	Fault
24	Dongpang	2003-4-12	70000	Collapse column
25	Dongpang	2010-11-15	2500	Mining activities
26	Niuerzhuang	2004-9-26	5160	Fault
27	Sunzhuang	1996-11-24	9000	Fault
28	Xingdong	2011-4-13	330	Mining activities
29	Shenjiazhuang	2012-5-26	740	Fault
30	Lincheng	2006-12-16	3600	Fault

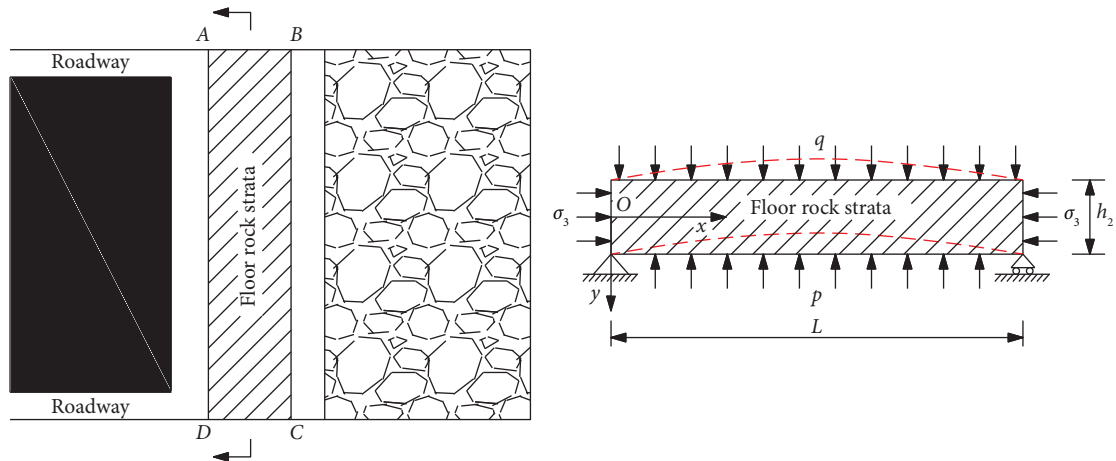


FIGURE 2: The simplified mechanical model of floor aquifer.

$$\begin{aligned}
 x &= \frac{\pi}{2L} \sqrt[4]{\frac{EI\pi^2}{L}} \delta, \\
 a &= L \sqrt{\frac{L}{EI\pi^2} \left( \frac{EI\pi^2}{L^2} - \sigma_3 h_2 \right)}, \\
 b &= -\frac{4(p-q)L^2}{\pi^2} \sqrt[4]{\frac{L}{EI\pi^2}}.
 \end{aligned} \quad (14)$$

The discriminant of floor water inrush is as follows [35]:

$$\Delta = 8a^3 + 27b^2 \begin{cases} > 0 & \text{no water inrush,} \\ = 0 & \text{critical state,} \\ < 0 & \text{water inrush.} \end{cases} \quad (15)$$

The system potential energy of rock beam is minimum when  $\Delta > 0$ . Therefore, the rock beam is stable and the water inrush cannot occur. However, it is on the contrary when  $\Delta < 0$ , namely, the rock beam is unstable and the water inrush occurs. When  $\Delta = 0$ , it is in critical state and the floor water inrush may occur under minimal engineering disturbance. In the Ruifeng coalmine, the hydraulic pressure of the confined aquifer is  $p \approx 1.33 \sim 1.73$  MPa and the thickness of the aquifuge is  $h \approx 49.0$  m. The buried depth of the No.5 coal seam is about  $-460$  m and the internal friction angle of the floor aquifuge is about  $30^\circ$ . Taking the above parameters to equation (2), the depth of floor failure zone due to mining activities is about  $h_1 \approx 12$  m. Besides, relevant physical and mechanical parameters are as follows:  $L \approx 80$  m,  $E \approx 10$  GPa,  $h_2 \approx 37$  m,  $q \approx 0.5$  MPa, and  $\sigma_3 \approx 11.5$  MPa, and taking the above parameters to equation (15), we can get  $\Delta > 0$ . In other words, the floor aquifuge is stable and mining above confined aquifer is safe. But considering the complex geological structures such as faults and collapse columns in the study area, floor water inrush still may occur during mining. Therefore, ESG microseismic monitoring system was applied to monitor the formation of water inrush pathway, which can predict floor water inrush.

#### 4. Numerical Analysis on Floor Water Inrush in the Ruifeng Coalmine

Floor water inrushes can be classified into two types: geological structures-controlled water inrush and mining-induced water inrush. The former is mainly caused by faults and karst collapse columns in the floor strata [37–39], the latter is directly related to the mining activities [3, 5, 22]. Mining activities would damage the floor aquifuge causing a decrease of aquifuge thickness. When the thickness of aquifuge decreases to the limit value, a water inrush accident must happen. Furthermore, mining makes the shear stress on the fault plane increase, which may cause the activation of faults and provide a pathway for confined water inflow. In the following, the software FLAC<sup>3D</sup> [40] was applied to simulate the plastic zone evolution of floor aquifuge containing a collapse column and the evolution of shear stress

on fault plane when the mining face advances to the geological structures.

**4.1. Collapse Column.** In this section, the software FLAC<sup>3D</sup> was applied to simulate the plastic zone evolution of floor aquifuge with the mining face advances to the collapse column. The numerical model is built based on the geological data of the Ruifeng coalmine. The numerical model is 250 m long, 160 m wide, and 180 m high. The horizontal section of collapse column is ellipse and its geometric parameters are shown in Figure 3. The physical and mechanical parameters of coal and rock strata are obtained based on experimental results, as shown in Table 2.

The depth of plastic zone of floor strata caused by mining is proportional to the mining thickness of the coal seam. Stress field and plastic zone around the collapse column are also influenced by mining activities. In the numerical simulation, the mining face begins with 80 m from the collapse column. The mining face advanced 30, 60, 75, 80, 85, 100, 130, and 160 m, respectively, with the distance of the mining face at 80 m, 50 m, 20 m, and 5 m before the center of the collapse column and  $-5$  m,  $-20$  m,  $-50$  m, and  $-80$  m after the center of the collapse column. Figure 4 shows the plastic zone evolution when the mining thickness is 2 m, 4 m, 6 m, and 8 m, respectively.

In general, the rock masses would undergo plastic yield when the tension stress or shear stress reach the limit value. The shear stress of floor aquifuge would increase at mining face after coal excavation. Furthermore, the peak value of shear stress increases as the mining thickness increases. The shear stress concentration would increase the range of floor plastic zone as shown in Figure 5. Before the mining face reaches the collapse column (mining advance less than 75 m), the plastic zone around the collapse column does not change. However, when the mining face reaches the collapse column, the plastic zone above the collapse column spread upward because of shear stress concentration. The depth of floor plastic zone is about 2.0 m, 4.0 m, 8.0 m, and 12.0 m when the mining thickness is 2.0 m, 4.0 m, 6.0 m, and 8.0 m, respectively. Furthermore, when the mining thickness is less than 6.0 m, the floor shallow plastic zone does not connect to the plastic zone around the collapse column. However, when the mining thickness is 8.0 m, the floor shallow plastic zone connects to the deep plastic zone, which indicates that the floor water inrush may occur. Therefore, the mining thickness has important influence on floor water inrush. In order to avoid floor water inrush accident and realize safe mining, the mining thickness should be less than 6.0 m.

**4.2. Fault.** The direct stress along the normal fault is tensile stress, which makes the cracks of tension-crushed zone open and connected. The floor water stored in the aquifer is more likely to flow through the aquifuge along the fault. Therefore, floor water inrush may occur when the mining face advances to the fault. Besides, the strength of the rock is very low near the fault plane, where the rocks fail more easily due to abutment pressure caused by mining activities. And this may result in a larger failure zone and increase the water inrush

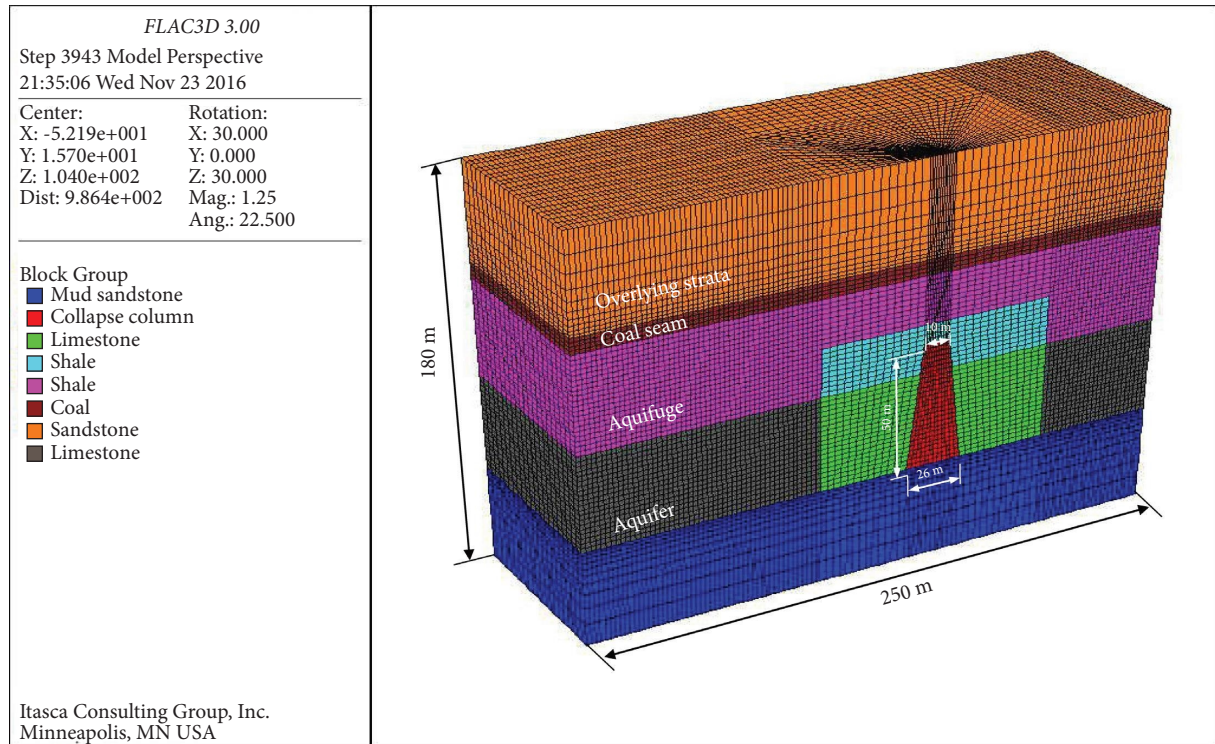


FIGURE 3: The numerical model of floor water inrush caused by collapse column.

TABLE 2: Physical and mechanical parameters of coal and rock.

Strata	Density ( $10^3 \text{ kg/m}^3$ )	Elastic modulus (GPa)	Poisson's ratio	Internal friction angle ( $^\circ$ )	Cohesion (MPa)	Tensile strength (MPa)
Sandy mudstone	2.60	25.92	0.26	30	9.13	1.45
Limestone	2.53	29.45	0.15	31	16.25	3.79
Shale	2.61	34.30	0.18	34	20.00	3.00
Coal	2.49	34.59	0.20	33	15.00	3.70
Sandstone	2.50	36.70	0.16	32	14.40	2.69

quantity. The numerical model is 250 m long, 120 m wide, and 160 m high. The monitoring points on the fault plane are located at  $-5 \text{ m}$ ,  $-10 \text{ m}$ ,  $-15 \text{ m}$ ,  $-20 \text{ m}$ ,  $-25 \text{ m}$ ,  $-30 \text{ m}$ ,  $-35 \text{ m}$ ,  $-40 \text{ m}$ , and  $-45 \text{ m}$ , as shown in Figure 4. The physical and mechanical parameters of coal and rock strata are shown in Table 3.

Shear stress on the fault plane usually plays an important role in the fault activation. Figure 6 shows the variation laws of shear stress on fault plane when the mining face advances to the fault. It can be seen from Figure 7 that the shear stress on fault plane increases at first and then decreases before the mining face reaches the fault. After the mining face reaches the fault, the shear stress decreases at first and finally reaches stable. With the mining face advancing to the fault, the deep shear stress of fault plane increases at first and then the shallow shear stress of fault plane increases. Furthermore, the shear stress on fault plane in shallow floor is more influenced by mining. The maximum shear stress is 9.7 MPa and the maximum shear stress concentration factor is about 1.9. The shear stress peaks when the mining face is about 20 m away from the fault, the fault is more likely to slide causing floor water inrush; but after the mining face reaches

the fault, mining has small influence on the shear stress on the fault plane.

## 5. Judgment of Floor Water Inrush Based on Microseismic Monitoring Results

*5.1. Microseismic Monitoring Floor Water Inrush and the Layout of ESG Sensors.* The geological conditions are very complex in the study area because there are many faults and collapse columns. Floor water inrush is very difficult to accurately position and predict by the traditional methods. However, coal mining causes breakage of the floor aquifuge, which is accompanied by acoustic emission [41, 42]. Microseismic monitoring system could capture the AE information and position the fractured zone of floor strata, which is a necessary condition for floor water inrush. The analysis procedure of floor water inrush based on microseismic monitoring is shown in Figure 7. The floor water inrush pathway can be achieved by the spatial distribution of microseismic events. All ESG sensors are mainly installed in the east main roadway and No. 3050 return air lane, as shown in Figure 8. The positional parameters of ESG sensors



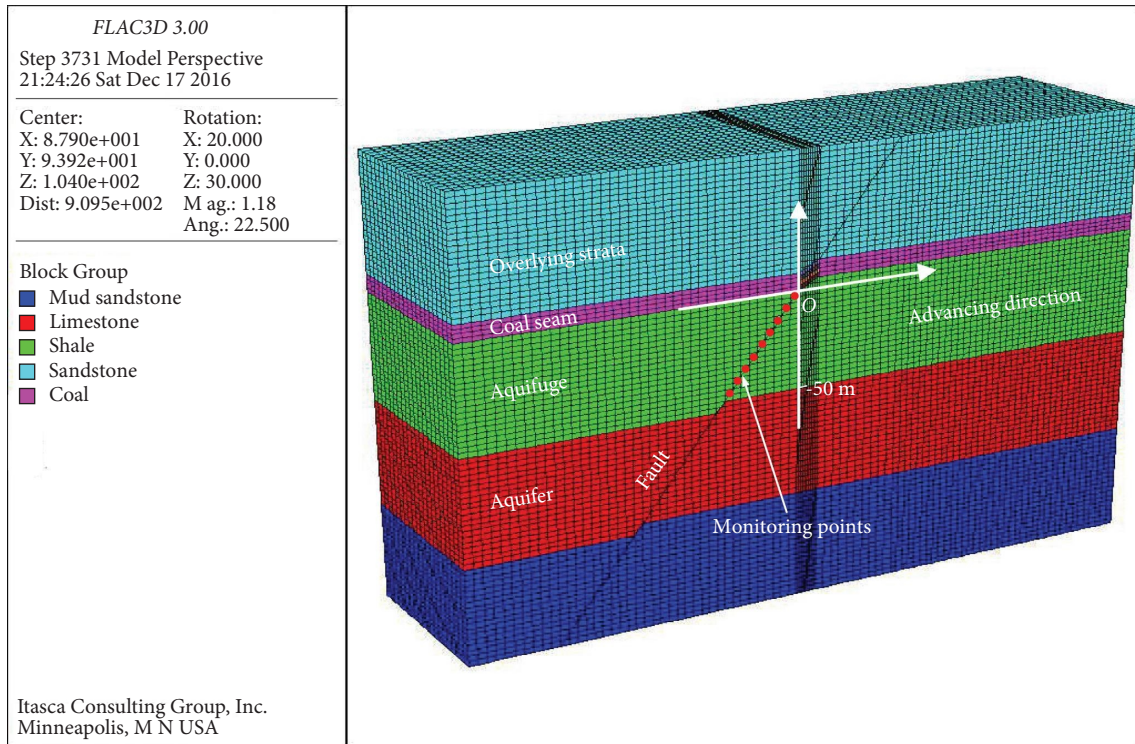


FIGURE 4: The numerical model of floor water inrush caused by the fault.

are shown in Table 3. The ESG sensors include 9 single pathway sensors (no. 1, no. 3, no. 4, no. 6, no. 7, no. 8, no. 9, no. 11, and no. 12) and 3 three-pathway sensors (no. 2, no. 5, and no. 10).

**5.2. Microseismic Monitoring Results.** The variation of energy release index and accumulated volume are shown in Figure 9. It was significantly found that a sharp increase of the energy release index occurred and the accumulated volume decreased suddenly on February 25, when the floor water inrush occurred. The floor aquifuge might experience the dynamic process that “energy accumulation → energy release → energy transfer,” matches well with the monitoring results of energy release index and accumulated volume. Therefore, floor water inrush is closely related to the variation of energy release index and accumulated volume. A sudden sharp change of energy release index or accumulated volume may be precursory characteristics of floor water inrush.

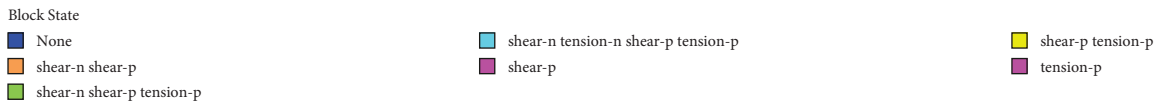
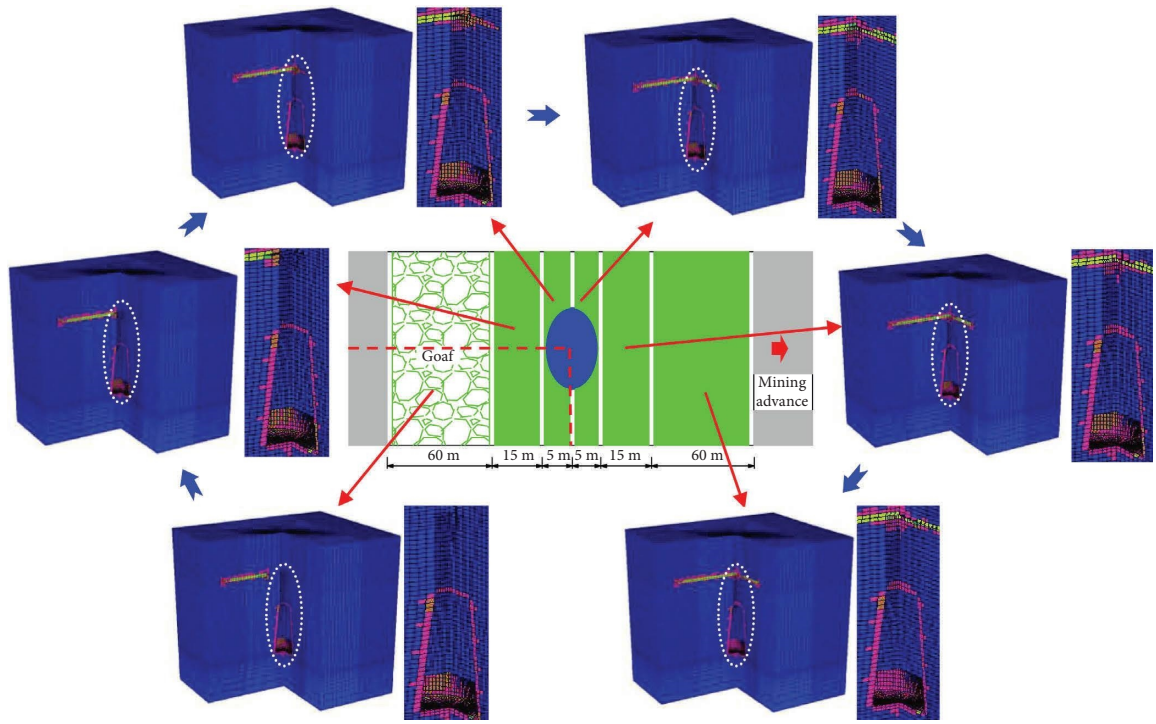
About 500 microseismic events occurred during the nearly four months’ monitoring and the spatial distribution of microseismic events is shown in Figure 10. The size of red dots represents the magnitude of microseismic events, namely, the bigger dot means that the rock fractures more seriously. As shown in Figure 11, the microseismic events initially occurred in the Ordovician limestone because of confined water. Besides, the floor strata unload after coal excavation, which causes the failure of the shallow floor aquifuge. Therefore, some microseismic events occurred in the shallow floor strata. Under the combined action of mining and confined water, the shallow floor fractured zone

finally connected to the aquifer and caused floor water inrush. There are two obvious water inrush pathways, located near two faults separately. One water inrush pathway is along the fault and the other water inrush pathway intersects the fault. Finally, the two water inrush pathways intersected at the water inrush position. The range of water inrush pathway gradually increases, which may cause the increase of water inrush rate.

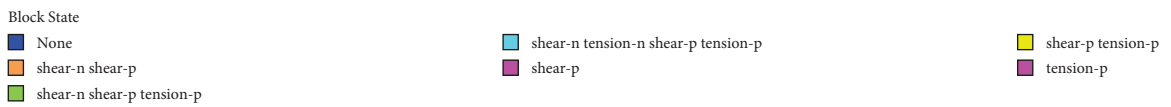
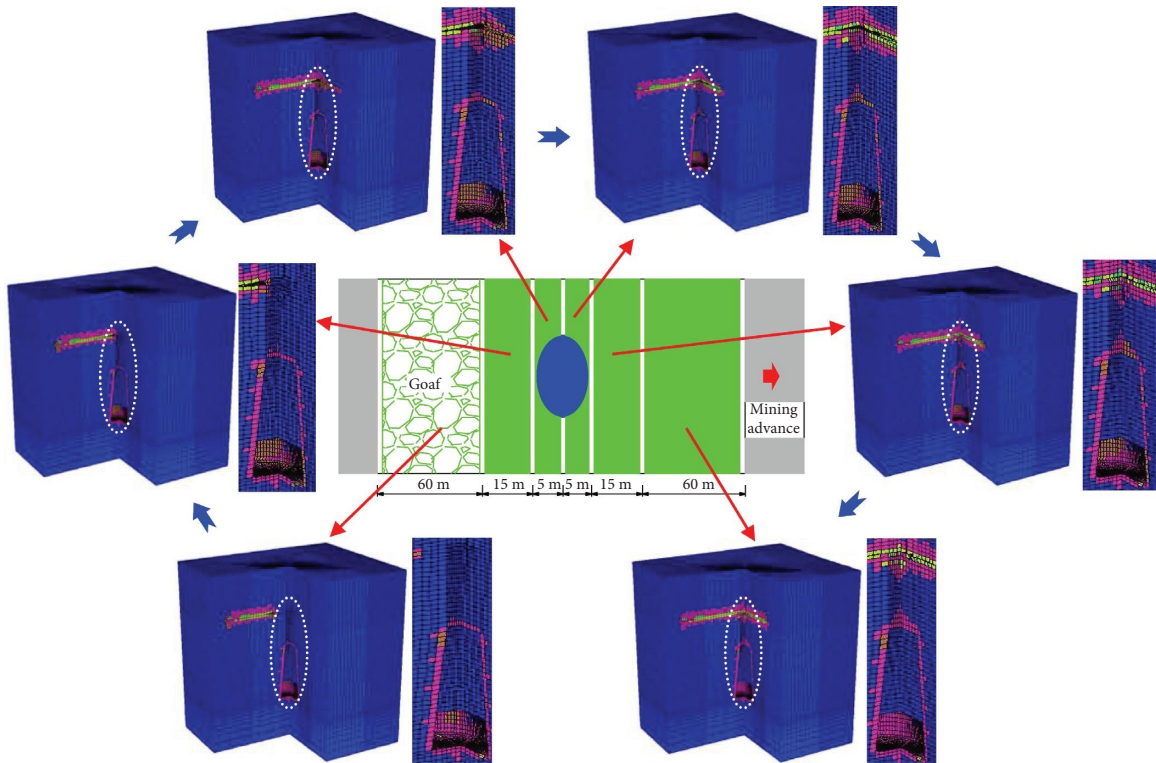
## 6. Targeted Grouting to Prevent Floor Water Inrush

In the Ruifeng coalmine, the traditional method to prevent floor water inrush is pregrouting, namely, some holes were drilled from the roadways into floor aquifuge and grouting cement slurry was conducted ahead of the mining face, as shown in Figure 11. Two grouting holes with different dip angle and length were drilled at the same place in the roadway. The average space between two adjacent grouting positions was about 40 meters. If the traditional pregrouting method was used, 52 grouting holes need to be drilled and the total length of grouting holes is about 3640 meters long. Furthermore, about 7600 tons of cement slurry would be injected.

But previous field practice show that the traditional pregrouting method was less effective to prevent floor water inrush and the cost was very high, because the grouting area was very large and the grouting holes were drilled blindly. Therefore, to effectively prevent floor water inrush and reduce the cost, targeted grouting method was proposed based on microseismic monitoring

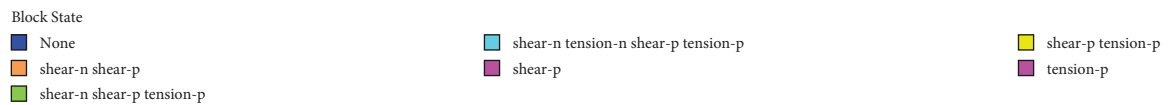
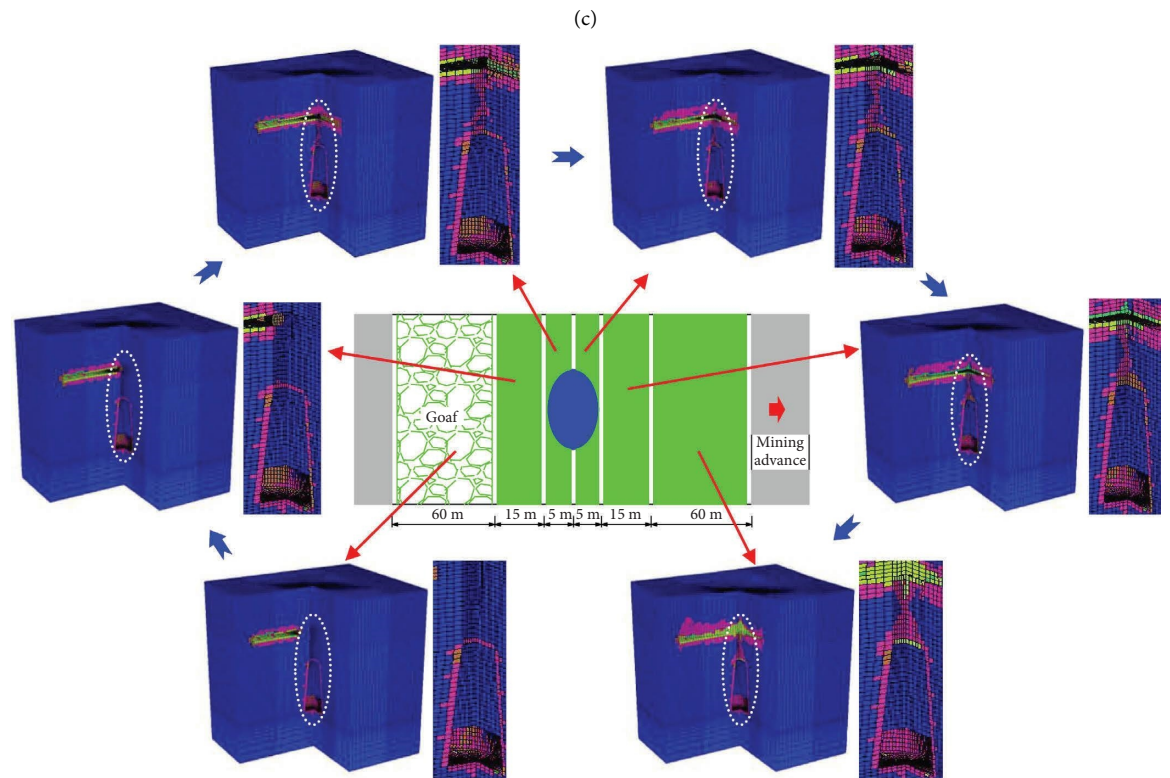
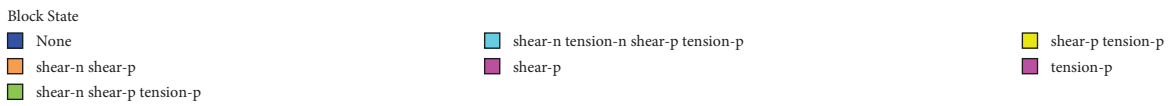
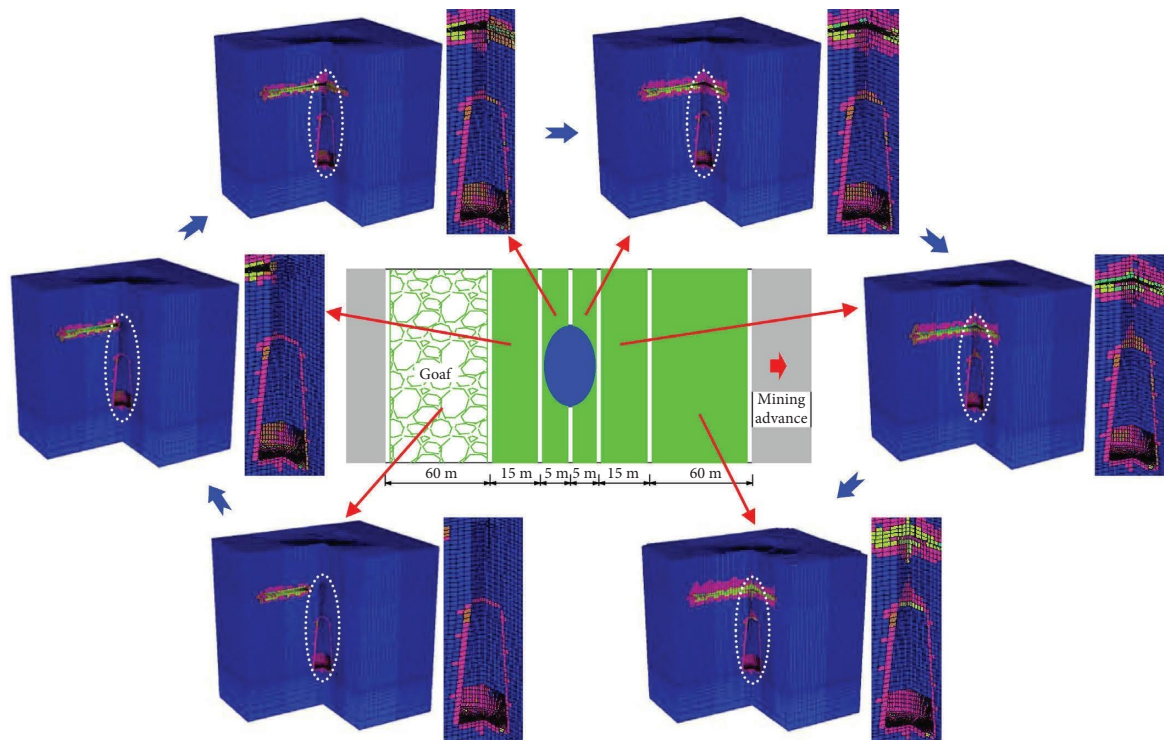


(a)



(b)

FIGURE 5: Continued.



(d)

FIGURE 5: The damage zone evolution of floor strata during mining. (a) The mining thickness is 2 m; (b) the mining thickness is 4 m; (c) the mining thickness is 6 m; and (d) the mining thickness is 8 m.

TABLE 3: The positional parameters of ESG sensors in the Ruifeng coalmine.

Number	The coordinates of ESG sensors			Dip angle (°)	Azimuthal angle (°)
	X	Y	Z		
1#	12395.492	20588.497	132.706	-30	-1
2#	12396.375	20505.893	132.185	-3	-2
3#	12429.610	20453.61	145.646	-30	88
4#	12509.072	20451.167	151.798	0	88
6#	12668.078	20462.936	144.475	0	179
5#	12588.771	20449.825	146.475	25	89
7#	12377.051	20634.143	132.239	-10	-93
8#	12464.329	20629.132	132.639	30	-93
10#	12633.068	20619.294	134.876	-25	-93
9#	12555.178	20624.009	133.174	30	-93
11#	12704.326	20614.977	134.877	0	-93
12#	12778.648	20623.827	134.882	-15	-94

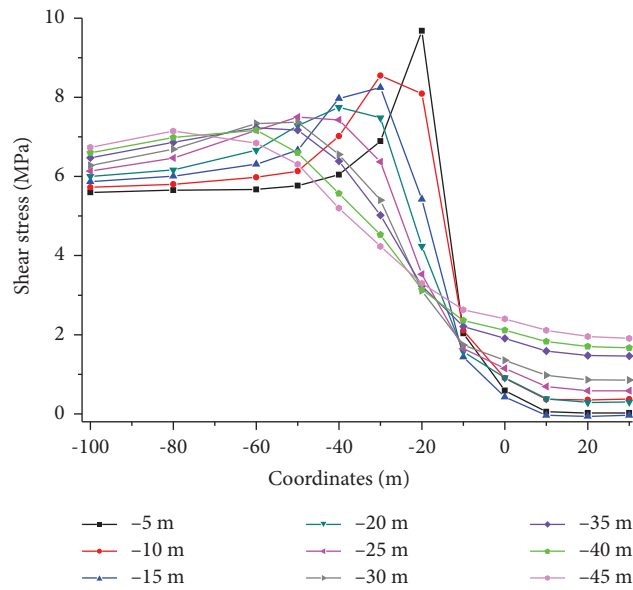


FIGURE 6: The variation laws of shear stress on the fault plane when the mining face advances to the fault.

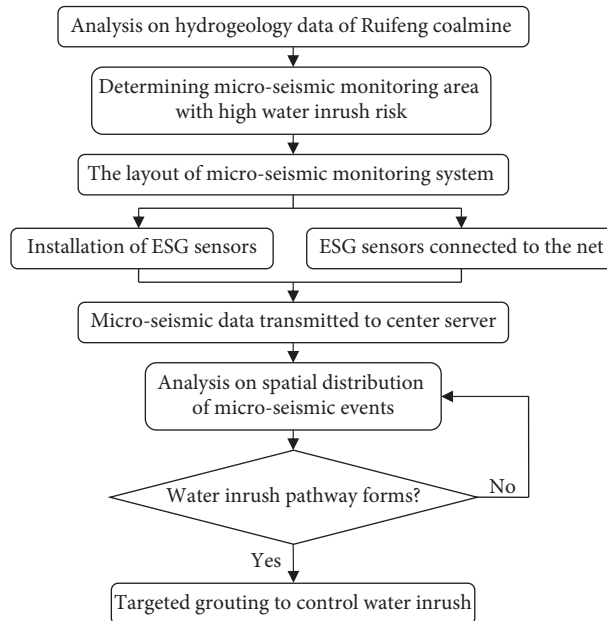


FIGURE 7: The procedure of floor water inrush control based on microseismic monitoring in the Ruifeng coalmine.

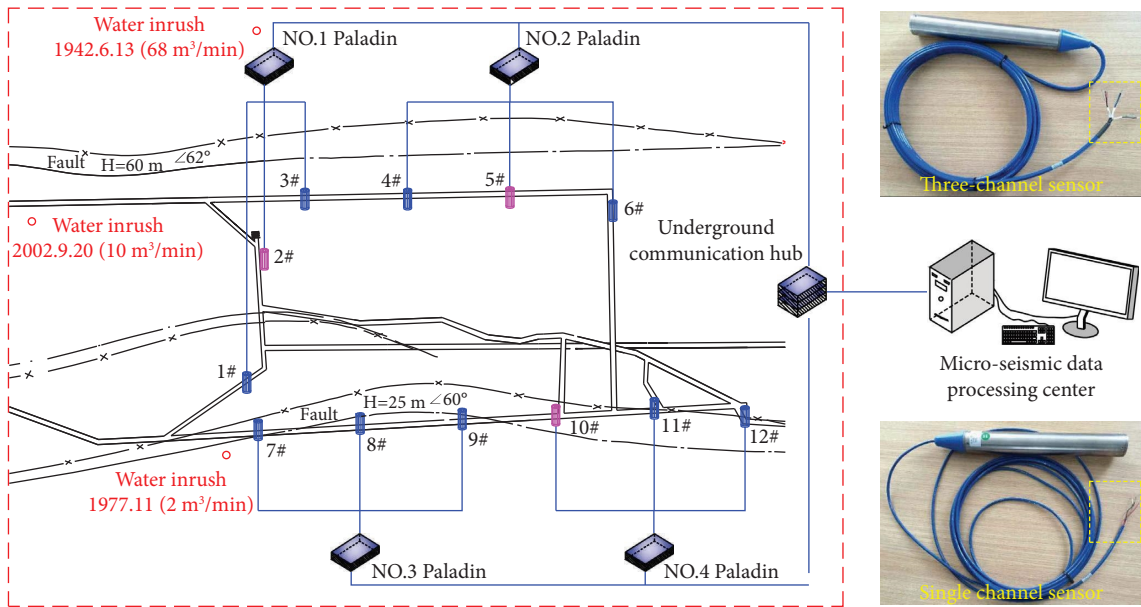


FIGURE 8: The layout of ESG sensors in the Ruifeng coalmine.

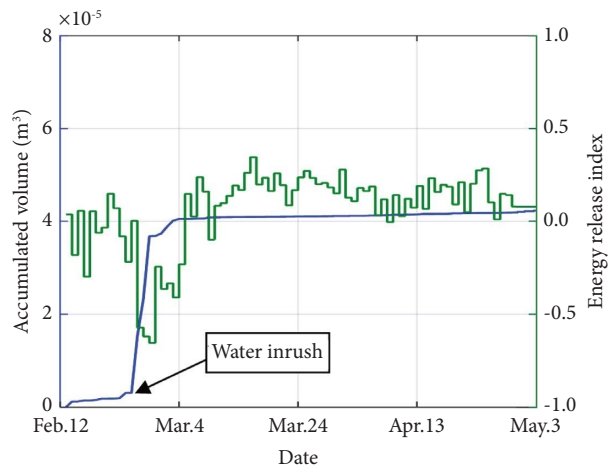
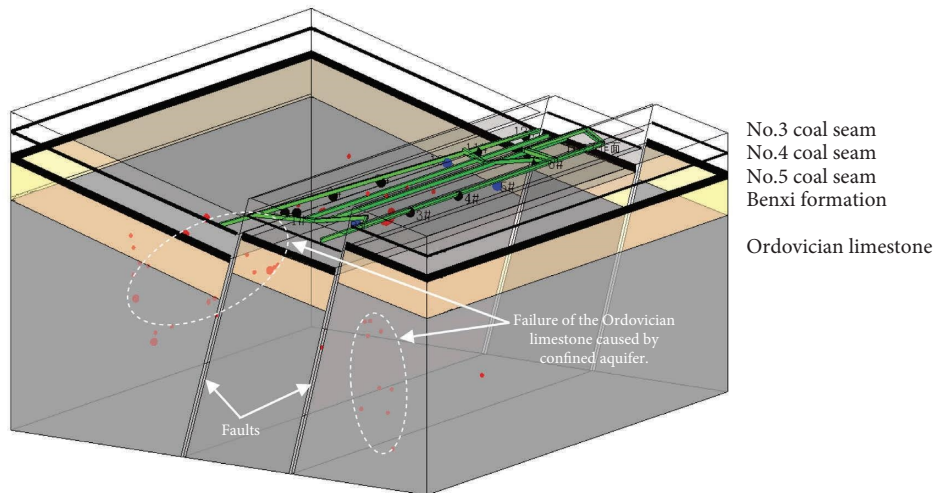


FIGURE 9: The variation laws of energy release index and accumulated volume.



(a)

FIGURE 10: Continued.

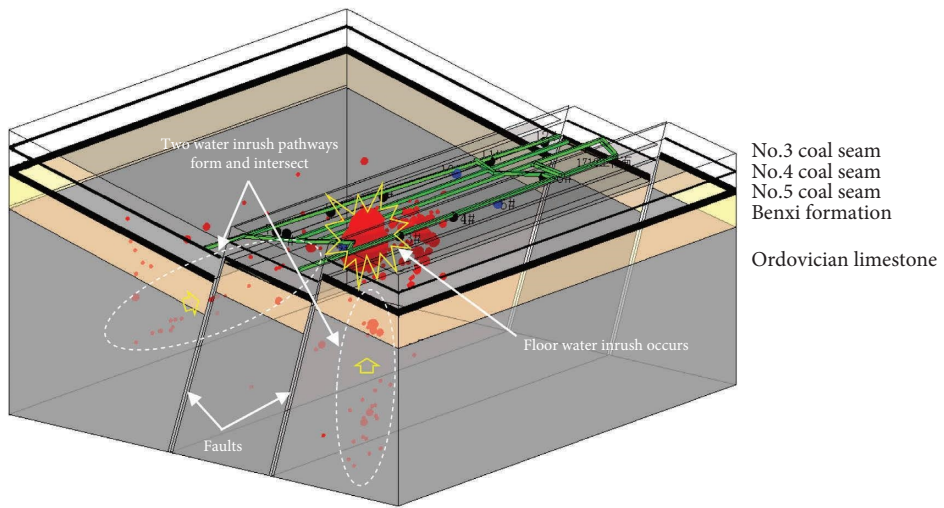
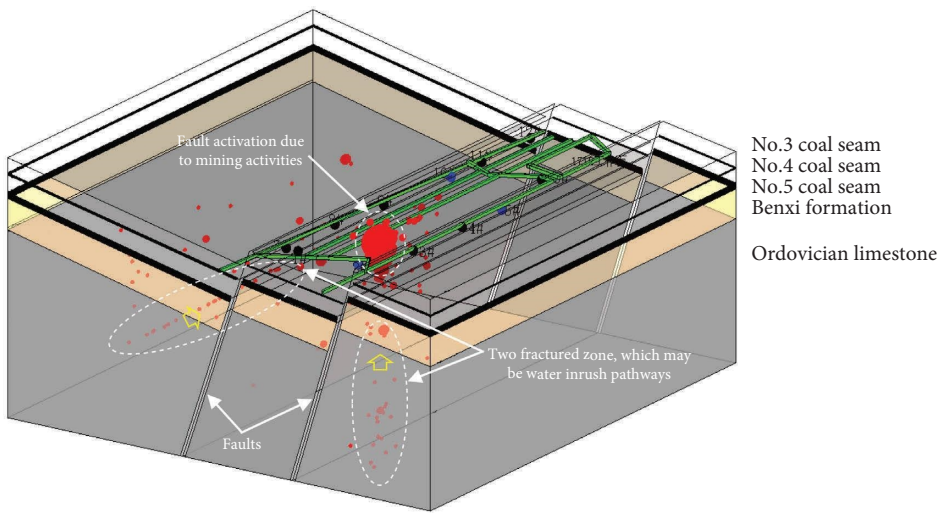
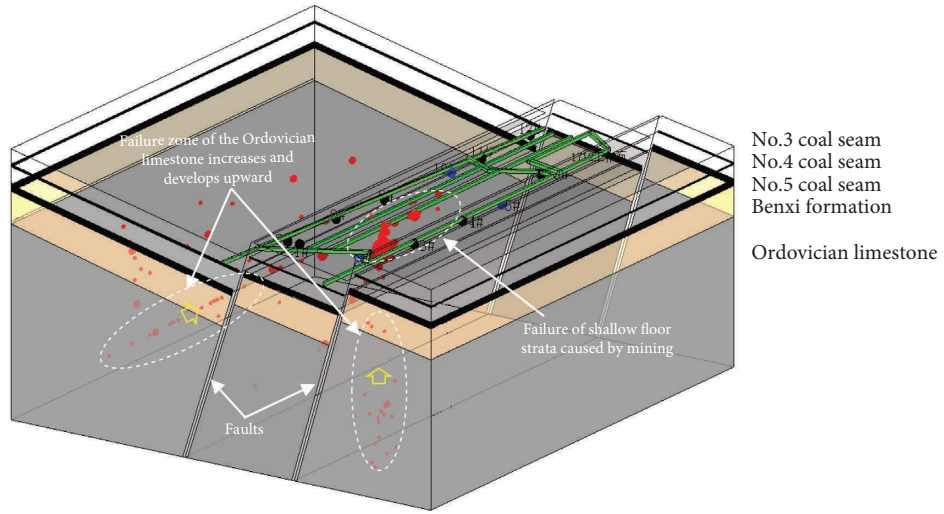


FIGURE 10: Continued.

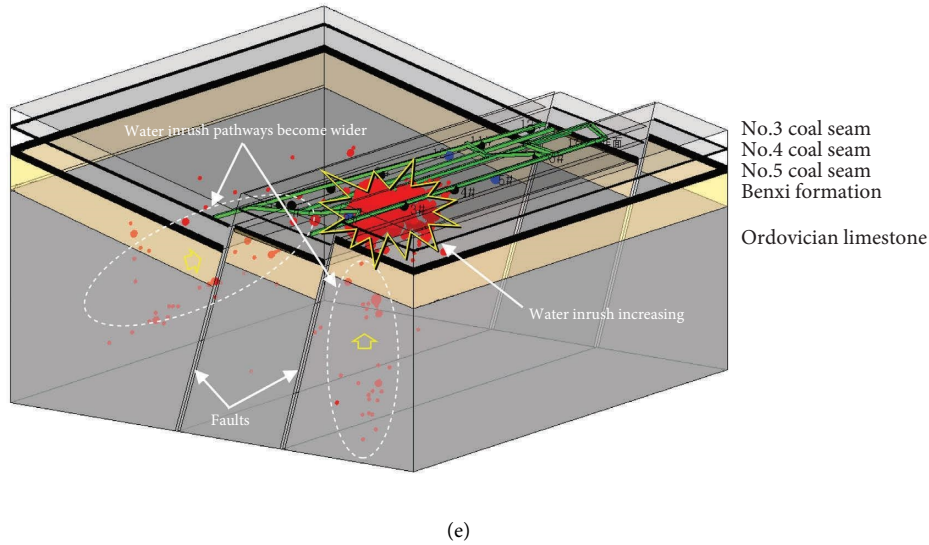


FIGURE 10: Spatial distribution of microseismic events in the Ruifeng coalmine.

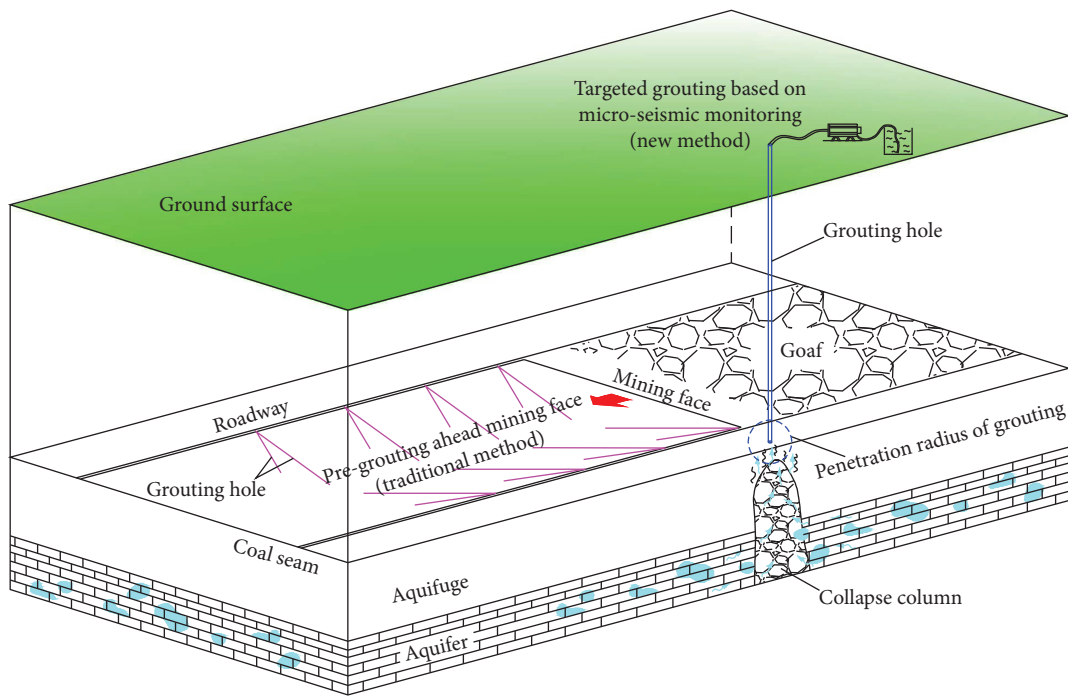


FIGURE 11: The pregrouting method and targeted grouting method to prevent floor water inrush in the Ruifeng coalmine.

results, as shown in Figure 11. Two water inrush pathways were positioned based on microseismic monitoring system. Correspondingly, two targeted grouting holes can be drilled from the ground. The total length of two grouting holes is about 950 meters, which is much less than that of the traditional pregrouting method. Furthermore, the water inrush was effectively prevented by injecting 900 tons of cement slurry, which was only a quarter of what the traditional pregrouting method consumed. Therefore, the targeted grouting method is more effective to prevent water inrush and significantly reduces the cost.

The variation laws of grouting pressure, water inflow rate, and microseismic events are shown in Figure 12. The water inrush occurred on February 25 and the targeted grouting was conducted 5 days later. The initial grouting pressure was 1.0 MPa and the final grouting pressure was 3.0 MPa. There are some fluctuations of grouting pressure because of the permeability change of floor strata. Additionally, the water inrush rate dramatically decreased from 80 m<sup>3</sup>/h to 20 m<sup>3</sup>/h after grouting for three days. In the end, the floor water inrush was completely prevented after grouting for 40 d. During the initial period of grouting, the

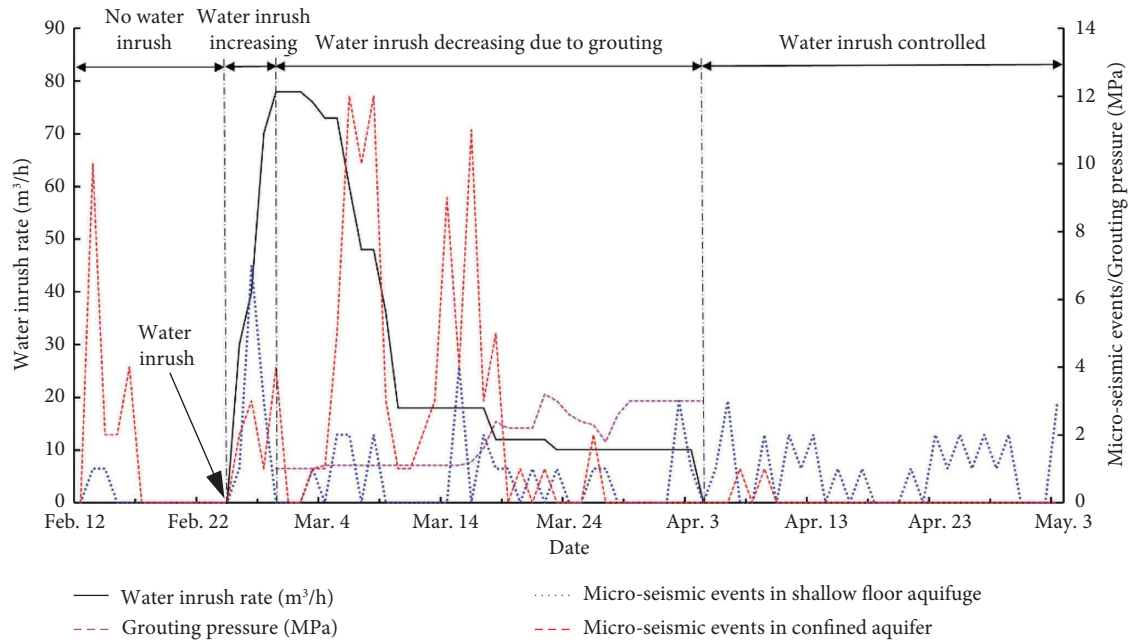


FIGURE 12: Variation laws of grouting pressure, water inrush rate, and microseismic events.

microseismic events still occurred in Ordovician limestone due to hydraulic fracturing. There are almost no microseismic events in Ordovician limestone after stopping grouting. But a few microseismic events in shallow floor strata occurred all the time due to mining activities.

## 7. Conclusions

- (1) Water inrush is the biggest threat for safe mining in the Ruifeng coalmine and the floor water inrush were mainly caused by mining activities and geological structures in the study mining area. Floor water inrush is more likely to occur during mining because the geological structures are complex in the study area. Based on cusp catastrophe theory, the mechanics criteria of floor water inrush is derived and the criteria is utilized to assess floor water inrush risk of the Ruifeng coalmine.
- (2) The failure process of the floor aquifuge during mining is achieved by numerical simulating. The mining thickness has important influence on floor water inrush. The depth of floor plastic zone increases with the increase of mining thickness. When the mining thickness is less than 6.0 m, the floor shallow plastic zone does not connect to the plastic zone around the collapse column. However, when the mining thickness is 8.0 m, the floor shallow plastic zone connects to the deep plastic zone, which indicates that the floor water inrush may occur. Therefore, in order to avoid floor water inrush, the mining thickness should be less than 6.0 m.
- (3) The shear stress on the fault plane increases at first and then decreases before the mining face reaches the fault. After the mining face reaches the fault, the shear stress decreases at first and finally reaches

stable. With the mining face advancing to the fault, the deep shear stress of the fault plane increases at first and then the shallow shear stress of the fault plane increases. Furthermore, the shear stress on the fault plane in shallow floor is more influenced by mining. The shear stress peaks when the mining face is about 20 m away from the fault, where the fault is more likely to slide causing floor water inrush.

- (4) ESG microseismic monitoring system was applied to monitor the formation process of water inrush pathway. The field monitoring results show that two water inrush pathways were accurately positioned. Then, two grouting holes were drilled from the ground surface and the water inrush was effectively prevented by injecting 900 tons of cement slurry, which significantly reduced the cost.

## Data Availability

The proposed numerical model and data used during the current study are available from the corresponding author.

## Conflicts of Interest

The authors declare that they have no conflicts of interest.

## Acknowledgments

This work was supported by the China Postdoctoral Science Foundation (no. 2020M680756).

## References

- [1] J. C. Zhang, "Investigations of water inrushes from aquifers under coal seams," *International Journal of Rock Mechanics and Mining Sciences*, vol. 42, no. 3, pp. 350–360, 2005.



- [2] Q. Wu, M. Wang, and X. Wu, "Investigations of groundwater bursting into coal mine seam floors from fault zones," *International Journal of Rock Mechanics and Mining Sciences*, vol. 41, no. 4, pp. 557–571, 2004.
- [3] J. A. Wang and H. Park, "Coal mining above a confined aquifer," *International Journal of Rock Mechanics and Mining Sciences*, vol. 40, no. 4, pp. 537–551, 2003.
- [4] Y. L. Lu and L. G. Wang, "Numerical simulation of mining-induced fracture evolution and water flow in coal seam floor above a confined aquifer," *Computers and Geotechnics*, vol. 67, pp. 157–171, 2015.
- [5] J. A. Wang and H. Park, "Fluid permeability of sedimentary rocks in a complete stress-strain process," *Engineering Geology*, vol. 63, no. 3–4, pp. 291–300, 2002.
- [6] W. Q. Liu, X. D. Fei, and J. N. Fang, "Rules for confidence intervals of permeability coefficients for water flow in overbroken rock mass," *International Journal of Mining Science and Technology*, vol. 22, no. 1, pp. 29–33, 2012.
- [7] Q. Wang, B. Jiang, S. Xu et al., "Roof-cutting and energy-absorbing method for dynamic disaster control in deep coal mine," *International Journal of Rock Mechanics and Mining Sciences*, vol. 158, Article ID 105186, 2022.
- [8] Q. Wang, S. Xu, Z. X. Xin, M. C. He, H. Y. Wei, and B. Jiang, "Mechanical properties and field application of constant resistance energy-absorbing anchor cable," *Tunnelling and Underground Space Technology*, vol. 125, Article ID 104526, 2022.
- [9] S. B. Tang, J. M. Li, S. Ding, and L. T. Zhang, "The influence of water-stress loading sequences on the creep behavior of granite," *Bulletin of Engineering Geology and the Environment*, vol. 81, no. 11, p. 482, 2022.
- [10] W. C. Zhu and C. H. Wei, "Numerical simulation on mining-induced water inrushes related to geologic structures using a damage-based hydromechanical model," *Environmental Earth Sciences*, vol. 62, no. 1, pp. 43–54, 2011.
- [11] Q. Wu and W. Zhou, "Prediction of groundwater inrush into coal mines from aquifers underlying the coal seams in China: vulnerability index method and its construction," *Environmental Geology*, vol. 56, no. 2, pp. 245–254, 2008.
- [12] G. Li and W. Zhou, "Impact of karst water on coal mining in North China," *Environmental Geology*, vol. 49, no. 3, pp. 449–457, 2006.
- [13] T. Glade and F. Nadim, "Early warning systems for natural hazards and risks," *Natural Hazards*, vol. 70, no. 3, pp. 1669–1671, 2014.
- [14] J. C. Zhang and B. H. Shen, "Coal mining under aquifers in China: a case study," *International Journal of Rock Mechanics and Mining Sciences*, vol. 41, no. 4, pp. 629–639, 2004.
- [15] W. Q. Peng, W. J. Wang, and Q. F. Li, "Reasonable width of waterproof coal pillar under the condition of different fault dip angles," *Journal of Mining and Safety Engineering*, vol. 26, no. 2, pp. 179–186, 2009.
- [16] Z. P. Meng, R. Wang, Y. Y. Wang, J. Liu, J. H. Zhang, and J. Yuan, "Geologic evaluation of water inrush risk for No.12 coal seam floor of Fangezhuang mine field in Kailuan," *Journal of Mining and Safety Engineering*, vol. 27, no. 3, pp. 310–315, 2010.
- [17] X. Liang, S. B. Tang, C. A. Tang, L. H. Hu, and F. Chen, "Influence of water on the mechanical properties and failure behaviors of sandstone under triaxial compression," *Rock Mechanics and Rock Engineering*, vol. 56, no. 2, pp. 1131–1162, 2022.
- [18] Y. J. Sun, J. P. Zuo, M. Karakus, and J. T. Wang, "Investigation of movement and damage of integral overburden during shallow coal seam mining," *International Journal of Rock Mechanics and Mining Sciences*, vol. 117, pp. 63–75, 2019.
- [19] R. Zhang, Z. Q. Jiang, H. Y. Zhou, C. W. Yang, and S. J. Xiao, "Groundwater outbursts from faults above a confined aquifer in the coal mining," *Natural Hazards*, vol. 71, no. 3, pp. 1861–1872, 2014.
- [20] J. P. Zuo, S. P. Peng, Y. J. Li, Z. H. Chen, and H. P. Xie, "Investigation of karst collapse based on 3-D seismic technique and DDA method at Xieqiao coal mine, China," *International Journal of Coal Geology*, vol. 78, no. 4, pp. 276–287, 2009.
- [21] Y. Wang, C. Zhu, M. C. He, X. Wang, and H. L. Le, "Macromeso dynamic fracture behaviors of Xinjiang marble exposed to freeze thaw and frequent impact disturbance loads: a lab-scale testing," *Geomechanics and Geophysics for Geo-Energy and Geo-Resources*, vol. 8, no. 5, p. 154, 2022.
- [22] T. H. Yang, J. S. Liu, W. C. Zhu, D. Elsworth, L. G. Tham, and C. A. Tang, "A coupled flow-stress-damage model for groundwater outbursts from an underlying aquifer into mining excavations," *International Journal of Rock Mechanics and Mining Sciences*, vol. 44, no. 1, pp. 87–97, 2007.
- [23] S. Levasseur, R. Charlier, B. Frieg, and F. Collin, "Hydro-mechanical modelling of the excavation damaged zone around an underground excavation at Mont Terri Rock Laboratory," *International Journal of Rock Mechanics and Mining Sciences*, vol. 47, no. 3, pp. 414–425, 2010.
- [24] Y. J. Sun, J. P. Zuo, M. Karakus, L. Liu, H. W. Zhou, and M. L. Yu, "A new theoretical method to predict strata movement and surface subsidence due to inclined coal seam mining," *Rock Mechanics and Rock Engineering*, vol. 54, no. 6, pp. 2723–2740, 2021.
- [25] W. C. Zhu and O. T. Bruhns, "Simulating excavation damaged zone around a circular opening under hydromechanical conditions," *International Journal of Rock Mechanics and Mining Sciences*, vol. 45, no. 5, pp. 815–830, 2008.
- [26] K. Katsuyama, *Applications of Acoustic Emission (AE) Techniques*, China Metallurgical Industry Press, Beijing, China, 1997.
- [27] N. W. Xu, C. A. Tang, L. C. Li et al., "Micro-seismic monitoring and stability analysis of the left bank slope in Jinping first stage hydropower station in southwestern China," *International Journal of Rock Mechanics and Mining Sciences*, vol. 48, no. 6, pp. 950–963, 2011.
- [28] V. L. Shkuratnik, L. Filimonov, and S. V. Kuchurin, "Regularities of acoustic emission in coal samples under triaxial compression," *Journal of Mining Science*, vol. 41, no. 1, pp. 44–52, 2005.
- [29] J. Li, S. C. Wu, Y. T. Gao, L. Li, and Y. Zhou, "An improved multidirectional velocity model for micro-seismic monitoring in rock engineering," *Journal of Central South University*, vol. 22, no. 6, pp. 2348–2358, 2015.
- [30] C. L. Wang, "Identification of early-warning key point for rock mass instability using acoustic emission/microseismic activity monitoring," *International Journal of Rock Mechanics and Mining Sciences*, vol. 71, pp. 171–175, 2014.
- [31] C. Zhu, Y. Z. Xu, Y. X. Wu et al., "A hybrid artificial bee colony algorithm and support vector machine for predicting blast-induced ground vibration," *Earthquake Engineering and Engineering Vibration*, vol. 21, no. 4, pp. 861–876, 2022.
- [32] S. Fuchs, J. Birkmann, and T. Glade, "Vulnerability assessment in natural hazard and risk analysis: current approaches and future challenges," *Natural Hazards*, vol. 64, no. 3, pp. 1969–1975, 2012.

- [33] B. Schwendtner, M. Papathoma-Köhle, and T. Glade, "Risk evolution: how can changes in the built environment influence the potential loss of natural hazards," *Natural Hazards and Earth System Sciences*, vol. 13, no. 9, pp. 2195–2207, 2013.
- [34] S. X. Yin, J. C. Zhang, and D. M. Liu, "A study of mine water inrushes by measurements of in situ stress and rock failures," *Natural Hazards*, vol. 79, no. 3, pp. 1961–1979, 2015.
- [35] D. X. Liang, Z. Q. Jiang, S. Y. Zhu, Q. Sun, and Z. W. Qian, "Experimental research on water inrush in tunnel construction," *Natural Hazards*, vol. 81, no. 1, pp. 467–480, 2015.
- [36] X. R. Wang, K. Guan, T. H. Yang, and X. G. Liu, "Instability mechanism of pillar burst in asymmetric mining based on cusp catastrophe model," *Rock Mechanics and Rock Engineering*, vol. 54, no. 3, pp. 1463–1479, 2021.
- [37] L. Lianchong, Y. Tianhong, L. Zhengzhao, Z. Wancheng, and T. Chunan, "Numerical investigation of groundwater outbursts near faults in underground coal mines," *International Journal of Coal Geology*, vol. 85, no. 3-4, pp. 276–288, 2011.
- [38] C. Neuzil and J. V. Tracy, "Flow through fractures," *Water Resources Research*, vol. 17, no. 1, pp. 191–199, 1981.
- [39] R. Zimmerman and G. Bodvarsson, "Effective transmissivity of two-dimensional fracture networks," *International Journal of Rock Mechanics and Mining Sciences & Geomechanics Abstracts*, vol. 33, p. 433, 1996.
- [40] Itasca, *Fast Lagrangian Analysis of Continua in 3 Dimensions Manual*, Itasca Consulting Group Inc, Minneapolis, MN, USA, 2015.
- [41] D. P. Jansen, S. R. Carlson, R. P. Young, and D. A. Hutchins, "Ultrasonic imaging and acoustic emission monitoring of thermally induced micro cracks in Lac du Bonnet Granite," *Journal of Geophysical Research: Solid Earth*, vol. 98, no. B12, pp. 22231–22243, 1993.
- [42] C. Li and E. Nordlund, "Experimental verification of the Kaiser effect in rocks," *Rock Mechanics and Rock Engineering*, vol. 26, no. 4, pp. 333–351, 1993.

## Research Article

# Progressive Failure of Surrounding Rock in Underground Engineering and Size Effect of Numerical Simulation

Danling Zhong <sup>1</sup>, Jianlin Chen,<sup>1</sup> Hui Zhou <sup>2</sup>, Xiangrong Chen,<sup>1</sup> and Yali Jiang<sup>1</sup>

<sup>1</sup>Power China Huadong Engineering Corporation, Hangzhou 310014, China

<sup>2</sup>State Key Laboratory of Geomechanics and Geotechnical Engineering, Institute of Rock and Soil Mechanics, Chinese Academy of Sciences, Wuhan 430071, China

Correspondence should be addressed to Danling Zhong; zhong\_dn@hdec.com

Received 31 May 2022; Revised 29 October 2022; Accepted 5 April 2023; Published 18 April 2023

Academic Editor: Guang-Liang Feng

Copyright © 2023 Danling Zhong et al. This is an open access article distributed under the Creative Commons Attribution License, which permits unrestricted use, distribution, and reproduction in any medium, provided the original work is properly cited.

The analysis and simulation of progressive failure of surrounding rock is very important for analyzing the stability of surrounding rock in underground engineering. Size effect is also a key problem worth further study in engineering. Taking the underground powerhouse on the right bank of Baihetan as an example, the acoustic test results are collected and the relaxation and failure characteristics of the surrounding rock are summarized. Then, the numerical simulation of progressive failure of surrounding rock of underground powerhouse is carried out by using the finite discrete element method CDEM (continuum-based discrete element method). The results are compared with the acoustic test results of the surrounding rock relaxation layer, and the stress and displacement of surrounding rock characteristic points are analyzed. At the same time, the size effect of grid and mechanical parameter in the process of numerical simulation are discussed. The calculated fracture depth of surrounding rock is in good agreement with the acoustic test results, which shows the reliability of progressive failure simulation of surrounding rock of the underground powerhouse. When CDEM is used to simulate the excavation of tunnels with different tunnel diameters, the minimum grid size should be about 1% of the tunnel diameter. The mechanical parameters of rock mass have significant size effect, which needs to be analyzed in detail. The research results prove the superiority of the CDEM method in simulating the progressive failure of hard surrounding rock and its unique size effect characteristics, which can provide technical reference for the application of the CDEM method in other similar engineering problems.

## 1. Introduction

Under high stress conditions, the excavation of hard rock tunnels will cause rapid adjustment of secondary stress field of the surrounding rock, which may lead to damage destabilization phenomena such as local spalling, collapse, or even rock burst of surrounding rock, seriously threatening the project progress and personnel safety [1–3]. Some scholars have studied the failure mechanism of the surrounding rock in Jinping and Baihetan underground powerhouses [4, 5]. It is of great theoretical value and academic significance to study the progressive failure of the surrounding rock in underground engineering and explore the grid size effect and rock mass parameter size effect in

numerical simulation analysis to ensure engineering safety and improve the theory of rock mass mechanics.

The numerical method to simulate the failure of the surrounding rock in underground engineering is mainly divided into three categories: continuous medium mechanics method, discontinuous medium mechanics method, and continuous discontinuous combination method. Among them, continuum mechanics methods include finite difference method (FDM), finite element method (FEM), and boundary element method (BEM). When simulating the mechanical behavior of the rock, these methods are difficult to reflect the strain softening phenomenon caused by local damage and failure of materials, and the characterization of macrocrack and fracture propagation is not intuitive.

Therefore, new models or methods are introduced such as Martin's high-order constitutive criterion [6], Cosserat's micropolar model [7], nonlocal model [8], and meshless method [9]. Later, based on the addition of shape function with discontinuous property to the traditional finite element equation, the generalized finite element method (GFEM) [10] and extended finite element method (XFEM) [11–13] appeared. For example, Belyschko et al. [12] used XFEM to simulate a tunnel in fractured rock mass, and represented the crack with the discontinuity of internal displacement of rock mass.

Discontinuous mechanics method can directly simulate rock mass fracture and its interaction, but it is difficult to be used in the structural numerical analysis of large-scale complex projects due to the limitation of calculation ability and algorithm stability and the difficulty of defining mesoparameters. Discontinuous medium methods can be divided into two categories: discrete element method (DEM) [14–16], discontinuous deformation analysis method (DDA) [17], and numerical manifold method (NMM) [18]. For example, Duan et al. [15] used the DEM method to study the damage of hard rock caused by excavation unloading.

Based on the advantages and adaptability of the continuous method and discontinuous method, numerical methods combining continuous and discontinuous medium method (such as FEM/BEM, FEM/DEM, and FDM/DEM) are gradually developed. Among them, the coupling method of the finite element and discrete element is the most mature, and many achievements have been made [19–22]. For example, the author uses the CDEM method to simulate the progressive failure of the surrounding rock of Canadian URL test tunnel [19] and Baihetan exploration tunnel [18]. Besides, the coupling of finite element methods and peridynamics [23–25] also developed to solve similar problems.

Surrounding rock failure is a process from continuous to discontinuous, accompanied by multiple crack propagation and large displacement. The finite discrete element method combining the continuous method and discontinuous method is more suitable to study the gradual transformation process of the surrounding rock from continuous to discontinuous after excavation. However, in the finite discrete element method, the crack can only occur along the triangular boundary, so the mesh size and mesh direction have a significant impact on the simulation results. For the grid direction, unstructured grid generation is generally adopted [26, 27]. As for the grid size, there is still no good method to select the grid size around the rock test samples with different sizes and tunnels with different diameters [28, 29].

In addition, in the numerical analysis of underground engineering, the value of rock parameters is very important. Size effect is one of the inherent properties of rock materials. The size effect of rock mechanical parameters includes strength and deformation. The main research methods are tests and numerical analysis. Among them, the research on the size effect of strength is mainly on rock compressive strength [30, 31], less on shear strength [32], and whether there is size effect on rock deformation parameters is controversial. So far, a lot of scholars have carried out a large number of tests on different kinds of rock mechanical

parameters, but no unified law of rock size effect has been summarized. And the size effect law of rock strength explained in the theory cannot correspond to the test results. Therefore, the research on the size effect of rock mechanical parameters is still an important research direction in geotechnical engineering.

The author has accumulated some achievements in using the finite discrete element method CDEM to simulate crack propagation, including the uniaxial and triaxial compression test of basalt, the URL test tunnel in Canada, and the Baihetan exploratory tunnel. In this paper, firstly, the same method is used to simulate the layer-by-layer excavation of the right bank powerhouse to show the reliability of the calculation results. Then, based on the previous simulation results of the indoor test and exploratory tunnel failure, the appropriate grid size and the variation law of mechanical parameters of basalt under different simulation scales are analyzed. The research results can provide technical reference for using CDEM to solve similar problems in other engineering.

## 2. Overview of Right Bank Powerhouse of Baihetan

*2.1. Background of the Project.* Baihetan Hydropower Station is one of the four step power stations in the lower reaches of Jinsha River, which will become the second largest giant hydropower station after the Three Gorges after completion.

The main caverns of the underground powerhouse on the right bank include the main and auxiliary powerhouse caverns, the main transformer caverns, the draft tube bulkhead gate chamber, and the tailrace surge chamber, which are arranged in parallel.

The powerhouse was excavated from top to bottom in ten layers. The total length of the underground powerhouse is 438 m, the height is 88.7 m, the top arch elevation is 624.6 m, the rock beam elevation ranges from 602.3 m to 604.4 m, and the widths below and above the rock beam are 31 m and 34 m, respectively.

*2.2. Geological Conditions.* The main and auxiliary powerhouses on the right bank are monoclinical rock strata, and the trend of rock strata intersects the powerhouse axis at a large angle of  $60^{\circ}\sim 70^{\circ}$ . The exposed lithology is mainly aphanitic basalt, column jointed basalt, plagioclase basalt, almond basalt, breccia lava, and thin tuff from  $P_2\beta_3^3$  layer to  $P_2\beta_5^1$  layer. Among them, the exposed lithology of the right bank underground powerhouse is mainly massive basalt with breccia lava, which is hard, slightly new, and free of unloading. The rock mass structure is mainly submassive, with partial massive structure. The surrounding rock is mainly classified as Class III<sub>1</sub>, accounting for about 70%.

The surrounding rock of the right bank underground powerhouse caverns is developed with large soft interlayer staggered zone, small faults, random fractures, dense columnar joints, and other unfavorable structures, among which the interlayer staggered zone has the largest scale and

the most prominent impact. The right bank underground powerhouse caverns are mainly affected by the interlayer staggered zones C3, C3-1, C4, and C5.

**2.3. In Situ Stress.** The initial stress of the right bank underground powerhouse is generally stable, except for the local area affected by large structures, such as interlayer belts, and is dominated by tectonic stress fields and denudation transformation. The horizontal stress is significantly greater than the vertical stress. The maximum principal stress direction of the right bank underground powerhouse area is N-S direction, horizontal. The intermediate principal stress is E-W direction, which inclines to the valley about  $0^{\circ}\sim 5^{\circ}$ , and partially inclines to the mountain due to the influence of the interlayer zone. The minimum principal stress is nearly vertical. According to the measurement, the stress size meets the following relationship:

$$\sigma_1 = 0.0304h + 10.2; \sigma_2 = 0.0268h + 7.5; \sigma_3 = 0.028h. \quad (1)$$

### 3. Relaxation Characteristics of the Right Bank Powerhouse

**3.1. Acoustic Test Results.** A total of 6~9 acoustic test sections are arranged in the underground powerhouse on the right bank, and the typical section is shown in Figure 1. Acoustic detection holes are distributed at the top arch of 624.6 m elevation, arch shoulder of 622.6 m and 617 m elevation, and side wall of 608 m, 601 m, 591 m, 572.4 m, and 560 m elevation.

Multiple acoustic tests are carried out in different excavation stages, and the results are summarized in Tables 1–3. According to the test results:

- (1) Crown and spandrel: The relaxation depth of the surrounding rock is generally about 0.9~2.5 m, with an average of about 1.54 m.
- (2) Side wall: The relaxation depth of surrounding rock at el. 608 m is about 2.6~4.0 m, and the average depth is 3.50 m. The relaxation depth of the surrounding rock at el. 601 m is about 3.0~5.6 m, with an average depth of 4.08 m. The relaxation depth of the upstream side wall at el. 591 m is about 1.0~2.6 m, and the average depth is 2.20 m. The relaxation depth of the downstream side wall at el. 583 m is about 2.0~2.6 m, with an average depth of 2.27 m. The relaxation depth of the upstream side wall at el. 572 m is about 1.4~2.6 m, with an average depth of 1.99 m.

**3.2. Failure Characteristics of Surrounding Rock.** The rock mass of the right bank powerhouse is mainly brittle rock. And the average in situ stress is 26 MPa, belonging to the high ground stress level. Many typical stress-based failure phenomena occurred during the excavation of the powerhouse, such as spalling, fracture, relaxation collapse, and concrete spray layer cracking, as shown in Figure 2.

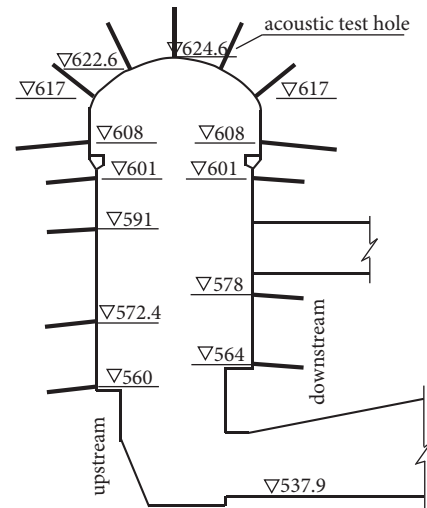


FIGURE 1: Typical section of acoustic test.

### 4. Numerical Simulation of the Right Bank Powerhouse

**4.1. Geometric Model.** Referring to the previous numerical simulation of URL test tunnel and Baihetan exploratory tunnel conducted by the author, the built-in software Gmsh is used for grid division, as shown in Figure 3.

The size of the whole model section is 600 m × 600 m. Area 1 is the powerhouse cavern to be excavated, and its grid size is 0.3 m. Area 2 is a square area close to the cavern with a range of 74 m × 133.9 m. Cracks first appear in this area during excavation, the grid size should be small enough to be 0.3 m. The range of area 3 is 300 m × 300 m, the grid size gradually changes from 0.3 m to 15 m. The range of area 4 is 600 m × 600 m, and the grid size changes from 15 m to 25 m. The total number of elements is 324244.

The right bank powerhouse is simulated according to the actual excavation process of eight layers, and the total excavation height is 73.9 m. The excavation heights from the first layer to the eighth layer are 13.6 m, 4.1 m, 11 m, 6.1 m, 11 m, 11 m, 4.9 m, and 12.2 m, respectively. The span of the top and bottom of the powerhouse is 34 m and 31 m, respectively.

**4.2. Geostress and Boundary Conditions.** The average burial depth of the powerhouse is about 500 m. The included angle between the first principal stress and the axis of the powerhouse is  $10^{\circ}$ , and the stress on the cross section of the powerhouse is mainly affected by the second principal stress. Ignoring the small dip angle of the second principal stress inclined to the valley, the in situ stress input by numerical simulation can be calculated, as shown in Table 4.

The boundary conditions adopted in the calculation are as follows: a normal displacement constraint is applied at the bottom. The normal stress is applied on the left and right sides, the shear stress is applied on the left and right, upper and lower sides, and both are applied under the condition of surface force. Then, the initial stress field of the model is obtained after calculation to the steady state.

TABLE 1: Statistical table of acoustic test results at el. 608 m.

Section number	Relaxation depth of the side wall (m)							Average
	No. 1	No. 2	No. 3	No. 4	No. 5	No. 6		
Upstream side wall at el. 608 m	2015.05.16	1.40	1.30	0.60	0.80	0.30	0.40	0.80
	2016.11.05	2.80	1.60	1.60	2.00	4.00	—	2.40
	2017.03.13	3.00	—	2.80	3.00	4.00	—	3.20
	2017.05.08	3.40	1.80	2.80	3.00	4.20	—	3.04
	2017.06.21	3.60	1.80	2.80	3.20	4.20	—	3.12
	2017.10.12	3.60	1.80	3.00	3.20	4.20	—	3.16
Downstream side wall at el. 608 m	2015.05.16	2.40	1.40	1.40	1.00	1.00	0.80	1.33
	2016.11.05	3.20	2.40	—	—	1.40	—	2.33
	2017.03.13	—	—	3.40	2.60	3.80	—	3.27
	2017.05.08	3.80	3.20	3.60	4.00	4.20	—	3.76
	2017.06.21	3.80	3.20	3.60	4.00	4.20	—	3.76
	2017.10.12	4.00	3.20	3.60	4.20	4.20	—	3.84
Average value					3.50			
Maximum value					4.20			

TABLE 2: Statistical table of acoustic test results at el. 601 m.

Section number	Relaxation depth of the side wall (m)									Average	
	No. 1	No. 2	No. 3	No. 4	No. 5	No. 6	No. 7	No. 8	No. 9		
Upstream side wall at el.601 m	2016.03.30	—	—	—	3.60	—	3.20	2.60	3.80	3.40	3.32
	2016.09.26	2.60	2.40	—	—	—	—	—	—	3.40	2.80
	2017.02.13	—	—	3.80	—	3.40	4.80	3.00	4.60	3.60	3.87
Downstream side wall at el. 601 m	2016.03.30	—	—	—	3.00	—	3.40	3.40	4.40	3.40	3.52
	2016.09.26	2.40	2.80	—	—	3.80	—	—	—	3.40	3.10
	2017.02.13	—	—	4.20	3.60	—	5.60	3.40	5.40	3.60	4.30
Average value					4.08						
Maximum value					5.60						

TABLE 3: Statistical table of acoustic test results at el. 591 m, el. 583 m, and el. 572 m.

Section number	Relaxation depth of the side wall (m)					Average	
	No. 1	No. 2	No. 3	No. 4	No. 5		
Upstream side wall at el. 591 m	2017.05.6	2.40	2.60	2.60	2.40	1.00	2.20
Downstream side wall at el. 583 m	2017.07.10	—	2.60	2.00	2.20	—	2.27
Upstream side wall at el. 572 m	2017.10.15	—	1.80	1.40	1.80	2.60	1.90
Downstream side wall at el. 578 m	2017.10.15	—	—	—	—	2.20	2.20
Average value					2.14		
Maximum value					2.60		

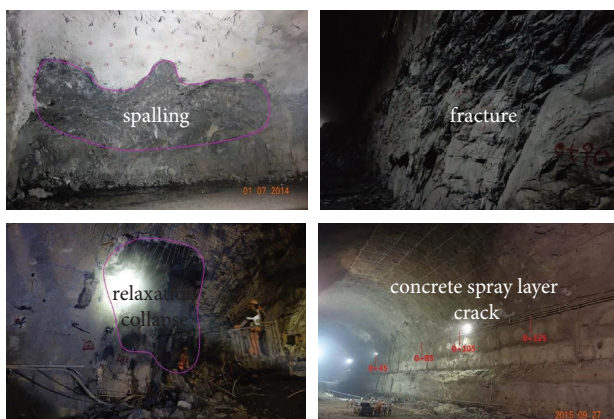


FIGURE 2: Stress-based failure features of the right bank powerhouse.

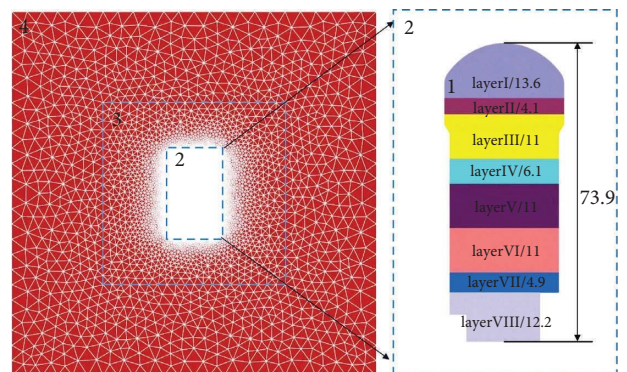


FIGURE 3: Model of numerical simulation.

TABLE 4: Geostress input for calculation of right bank powerhouse.

Stress	The first principal stress	The second principal stress	The third principal stress	Normal stress	Shear stress
Value (MPa)	25.4	20.9	14	21	0.77

**4.3. Calculation Steps and Mechanical Parameters.** As for the feedback analysis of the powerhouse tunnel group during the construction, a large number of numerical calculations have been carried out and rich results have been achieved. In their work, numerical analysis software FLAC3D or 3DEC is usually used for calculation, and the Hoek–Brown model and corresponding parameters are selected.

In this paper, the software CDEM is used for calculation. The constitutive model is based on the Mohr–Coulomb strength failure criterion. The acquisition methods of rock mass strength parameters and deformation parameters are as follows:

- (1) extract the rock mass density, uniaxial compressive strength UCS, geological strength index GSI, and the coefficient  $m_i$  from the previous calculation report;
- (2) input the abovementioned parameters and tunnel buried depth into the RocData program to obtain the basic parameters of rock mass.
- (3) input the basic parameters of rock mass into the numerical calculation model as initial data, and the failure characteristics of surrounding rock with given parameters are calculated and compared with the failure characteristics observed.
- (4) In the process of feedback analysis, GSI and UCS shall be properly adjusted according to the difference of local rock mass quality until the calculation results are fully close to the observed. The final mechanical parameters adopted in the calculation are shown in Table 5.

The specific calculation steps are as follows: The initial in situ stress field is firstly calculated with a total of 1,000,000 steps. Then, the excavation simulation of the powerhouse start shall be carried out. Each layer of excavation shall be calculated in 3,000 steps until it is stable, which shall be carried out in 8 times. The total number of calculation steps is 1,024,000.

## 5. Results Analysis

**5.1. Fracture Evolution of Surrounding Rock.** The evolution process of internal cracks in layers I~VIII of the powerhouse is obtained after the completion of excavation, as shown in Figure 4. At the same time, the damage of one-dimensional spring, i.e., contact element, is monitored during the calculation, and a total of three variables are statistically output, as shown in Figure 5. Among them, the total damage of spring is the proportion of elements that have been damaged. The total rupture of spring is the proportion of elements that have not only been damaged but also have the cohesion and tensile strength reduced to zero. The current damage of spring is the proportion of elements that are now in a damaged state.

TABLE 5: Mechanical parameters for simulation.

Parameters	Values
Density $\rho$ (kg/m <sup>3</sup> )	2750
Deformation modulus $E$ (GPa)	26
Poisson's ratio $\nu$	0.25
Cohesion $c$ (MPa)	3.2
Tensile strength $\sigma_t$ (MPa)	0.3
Initial internal friction angle $\varphi^\circ$	5.16
Multiplication of the increase of internal friction angle $n$	10
Dilatancy angle $\psi^\circ$	10
Tensile fracture energy (Pa.m)	50
Shear fracture energy (Pa.m)	500

As can be seen from Figure 4, after the excavation of layer I is completed, a circle of cracks appear in the surrounding rock of left and right bank spandrels and crown arches, and the cracks are evenly and symmetrically distributed. After the excavation of layer II, the crack propagation range increases, mainly along the exposed side wall of layer II, and the crack propagation depth increases slightly compared with that after the excavation of layer I. After the excavation of layer III, the number of cracks increases significantly. This is the design position of rock beam where the excavation surface is irregular. The cracks expand rapidly to the depth along the side walls on both sides, and the propagation depth is much greater than the crack depth of the top arch and left and right spandrels. After the excavation of layers IV~VIII is completed, the law of crack propagation is relatively consistent. The cracks expand and connect along the exposed side wall, and the crack propagation depth is large. Under the action of cracks, the side walls on both sides tend to deform towards the free face, which can be reflected from the inclination of the side wall after the excavation of layer VIII. This phenomenon may be related to the high height of the side wall. As the excavation boundary of the pit in layer VIII is irregular, the crack distribution density is large at the turning point of the right footing, and the edge of the footing tends to rise.

There is a good correspondence between Figures 4 and 5. After the excavation of the powerhouse, the three fracture curves continue to grow with the advance of calculation steps. Taking the failure condition when reaching stability as an example, it can be seen from the total damage curve of spring that the proportion of cracks in stable state does not increase much during the excavation of layers I~IV. From layer V to layer VIII, a large number of cracks are generated in the excavation process of each layer, and the proportion of cracks expands in an approximate S-shaped trend. At the end of each layer excavation, the crack propagation basically reaches a stable state. The total rupture curve of spring and the current damage curve of spring are the completely damaged elements and the elements now in the damaged

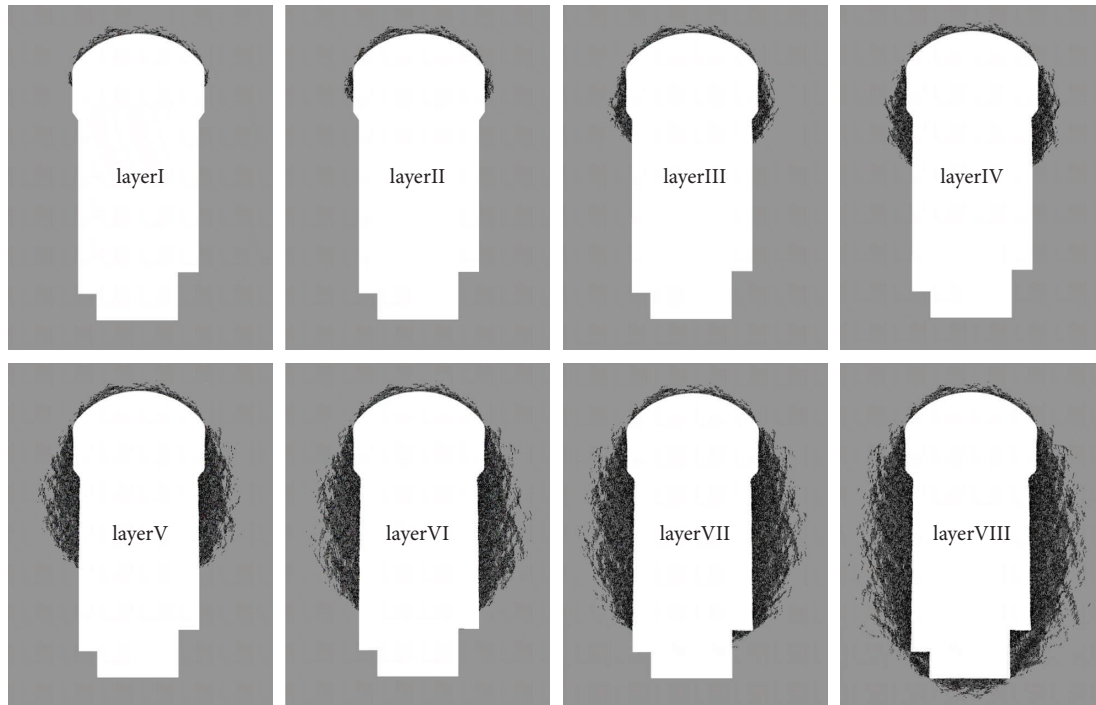


FIGURE 4: Fracture process of surrounding rock during layered excavation of right bank powerhouse.

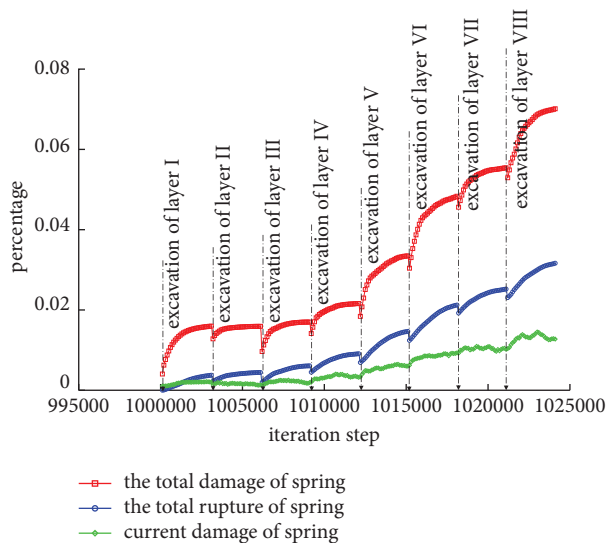


FIGURE 5: The statistics of spring rupture.

state, respectively, and their proportion is far lower than that of the total elements ever damaged. The trend of growth is also relatively stable, and there is no significant S-shaped growth.

From the numerical simulation results, it can be seen that the failure simulation of the surrounding rock in the process of powerhouse excavation reflects the progressive failure characteristics of the surrounding rock. Firstly, after the excavation of powerhouse top arch, the stress of the surrounding rock begins to adjust, the tangential stress of the top arch increases continuously, and the vertical stress decreases continuously, resulting in circumferential splitting

cracks in the top arch. Secondly, with the gradual increase of excavation depth, further stress adjustment of the surrounding rock begins. The local stress concentration begins to appear in the left and right side walls, and the cracks continue to sprout and expand, which provides favorable boundary conditions for the spalling and block falling of the side wall rock mass. And the upward bulging and cracking may occur in the bottom foot.

### 5.2. Comparison between Simulated and Observed Fracture.

Taking the excavation of layer II, layer IV, and layer VI as an example, Figure 6 shows the feedback results of the relaxation depth of the crown arch and side wall after excavation of each layer. In order to facilitate analysis, the characteristic points at different elevations are numbered. Among them, 0 represents measuring point at crown arch of 624.6 m elevation; 1 and 1' represent measuring points at upstream and downstream spandrels of 622.6 m elevation; 2 and 2' represent measuring points at upstream and downstream abutment of 617 m elevation; 3 and 3', 4 and 4', 5 and 5', and 6 and 6' represent measuring points at upstream and downstream side walls of 608 m, 601 m, 591 m, and 583 m elevation, respectively. According to the feedback analysis results:

- (1) During the excavation of layer VI, the relaxation depth of the crown arch increases to a certain extent. The relaxation depth generally increases by about 0.0~0.4 m, and the relaxation depth is 1.6~3.2 m.
- (2) After the excavation of layer VI is completed, the relaxation depth of the upstream and downstream side walls at 608 m increases by about 0.2~0.7 m, and the relaxation depth is 4.5 m and 4.6 m, respectively.



The relaxation depth of upstream and downstream side walls at el. 601 m is 5.1 m and 6.0 m, respectively. The relaxation depth of upstream and downstream side walls at el. 591 m is 4.9 m and 6.0 m, respectively. The relaxation depth of upstream and downstream side walls below el. 583 m is 3.1 m and 3.9 m, respectively.

The simulation results are basically consistent with the deformation characteristics and relaxation depth measured in the field. The model adopted is simplified in the calculation in this paper, without considering any weak zone. The rock mass is considered to be homogeneous and isotropic, resulting in some errors in the calculation results. But on the whole, the numerical calculation can better reflect the failure of the surrounding rock of the underground powerhouse, and the results are reliable.

**5.3. Stress Analysis of Surrounding Rock.** In order to further analyze the failure of the roof arch and side wall of the surrounding rock, the corresponding measuring points are selected at different excavation stages around the tunnel. All measuring points are the points closest to the free face. The specific location distribution is shown in Figure 7. The evolution curves of the minimum principal stress of each measuring point on the left and right side walls with the calculation step are counted, as shown in Figure 8.

The evolution law of the minimum principal stress of the measuring points on the left side wall is basically the same as that of the measuring points on the right side wall. Take the measuring points on left side wall as an example. From layer I to layer VIII, the minimum principal stress of each measuring point first experiences a continuous growth, then drops rapidly at a certain time, and then oscillates and fluctuates near the lower value, and the maximum stress can reach about 70 MPa. Among them, the stress drop time of each measuring point from layer II to layer VIII is the excavation time of this layer, as shown in the figure, which is caused by strong unloading of the surrounding rock during excavation. The measuring points of layer I are slightly different. After the excavation of layer I, the stress does not decrease rapidly, but increases continuously. The possible reason can be closely related to the location of the measuring point, which is selected at the spandrels on both sides. After excavation, the stress concentration here is relatively significant. The stress does not begin to decrease until the excavation of layer II. In the excavation process of subsequent layers, the stress of the measuring point does not decrease to the minimum value, but fluctuates around 50 MPa.

**5.4. Deformation Analysis of Surrounding Rock.** The same measuring points are selected for the deformation analysis of the surrounding rock, and the evolution curve of the lateral displacement of the measuring points on left and right side walls with the calculation step is shown in Figure 9.

The lateral displacement of each measuring point on left and right side walls is symmetrically distributed. The left

measuring point deforms to the right and the right measuring point deforms to the left, resulting in the deformation of the rock mass on both sides to the middle free face after the completion of excavation, which is easy to form spalling and block falling. From layer I to layer VIII, the displacement of measuring points of each layer begins to increase after the excavation of this layer is completed, and the growth trend is approximately linear. The displacement growth rate of the measuring points of layer I is the slowest. After the excavation of layer II is completed, the growth rate remains basically stable, approximately zero. The displacement growth rate of measuring points of layer II is the second. After excavation, the deformation increases slowly. When the excavation of layer III is completed, the displacement increases rapidly. Then, the deformation speed slows down gradually until the excavation is completed, and the final deformation is about 0.2 m. The displacement of measuring points of layers III~VIII starts to increase linearly after the excavation of this layer, and the growth rate of measuring points on each layer is basically the same. At the end of the calculation, the lateral displacement of the measuring point of layer III is the largest, about 0.65 m. This layer is at the position of the rock beam, with the largest deformation.

It should be noted that, since the model for calculation in this paper is simplified, there may be large errors in the calculated data of displacement, and the evolution law of displacement should be paid more attention to.

## 6. Analysis of Size Effect

**6.1. Size Effect of Grid.** Because the crack of CDEM can only develop along the triangular element, in order to accurately simulate the stress field at the crack tip, the mesh is often required to be as small as possible, but it also brings the problem of increasing the amount and time of calculation. On the other hand, large mesh size will increase the yield displacement, resulting in too high calculation strength. Therefore, it is of great significance to study the appropriate grid size to improve the computational efficiency.

Table 6 summarizes the excavation diameter, grid size, and the ratio of grid size to excavation diameter of indoor test simulation, Canadian URL test tunnel simulation, Baihetan exploratory tunnel simulation, and Baihetan powerhouse simulation. It can be seen from the table that the ratio of the minimum grid size to the excavation diameter is about 1/100. At this time, the finite discrete element method CDEM can better simulate the progressive failure of the hard brittle rock and hard brittle surrounding rock.

**6.2. Size Effect of Mechanical Parameters.** Due to the existence of size effect, it is unreasonable to directly apply the mechanical parameters of a specific size of rock mass to engineering design and the establishment of the constitutive model. Similarly, the test results of indoor small-size rock samples cannot be directly extrapolated to the on-site rock mass. The indoor test, exploratory tunnel, and powerhouse are numerical simulations on three different scales. Table 7

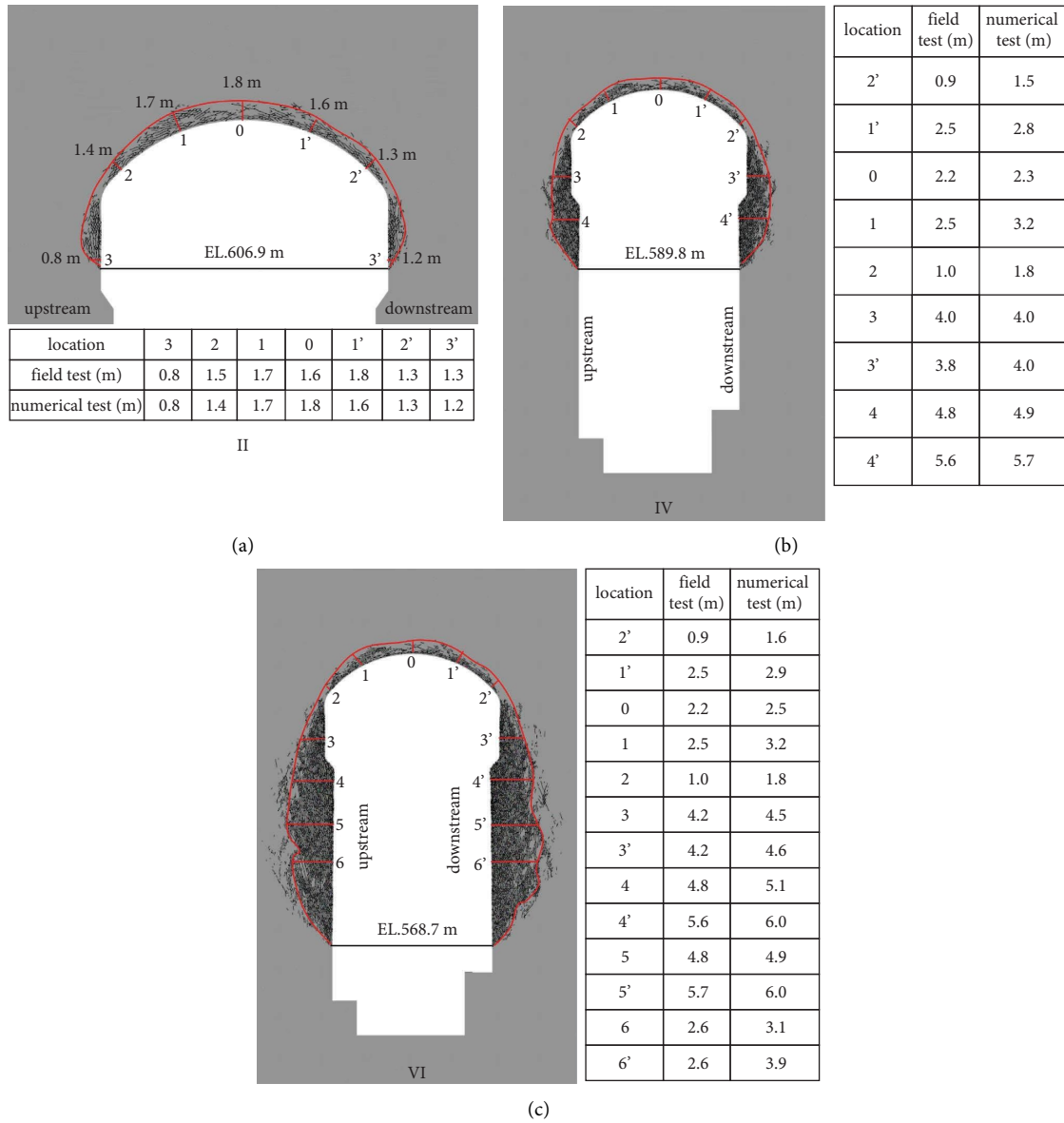


FIGURE 6: Feedback results of the relaxation depth after the excavation of (a) layer II, (b) layer IV, and (c) layer VI.

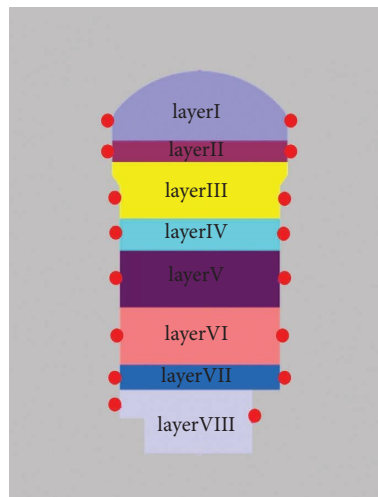


FIGURE 7: Location of measuring points in different excavation stages.

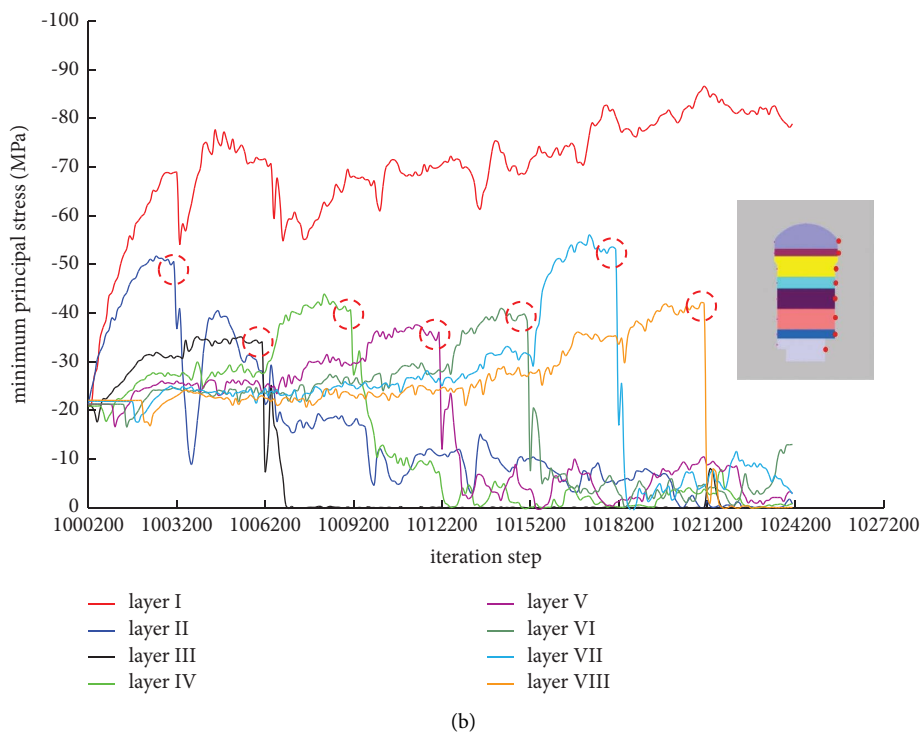
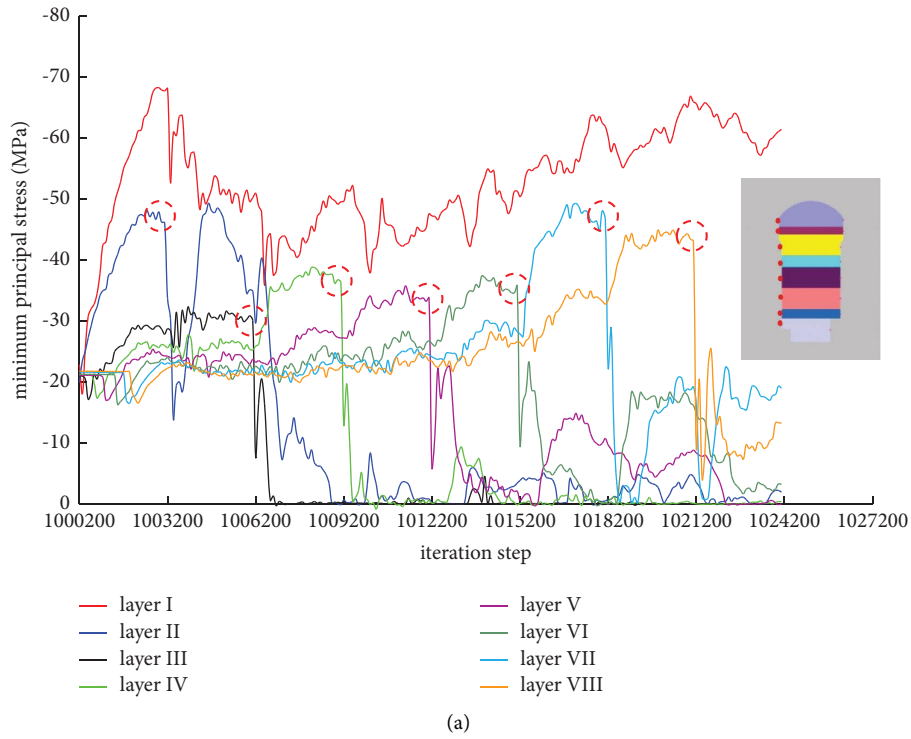


FIGURE 8: The minimum principal stress curve of characteristic points at (a) left and (b) right side walls.

summarizes the various parameters under different scales of numerical simulation. Among them, the indoor test simulation includes two types of basalt of almond basalt and cryptocrystalline basalt.

It can be seen from Table 7 that the mechanical parameters of almond basalt and cryptocrystalline basalt are slightly different, mainly in the value of deformation modulus, cohesion, and tensile strength. As far as the

simulation results of the three scales are concerned, both the deformation parameters and the strength parameters show a certain degree of size effect. The deformation modulus first decreases and then increases from small scale to large scale. The cohesion and tensile strength decrease greatly. The internal friction angle increases gradually, but the increase range is small. The dilatancy angle and fracture energy remain unchanged.

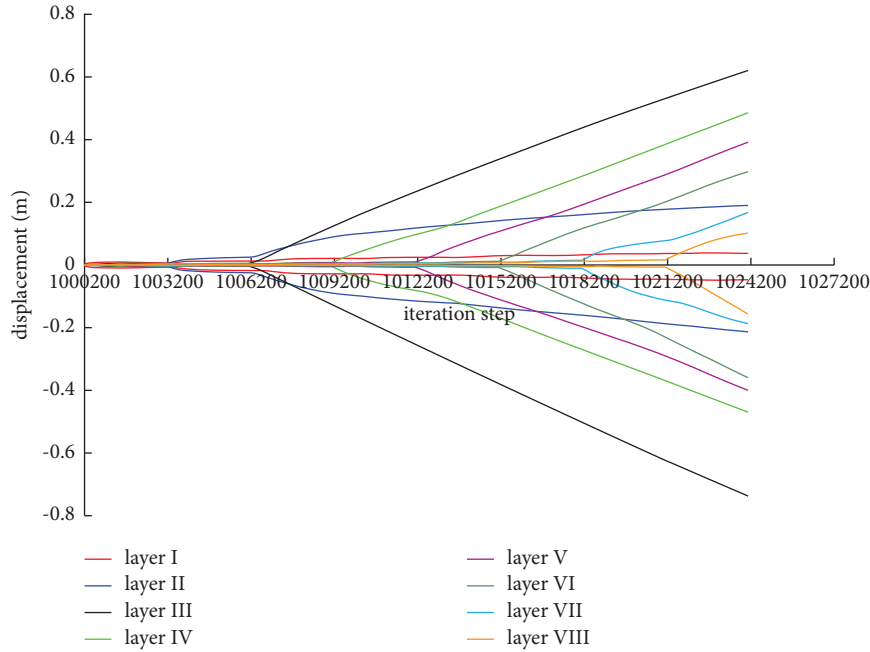


FIGURE 9: The displacement curve of characteristic points at left and right side walls.

TABLE 6: Grids characteristics under different simulation scales.

	Indoor test	URL	Exploratory tunnel	Powerhouse
Test scale	50 mm × 100 mm	60 m × 60 m	40 m × 40 m	600 m × 600 m
Excavation diameter/m	—	3.5	2.5	31
Grid size/m	0.003	0.03	0.03	0.3
Ratio	—	1/117	1/83	1/103

TABLE 7: Mechanical parameters under different simulation scales.

Parameters	Almond basalt	Cryptocrystalline basalt	Exploratory tunnel	Powerhouse
Density $\rho$ (kg/m <sup>3</sup> )	2821	2907	2800	2750
Deformation modulus $E$ (GPa)	38	47	10	26
Poisson's ratio $\nu$	0.19	0.21	0.25	0.25
Cohesion $c$ (MPa)	45	60	25	3.2
Tensile strength $\sigma_t$ (MPa)	9.58	18.5	8	0.3
Initial internal friction angle $\varphi^\circ$	3.9	3.9	5	5.16
Final internal friction angle $\varphi^\circ$	39	39	50	51.6
Dilatancy angle $\psi^\circ$	10	10	10	10
Tensile fracture energy (Pa.m)	50	50	50	50
Shear fracture energy (Pa.m)	500	500	500	500

6.3. Discussion. In the paper about URL test tunnel [19], the key factors of crack propagation simulation using the continuous discontinuous analysis method are discussed, including size effect, constitutive model, and excavation method. The results show that the constitutive model determines the basic form of crack propagation, but in order to accurately simulate the progressive propagation of cracks, the number of elements must be sufficient enough, and the effects of 3D excavation must be considered.

The previous paper focused on the grid size effect of the same engineering scale, while this paper focuses on engineering rock mass of different scales. The results show that, in order to obtain the simulation results as accurate as possible, the number of grids should not only be sufficient enough but also meet the condition that the ratio of grid size to the excavation diameter is about 1/100.

In addition, during the transition from rock to rock mass, due to the weakening of homogeneity and the addition

of joints, the role of cohesion in the brittle failure of rock mass is gradually weakened, while the role of friction is gradually enhanced.

## 7. Conclusions

The progressive failure simulation of the surrounding rock in underground engineering is of great significance for analyzing and ensuring the stability of the surrounding rock. In this paper, the finite discrete element method CDEM is used to simulate the excavation of right bank powerhouse of Baihetan. The fracture evolution of the surrounding rock, the stress, and displacement of characteristic points are analyzed. The calculated results are compared with the relaxation layer depth measured by the acoustic test. At the same time, the size effect of grid and mechanical parameters are discussed when adopting CDEM for simulation. The main conclusions are as follows:

- (1) The fracture depth of the surrounding rock during the layer-by-layer excavation of the powerhouse is basically consistent with the relaxation layer depth measured by the acoustic test, which shows the reliability of the calculation results and reflects the rationality and practicality of the constitutive model and mechanical parameters adopted in this paper
- (2) When the finite discrete element method CDEM is used to simulate the fracture evolution of the surrounding rock in the process of tunnel excavation with different tunnel diameters, good simulation results can be obtained when the minimum size of the grid around the tunnel is controlled at 1% of the tunnel diameter
- (3) Under different scale simulating conditions, the mechanical parameters of rock and rock mass cannot be universal, and the variation laws of deformation parameters and strength parameters cannot be unified, so it needs to be analyzed in specific circumstances

## Data Availability

The data used to support the findings of this study are available from the corresponding author upon request.

## Conflicts of Interest

The authors declare that there are no conflicts of interest.

## Acknowledgments

The work reported here was supported by China Postdoctoral Science Foundation with Grant no. 2021M690999.

## References

- [1] X. T. Feng, H. Xu, S. L. Qiu et al., "In situ observation of rock spalling in the deep tunnels of the China Jinping underground laboratory (2400 m Depth)," *Rock Mechanics and Rock Engineering*, vol. 51, no. 4, pp. 1193–1213, 2018.
- [2] F. Q. Gong, Y. Luo, X. B. Li, X. F. Si, and M. Tao, "Experimental simulation investigation on rockburst induced by spalling failure in deep circular tunnels," *Tunnelling and Underground Space Technology*, vol. 81, pp. 413–427, 2018.
- [3] Y. Luo, F. Q. Gong, D. Q. Liu, S. Y. Wang, and X. F. Si, "Experimental simulation analysis of the process and failure characteristics of spalling in D-shaped tunnels under true-triaxial loading conditions," *Tunnelling and Underground Space Technology*, vol. 90, pp. 42–61, 2019.
- [4] A. C. Shi, C. J. Li, W. B. Hong, G. D. Lu, J. W. Zhou, and H. B. Li, "Comparative analysis of deformation and failure mechanisms of underground powerhouses on the left and right banks of Baihetan hydropower station," *Journal of Rock Mechanics and Geotechnical Engineering*, vol. 14, no. 3, pp. 731–745, 2022.
- [5] H. B. Li, M. C. Liu, W. B. Xing, S. Shao, and J. W. Zhou, "Failure mechanisms and evolution assessment of the excavation damaged zones in a large-scale and deeply buried underground powerhouse," *Rock Mechanics and Rock Engineering*, vol. 50, no. 7, pp. 1883–1900, 2017.
- [6] C. D. Martin, "Seventeenth Canadian geotechnical colloquium: the effect of cohesion loss and stress path on brittle rock strength," *Canadian Geotechnical Journal*, vol. 34, no. 5, pp. 698–725, 1997.
- [7] H. B. Muhlhaus and I. Vardoulakis, "The thickness of shear bands in granular materials," *Géotechnique*, vol. 37, no. 3, pp. 271–283, 1987.
- [8] Z. P. Bazant and G. Pijaudiercabot, "Nonlocal continuum damage, localization instability and convergence," *Journal of Applied Mechanics*, vol. 55, no. 2, pp. 287–293, 1988.
- [9] T. Rabczuk and T. Belytschko, "A three-dimensional large deformation mesh free method for arbitrary evolving cracks," *Computer Methods in Applied Mechanics and Engineering*, vol. 196, no. 29–30, pp. 2777–2799, 2007.
- [10] T. Strouboulis, I. Babuska, and K. Copps, "The design and analysis of the generalized finite element method," *Computer Methods in Applied Mechanics and Engineering*, vol. 181, no. 1–3, pp. 43–69, 2000.
- [11] N. Moes and T. Belytschko, "Extended finite element method for cohesive crack growth," *Engineering Fracture Mechanics*, vol. 69, no. 7, pp. 813–833, 2002.
- [12] T. Belytschko, N. Moes, S. Usui, and C. Parimi, "Arbitrary discontinuities in finite elements," *International Journal for Numerical Methods in Engineering*, vol. 50, no. 4, pp. 993–1013, 2001.
- [13] D. Deb and K. C. Das, "Extended finite element method for the analysis of discontinuities in rock masses," *Geotechnical & Geological Engineering*, vol. 28, no. 5, pp. 643–659, 2010.
- [14] P. A. Cundall and O. D. Strack, "A discrete numerical model for granular assemblies," *Géotechnique*, vol. 29, no. 1, pp. 47–65, 1979.
- [15] K. Duan, Y. L. Ji, W. Wu, and C. Y. Kwok, "Unloading-induced failure of brittle rock and implications for excavation-induced strain burst," *Tunnelling and Underground Space Technology*, vol. 84, pp. 495–506, 2019.
- [16] L. H. Hu, G. S. Su, X. Liang, Y. C. Li, and L. B. Yan, "A distinct element based two-stage-structural model for investigation of the development process and failure mechanism of strain-burst," *Computers and Geotechnics*, vol. 118, Article ID 103333, 2020.
- [17] G. Q. Chen, M. C. He, and F. S. Fan, "Rock burst analysis using DDA numerical simulation," *International Journal of Geomechanics*, vol. 18, no. 3, pp. 1–12, 2018.

- [18] L. Yang, Y. T. Yang, and H. Zheng, "The phase field numerical manifold method for crack propagation in rock," *Rock and Soil Mechanics*, vol. 42, no. 12, pp. 3419–3427, 2021.
- [19] D. N. Zhong, J. L. Chen, H. Zhou et al., "Techniques for progressive failure simulation of hard brittle surrounding rockmass: taking the URL test tunnel as an example," *Advances in Civil Engineering*, vol. 2021, Article ID 8449905, 12 pages, 2021.
- [20] D. N. Zhong, J. L. Chen, H. Zhou, X. R. Chen, and Y. L. Jiang, "Study on progressive failure of hard rock tunnel after excavation under high stress," *Advances in Civil Engineering*, vol. 2022, Article ID 4755417, 13 pages, 2022.
- [21] I. Vazaios, N. Vlachopoulos, and M. S. Diederichs, "Assessing fracturing mechanisms and evolution of excavation damaged zone of tunnels in interlocked rock masses at high stresses using a finite discrete element approach," *Journal of Rock Mechanics and Geotechnical Engineering*, vol. 11, no. 4, pp. 701–722, 2019.
- [22] A. Lisjak, B. Garitte, G. Grasselli, H. R. Müller, and T. Vietor, "The excavation of a circular tunnel in a bedded argillaceous rock (Opalinus Clay): short-term rock mass response and FDEM numerical analysis," *Tunnelling and Underground Space Technology*, vol. 45, pp. 227–248, 2015.
- [23] W. Sun and J. Fish, "Superposition-based coupling of peridynamics and finite element method," *Computational Mechanics*, vol. 64, no. 1, pp. 231–248, 2019.
- [24] W. Sun and J. Fish, "Coupling of non-ordinary state-based peridynamics and finite element method for fracture propagation in saturated porous media," *International Journal for Numerical and Analytical Methods in Geomechanics*, vol. 45, no. 9, pp. 1260–1281, 2021.
- [25] W. Sun, G. Zhang, and Z. L. Zhang, "Damage analysis of the cut-off wall in a landslide dam based on centrifuge and numerical modeling," *Computers and Geotechnics*, vol. 130, Article ID 103936, 2021.
- [26] O. K. Mahabadi, A. Lisjak, A. Munjiza, and G. Grasselli, "Y-geo: new combined finite-discrete element numerical code for geomechanical applications," *International Journal of Geomechanics*, vol. 12, no. 6, pp. 676–688, 2012.
- [27] A. Lisjak, D. Figi, and G. Grasselli, "Fracture development around deep underground excavations: insights from FDEM modelling," *Journal of Rock Mechanics and Geotechnical Engineering*, vol. 6, no. 6, pp. 493–505, 2014.
- [28] A. Munjiza and N. W. M. John, "Mesh size sensitivity of the combined FEM/DEM fracture and fragmentation algorithms," *Engineering Fracture Mechanics*, vol. 69, no. 2, pp. 281–295, 2002.
- [29] L. W. Guo, J. S. Xiang, J. P. Latham, and B. Izzuddin, "A numerical investigation of mesh sensitivity for a new three-dimensional fracture model within the combined finite-discrete element method," *Engineering Fracture Mechanics*, vol. 151, pp. 70–91, 2016.
- [30] A. B. Hawkins, "Aspects of rock strength," *Bulletin of Engineering Geology and the Environment*, vol. 57, no. 1, pp. 17–30, 1998.
- [31] W. J. Darlington, P. G. Ranjith, and S. K. Choi, "The effect of specimen size on strength and other properties in laboratory testing of rock and rock-like cementitious brittle materials," *Rock Mechanics and Rock Engineering*, vol. 44, no. 5, pp. 513–529, 2011.
- [32] H. Masoumi, S. Saydam, and P. C. Hagan, "Incorporating scale effect into a multiaxial failure criterion for intact rock," *International Journal of Rock Mechanics and Mining Sciences*, vol. 83, pp. 49–56, 2016.

## Research Article

# Experimental Study on Dynamic Compression Mechanics of Sandstone after Coupled Alkali-Chemical-Dynamic Interaction

Qi Ping <sup>1,2,3</sup>, Chen Wang,<sup>2,3</sup> Qi Gao,<sup>2,3</sup> Kaifan Shen,<sup>2,3</sup> Yulin Wu,<sup>2,3</sup> Shuo Wang,<sup>2,3</sup> and Xiangyang Li<sup>2,3</sup>

<sup>1</sup>State Key Laboratory of Mining Response and Disaster Prevention and Control in Deep Coal Mine, Anhui University of Science and Technology, Huainan, Anhui 232001, China

<sup>2</sup>Research Center of Mine Underground Engineering, Ministry of Education, Anhui University of Science and Technology, Huainan, Anhui 232001, China

<sup>3</sup>School of Civil Engineering and Architecture, Anhui University of Science and Technology, Huainan, Anhui 232001, China

Correspondence should be addressed to Qi Ping; [ahpingqi@163.com](mailto:ahpingqi@163.com)

Received 4 July 2022; Accepted 20 September 2022; Published 10 October 2022

Academic Editor: Quan Jiang

Copyright © 2022 Qi Ping et al. This is an open access article distributed under the Creative Commons Attribution License, which permits unrestricted use, distribution, and reproduction in any medium, provided the original work is properly cited.

For the purpose of analyzing the effect of the alkaline solutions on the mechanical property of sandstone impact compression, the sandstone specimens of coal mine roadway were corroded in NaOH solution with pH 7 (neutral pure water solution) and pH = 8, 9, 10, 11, and 12 for 28 d, followed by dynamic compression tests using a separated Hopkinson compression bar test device, and the microstructural changes of the specimens were measured by SEM electron microscope scanning equipment. The studies indicate that the degree of damage to the dynamic properties of a sandstone specimen is tightly correlated with the variation of the pH value of the corrosion solution. The corrosion deterioration effect of the strong alkaline solution is most obvious, followed by the weak alkaline solution, and the mechanical properties of the sandstone are relatively stable under a neutral solution. The dynamic compressive strength and dynamic modulus of elasticity of specimens decrease as a quadratic and cubic function, respectively, with the rising pH of the solution. The dynamic peak strain and average strain rate tend to increase with the increase in pH, and they are larger than those of the uncorroded specimens. As the pH of the solution rises, the impact damage of the sandstone specimens intensifies, and the average particle size of the fragments tends to decrease in a quadratic polynomial.

## 1. Introduction

Due to the continuous development of the world economy and modern engineering industry, both the development of mineral resources such as deep oil and natural gas and the deep burial disposal of highly radioactive nuclear waste, as well as the construction of rock works such as tunnels and water conservancy projects, are increasing [1]. The stability of underground rock engineering is usually affected by high ground pressure, high seepage flow [2], and high ground temperature [3]. And the influence of corrosion damage of groundwater on deep underground engineering has attracted the attention of many scholars in recent years, and studies related to static tests of different kinds of rocks under the action of water-rock chemistry have been carried out. Li

et al. [4] utilized the rock mass AE technology to study the uniaxial compression destruction degree of red-bedded soft rocks after being subjected to different acidic pH chemical solutions. Fu et al. [5] used different pH solutions to soak rock samples to explore the effect law of chemical solutions on mechanical properties as well as corrosion mechanism of brilliant rocks for the mining difficulties caused by the intrusion of dense and hard brilliant rocks into coal seams. Huo et al. [6] combined the uniaxial compression test and CT scan test to analyze the basic physical characteristics as well as mechanical property changes of sandstone corroded by acidic solutions. Ding et al. [7] conducted mechanical tests on Longmen Grottoes tuff under different chemical solutions and studied both the strength damage characteristics and solubility properties. Ling et al. [8] conducted

nonequilibrium flow dynamic corrosion tests on black shale immersed in acidic aqueous solutions with different pH and analyzed its deformation and strength characteristic at different deformation and strength characteristics patterns during different soaking periods. Miao et al. [9] carried out static compression mechanical experiments and splitting experiments on marble after soaking in different acidic NaCl solutions, comparing and analyzing the strength deterioration, axial deflection characteristics, and destructive effects of mechanical properties and parameters of granite under different acidic chemical environments. Shen et al. [10] completed a triaxial creep experiment in single fissure granite with simultaneous chemical solution percolation. The comprehensive response mechanism of single fissure rocks under a stress-percolation-chemical coupling environment was studied. Zhou and Chen [11] conducted uniaxial mechanical tests and electron microscope scanning test analysis of granite under different times of erosion by different acidic solutions. Yuan et al. [12] investigated sandstone under the fundamentals of chemical thermodynamics and chemical dynamics. In addition, the energy evolution and damage characteristics of fractured carbonaceous shale subjected to dry-wet circulations were studied. Liu et al. [13] made intact and fissure dip angles of 30°, 45°, and 60° charcoal shale and subjected them to triaxial compression tests under different dry-wet circulations to investigate their effects on the strength, destruction mode, and energy evolution of single fissure charcoal shale.

The surrounding rocks of underground projects are not only eroded by water-chemical solutions but also bear dynamic loads such as mechanical digging, blasting excavation, and seismic impact at the same time [14], which leads to hidden problems in the construction and stability of rock works. It can be seen that the dynamics of the rock is also an important influence on the stability performance and safety performance in underground rock engineering. While the separated Hopkinson compression bar test device is widely used in the tests related to rock dynamic mechanics, Ping et al. [15] studied the problem of how to select a reasonable loading waveform in SHPB experiment. Li et al. [16] investigated the energy dissipation in the impact splitting test of prefabricated single-nodular rock under high strain rate. Yuan and Ma [17] analyzed the influence of water content on the kinetic properties in sandstone after SHPB uniaxial compression test.

There are relatively few tests on rock mechanics under coupled chemical-dynamic conditions. Li et al. [18] conducted impact compression experiments on limestone under erosion in 3 sets of different pH solutions to study its dynamic mechanical properties. Zhang et al. [19] investigated a dynamic tensile mechanical characteristic of limestone with different times of corrosion by the same acidic solution. Li et al. [20] carried out dynamic tensile tests on chert under corrosion in three groups of different acidic solutions and investigated the relationship between dynamic tensile strength and specific energy in the specimens. Ping et al. [21] analyzed the kinetic property changes of the roadway sandstone under different days of corrosion by strong alkali solutions.

Groundwater is generally alkaline, and underground rockworks are subjected to dynamic load impact damage effects in addition to experiencing prolonged corrosion damage by the water-chemical environment [22]. To research the influence of alkaline solution erosion on the dynamic compression characteristics of sandstone, the tests in this study configured NaOH solutions of pH 7, 8, 9, 10, 11, and 12 and placed the sandstone specimens in them for 28 days. Finally, impact compression tests were performed on sandstone specimens at a constant loading rate using a 50 mm diameter split Hopkinson compression bar experimental setup. Several dynamic mechanical parameters of sandstone specimens as well as the microlevel corrosion conditions were analyzed and summarized as influenced by the pH change of the water chemical solution.

## 2. Sandstone Specimen Preparation and Impact Compression Test Procedure

*2.1. Corrosion Specimen Preparation.* The specimens used in this study were obtained from sandstone of the roadway of the Gu Bei coal mine in Huainan City, which had a greyish-white surface.

To increase the homogeneity of the test, the sandstone samples selected for the test were obtained from identical rock. X-ray diffraction (XRD) tests were then performed, and the mineral composition of the rock samples has been analyzed against standard PDF cards. The main components were quartz ( $\text{SiO}_2$ ), albite ( $\text{Na}(\text{Si}_3\text{Al})\text{O}_8$ ), and kaolinite ( $\text{Al}_2\text{Si}_2\text{O}_5(\text{OH})_4$ ), and the molecular formulas of the other minor constituent minerals were  $\text{Al}_2\text{O}_3$ ,  $\text{Fe}_2\text{O}_3$ ,  $\text{CaO}$ ,  $\text{Na}_2\text{O}$ ,  $\text{K}_2\text{O}$ , and  $\text{MgO}$ . The diffraction energy spectrum is shown in Figure 1.

In accordance with the requirements of the rock dynamic properties test protocol [23], the rock has been made into standard specimens of 50 mm in diameter and 25 mm in height through three processes of coring, cutting, and grinding, and control the specimen size error within  $\pm 2$  mm, the two end surface unevenness error of  $\pm 0.05$  mm, and the axis allowable error of  $\pm 0.25^\circ$  [24]. Twenty one specimens were made in total and 3 were selected as uncorroded specimens, while the other 18 have been classified into six sets and subjected to corrosion tests with different pH solutions.

Six sets of aqueous chemical solutions with pH 7, 8, 9, 10, 11, and 12 were used in the experiment, as indicated in Figure 2. Each group of the chemical solution was put into 3 specimens for corrosion, and the corrosion time was 28 d. PHS-25 digital display acidity meter was used to measure the pH variation of its solution regularly every day, and all specimens were removed from the solution after the corrosion test.

*2.2. Dynamical Test Device.* The SHPB experimental equipment used for the impact compression test was provided by the State Key Laboratory of Mining Response and Disaster Prevention and Control in Deep Coal Mines, which is indicated in Figure 3.



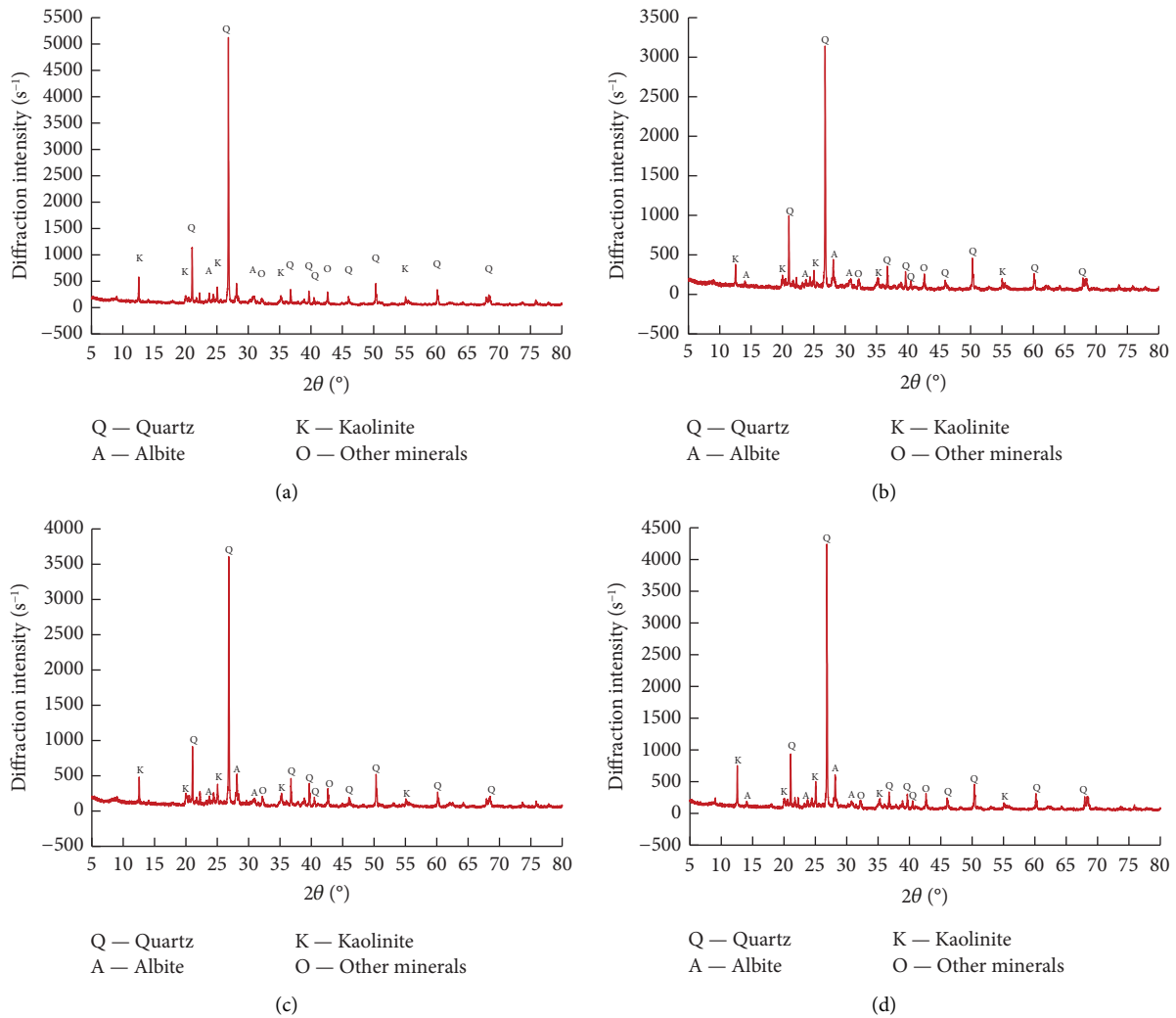


FIGURE 1: X-ray diffraction spectrum. (a) Uncorroded. (b) pH=7. (c) pH=9. (d) pH=12.

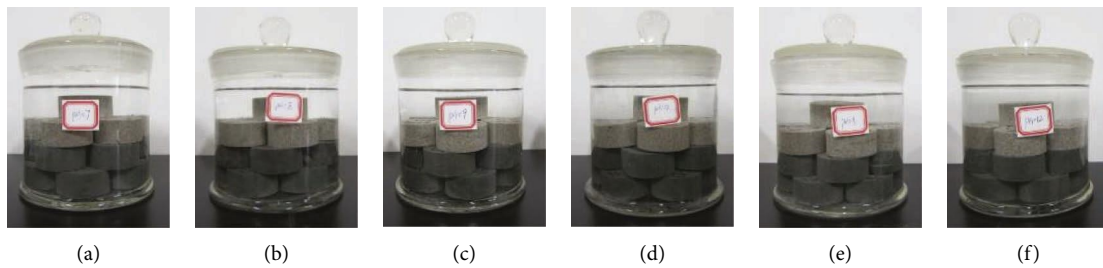


FIGURE 2: Sandstone corroded specimen. (a) pH=7; (b) pH=8; (c) pH=9; (d) pH=10; (e) pH=11; (f) pH=12.



FIGURE 3: SHPB experimental equipment.

The material of the rods is all high-strength 40Cr alloy steel, whose longitudinal wave speed is 5190 m/s. The incident and transmission rods are 2000 mm and 1500 mm long, respectively, and both have a 50 mm diameter. The high-pressure nitrogen gas is released instantaneously to drive the spindle-shaped bullet impact rod to move at a high speed for impact loading. In addition, an appropriate amount of vaseline was applied to both ends of the specimen to reduce the end-face friction effect.

Based on the fundamental of impact dynamic experiment [25], the three-wave method was used to process all data obtained from the data acquisition system [26], so as to calculate the relevant kinetic indicators such as stress  $\sigma(t)$ , strain  $\varepsilon(t)$ , and strain rate  $\dot{\varepsilon}(t)$  of the rock specimen. The calculation principle is indicated as

$$\left. \begin{aligned} \sigma(t) &= \frac{E_0 A_0}{2A_S} [\varepsilon_I(t) + \varepsilon_R(t) + \varepsilon_T(t)] \\ \varepsilon(t) &= \frac{C_0}{L_S} \int_0^t [\varepsilon_I(t) + \varepsilon_R(t) - \varepsilon_T(t)] dt \\ \dot{\varepsilon}(t) &= \frac{C_0}{L_S} [\dot{\varepsilon}_I(t) + \dot{\varepsilon}_R(t) - \dot{\varepsilon}_T(t)] \end{aligned} \right\}, \quad (1)$$

where  $A_0$  and  $A_S$  represent the cross-sectional areas of compression bar and specimen.  $\varepsilon_I(t)$ ,  $\varepsilon_R(t)$ , and  $\varepsilon_T(t)$  represent the incident stress wave, reflected stress wave, and transmitted stress wave in the moment  $t$ , respectively.  $E_0$  and  $C_0$  represent the modulus of elasticity of the compression bar and the longitudinal wave speed.  $L_S$  represent the length of the specimen;  $t$  is the continuation time of the stress wave.

**2.3. Solution pH Variation.** Starting from the immersion of all sandstone specimens into the solution, the pH change of the solution was measured regularly every day using a PHS-25 digital display acidity meter, and the pH change curve of each solution with time is shown in Figure 4.

As shown in Figure 5, the pH of the strong alkali solution (pH = 11, 12) decreases continuously and tends to be neutral as the corrosion time increases; the pH of the weak alkali solution (pH = 8) increases slightly; the solutions with pH of 9 and 10 change less and level out; while the pH of neutral pure water decreases slightly and tends to be weakly acidic. Compared with the weak alkali solution, the concentration of  $\text{OH}^-$  in the strong alkali solution is higher, and the chemical reaction rate with sandstone mineral components is faster and more fully reacted, resulting in the consumption of  $\text{OH}^-$  in the strong alkali solution which is much larger than that in weak alkali solution; thus, its pH decreases significantly. In addition, the pH change of each solution has a time effect. During the pre-water-rock chemistry phase, some mineral components in sandstone react chemically with  $\text{OH}^-$  in solution or hydrolyze with solution, accompanied by the consumption of original substances and the generation of precipitation and other substances, which leads to a more significant change of solution pH, and during the late stage of water-rock action, due to the continuous consumption of some mineral components in sandstone, the chemical reaction rate decreases; thus, the change of solution pH is relatively small and tends to level off gradually.

With reference to the previous studies [27–30] and combined with the mineral composition of sandstone obtained from XRD tests, the equations of water-rock chemical reactions occurring in different water chemical solutions tested in this study can be summarized as follows.

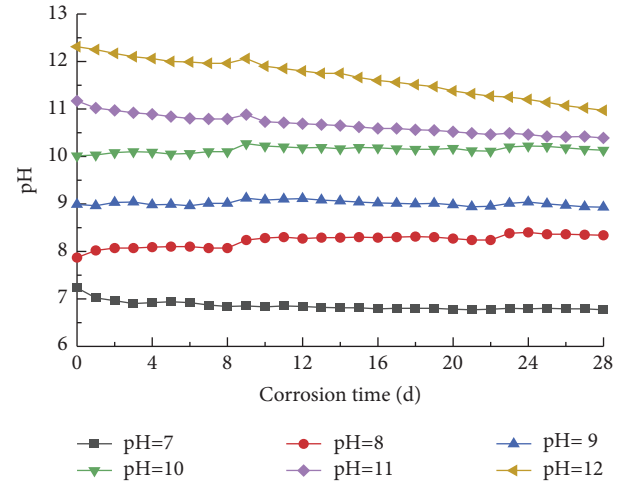


FIGURE 4: Curves of pH value variation with time in hydrochemical solutions.

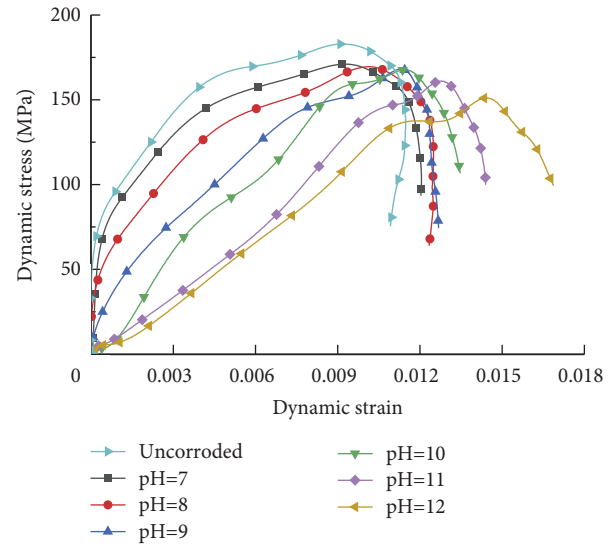
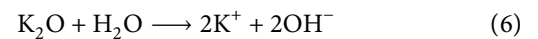
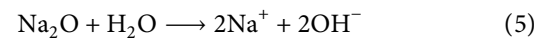
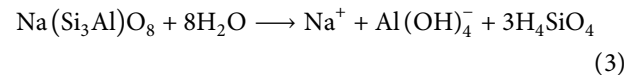
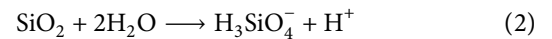
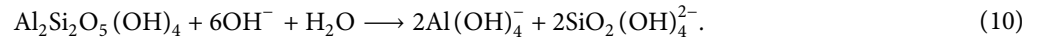
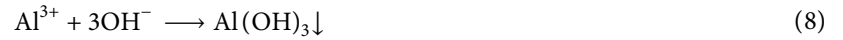


FIGURE 5: Dynamic stress-strain curves on sandstone specimens under erosion with different pH solutions.

The hydrolysis reactions of some mineral components of sandstone in neutral pure water solutions occur as shown in equations (2)–(6):



The main chemical reactions occurring in alkaline solutions with sandstone mineral components are shown in (10):



In addition to the above chemical reaction equations, water-rock chemistry also includes dissolution and dissolution, which will likewise lead to an increase in the degree of microscopic chemical damage in sandstone specimens, thus causing different degrees of deterioration in their dynamic mechanical properties.

### 3. Experimental Discussion and Analysis

**3.1. Sandstone Dynamic Stress-Strain Variation.** A dynamic compression test was carried out under a shock air pressure of 0.50 MPa, and the dynamic stress-strain curves of sandstone specimens were without corrosion and after corrosion with different pH solutions (see Figure 5).

According to the analysis, the dynamic mechanical properties in specimens show a deterioration trend after erosion by different pH solutions, and the greatest decrease in dynamic compressive strength is after erosion by a strong alkali solution, and the corresponding breaking strain increases sharply, followed by corrosion by a weak alkali solution, while the smallest decrease in dynamic compressive strength is after erosion by a neutral solution. After preliminary analysis, the pH value is a significant factor affecting the variation of dynamic mechanical parameters of the rock.

Figures 6 and 7 and Table 1 show the variation of dynamic compressive strength and the dynamic peak strain for the specimens under different pH solution conditions.

The results obtained showed that  $\sigma_d$  for the uncorroded specimens was up to 183.67 MPa. However,  $\sigma_d$  of the sandstone specimens showed a quadratic decreasing trend after 28 d of corrosion treatment by six pH solutions, in which the strength of the specimens decreased the least by 6.58% after corrosion by neutral solution, while the maximum decrease was 17.11% at pH 12. The corresponding  $\varepsilon_d$  of the sandstone specimens had an increase of 21.34%, 35.30%, 42.15%, 49.99%, 53.14%, and 82.01%, respectively, compared with the uncorroded sandstone specimens. Clearly, the growth of  $\varepsilon_d$  of sandstone specimens under the corrosion of neutral and weak alkaline solutions is relatively small, and the growth of  $\varepsilon_d$  increases gradually as the alkalinity increases, reaching its peak under the corrosion of strong alkaline solutions with pH 12. This is because some of the constituent minerals decompose and produce precipitation and other substances after chemical reaction under an alkaline solution, which leads to the destruction of the original internal structure and the expansion and increase of the number of microcracks again, thus showing the deterioration of  $\sigma_d$  and the increase of  $\varepsilon_d$  amplitude.

**3.2. Variation of Dynamic Modulus of Elasticity and Average Strain Rate.** The changes in modulus of dynamic elasticity as well as average strain-rate of the specimens corroded by different pH solutions are shown in Figures 8 and 9, respectively.

From Figure 8,  $E_d$  decreases with increasing pH in a cubic function, and the higher the pH of the solution, the greater the decrease. Moreover, the percentage loss of  $E_d$  value was 5.12%, 5.73%, 6.48%, 13.95%, 18.84%, and 38.45% after corrosion of specimens with different pH solutions compared with uncorroded specimens. The reasons are as follows. As the pH value increases, the solution erosion effect is enhanced, and the internal microcracks of sandstone specimens are extended continuously, leading to a gradual decrease of the resistance to deformation of sandstone specimens, and the deterioration of impact mechanical characteristics of specimens in strong alkaline solution corrosion is more obvious compared with neutral pure water solution and weak alkaline solution.

From Figure 9,  $\dot{\varepsilon}$  showed a quadratic polynomial positive correlation with increasing pH of the solution, as well as the higher the pH, the larger the rise in  $\dot{\varepsilon}$ . Moreover, the  $\dot{\varepsilon}$  rise values were 1.04%, 3.42%, 10.80%, 20.03%, 28.38%, and 63.78% after the corrosion of specimens with different pH solutions compared with the uncorroded specimens. It can be observed that the variation in  $\dot{\varepsilon}$  of sandstone after corrosion in a neutral solution is small and can be neglected, while in an alkaline solution,  $\sigma_d$  decreases, as well as  $\dot{\varepsilon}$  rises as pH increases, which represents a more significant strain-rate effect.

**3.3. Corrosion Microscopic Damage Mechanism of Sandstone Specimens.** Figure 10 shows the SEM electron microscope scanning test images of the specimens under the corrosion of different pH solutions.

As it is observed in Figure 10, uncorroded sandstone is structurally dense with occasional secondary pores. While in neutral pure water solution, sandstone undergoes just a little hydrolytic reaction, making the specimen porous. While in the alkaline surface is relatively smooth, the degree of deterioration damage is small. In an alkaline solution, sodium feldspar and other major mineral components in sandstone react with  $\text{OH}^-$  to produce free  $\text{K}^+$  and  $\text{Na}^+$ , while a small amount of  $\text{Al}^{3+}$  and  $\text{Ca}^{2+}$  combine with  $\text{OH}^-$  to produce a white precipitate, which can be observed in SEM images as a little white crystal on the surface of sandstone specimens. And in alkaline solutions with different pH solutions, the intensity of chemical reactions occurring varies. It can be

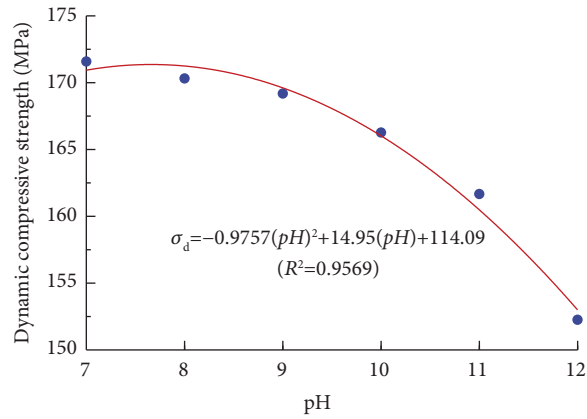


FIGURE 6: Relationship between dynamic compressive strength and pH.

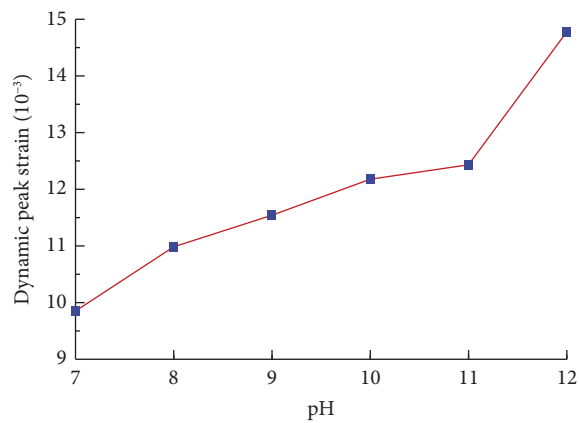


FIGURE 7: Relationship between dynamic peak strain and pH.

TABLE 1: Selected dynamic mechanical parameters of some corrosion specimens.

pH	Specimen number	Dynamic compressive strength $\sigma_d$ (MPa)	Dynamic peak strain $\epsilon_d/10^{-3}$	Dynamic modulus of elasticity $E_d$ (GPa)	Average strain rate $\dot{\epsilon}$ (s <sup>-1</sup> )
Uncorroded	GB41-19	183.67	8.118	18.463	66.654
7	GB41-03	171.59	9.850	17.518	67.243
8	GB41-06	170.32	10.983	17.404	68.829
9	GB41-07	169.19	11.540	17.267	73.744
10	GB41-12	166.27	12.176	15.888	79.885
11	GB41-13	161.66	12.432	14.985	85.436
12	GB41-17	152.25	14.776	11.365	109.001

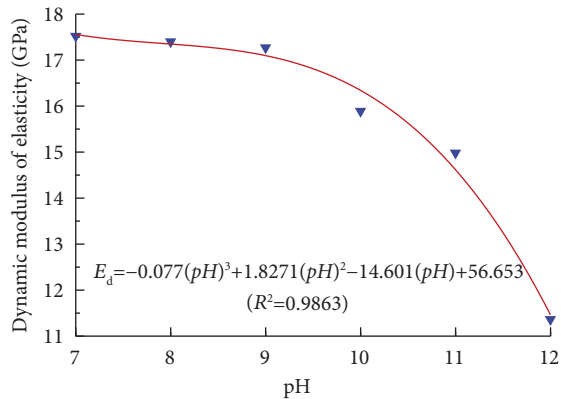


FIGURE 8: Relationship between dynamic elastic modulus and pH.

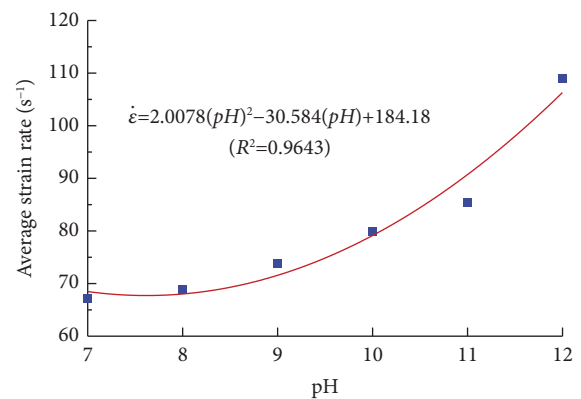


FIGURE 9: Relationship between average strain rate and pH.

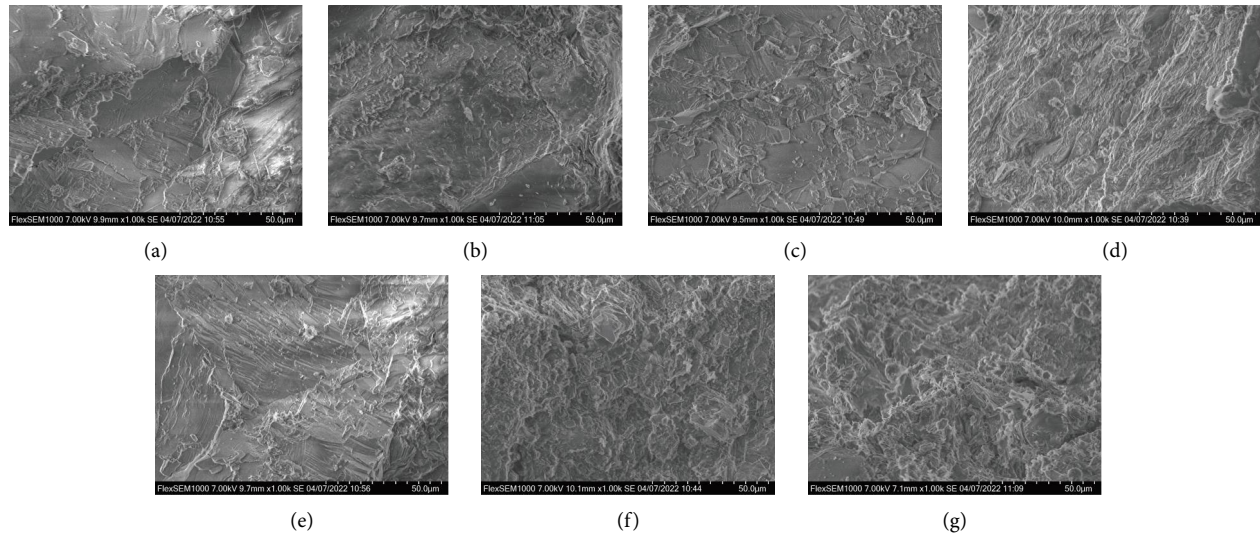


FIGURE 10: SEM images of specimens after corrosion in various pH solutions. (a) Uncorroded. (b) pH=7 (c) pH=8. (d) pH=9. (e) pH=10. (f) pH=11. (g) pH=12.

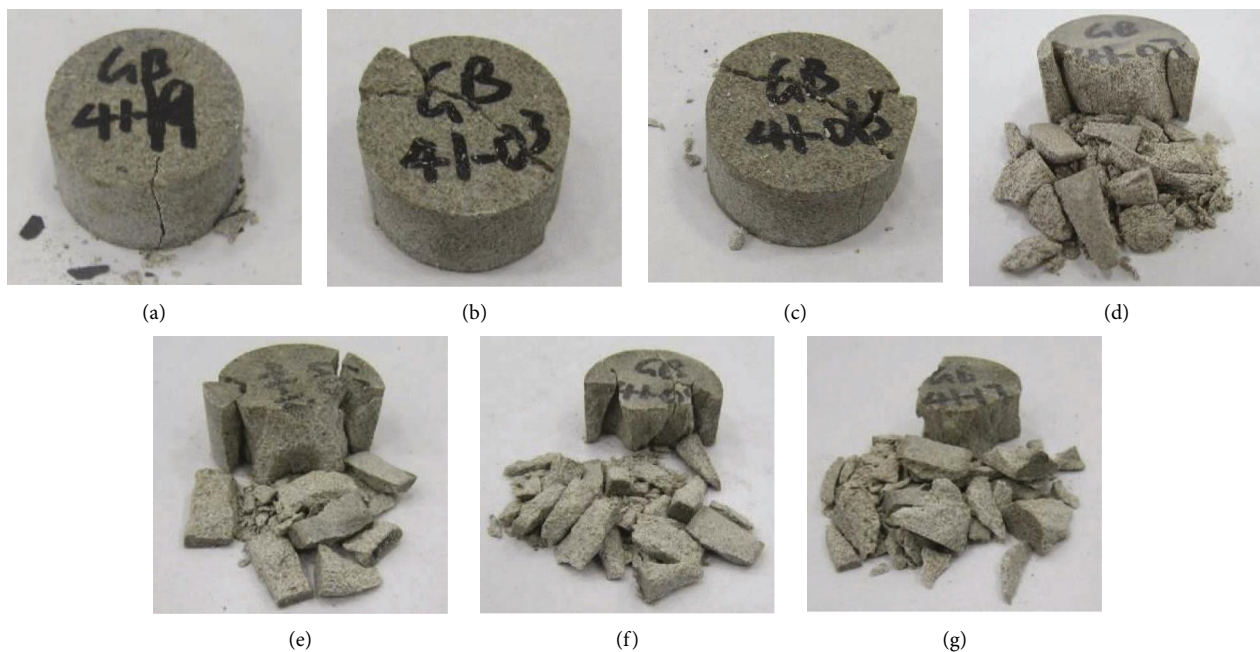


FIGURE 11: Impact damage forms of sandstone corroded by different pH solutions. (a) Uncorroded. (b) pH=7. (c) pH=8. (d) pH=9. (e) pH=10. (f) pH=11. (g) pH=12.

observed that microcracks in the internal structure of sandstone start to expand after soaking in neutral solutions, and a small amount of microporosity appears in sandstone in weakly alkaline solutions. With the enhancement of alkalinity, the corrosion phenomenon on the surface of the specimen becomes more and more serious, and the number of secondary pores and microcracks inside gradually increases, no longer maintaining the original compact structure. Therefore, the degree of sandstone damage caused by erosion of strong alkali solutions is greatest, followed by weak alkali solutions, and the neutral solution is the least, which is corroborated with the previous law that the

deterioration of dynamic mechanical properties increases with the increasing pH value.

**3.4. Specimen Impact Damage Forms.** As it is observed in Figure 11, compared with the uncorroded specimens, the sandstone specimens were less damaged after corrosion by neutral and weak alkaline solutions, as well as the broken form was characterized by the basic integrity of the specimen surface and the presence of fragments of larger size, accompanied by a small amount of debris. As the pH value of the corrosion solution rose from 9 to 12, it was observed that

TABLE 2: Sieving results of sandstone specimens in broken pieces.

pH	Number	Diameter of sieve hole (mm)									Total mass (g)	Average particle size of fragments (mm)
		0.15	0.3	0.6	1.18	2.36	4.75	9.5	13.2	16.0		
7	GB41-03	0.21	0.18	0.30	0.25	0.35	0.90	3.71	4.53	115.62	126.05	15.47
8	GB41-06	0.17	0.15	0.32	0.30	0.26	3.48	4.20	0.00	121.80	130.68	15.35
9	GB41-07	0.56	0.54	0.81	0.86	1.23	3.25	10.22	4.18	105.08	126.73	14.63
10	GB41-12	0.78	0.75	1.34	1.39	3.41	8.81	7.04	10.69	88.83	123.04	13.67
11	GB41-13	1.24	1.05	1.64	1.58	2.73	10.98	15.94	19.72	71.15	126.03	12.79
12	GB41-17	2.16	1.89	2.79	2.76	5.44	22.26	17.93	10.23	58.14	123.60	11.00

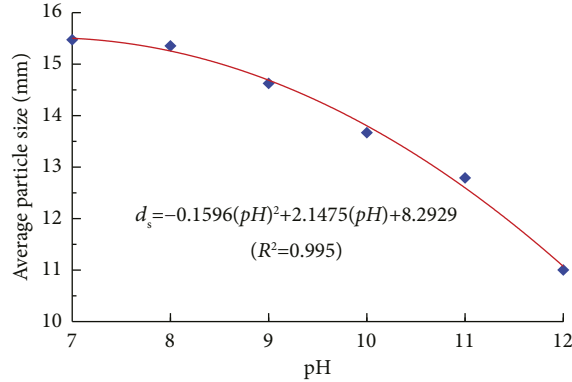


FIGURE 12: Variation of average particle size of sandstone specimens' fractions with pH.

the integrity of the specimen decreased, and both fracture plane and fragments increased significantly. As the solution pH reached 12, the fragmentation pattern in specimens was mainly small-sized fragments.

Study the extent of damage in rock specimens subjected to dynamic load impact based on quantitative analysis. The average particle size of the fragment's  $d_s$  [31] was taken as

$$d_s = \frac{\sum(r_i d_i)}{\sum r_i}, \quad (11)$$

where  $d_i$  represents the diameter with different grades of sieve holes, mm, and  $r_i$  represents the percentage of mass of crushed pieces relative to  $d_i$ .

According to China GB/T14685-2011 "pebbles and gravel for construction" and GB/T14684-2011 "sand for construction," 0.15, 0.3, 0.6, 1.18, 2.36, 4.75, 9.5, 13.2, and 16.0 mm square hole sand and gravel sieves were selected, using Zhejiang Geotechnical Instrument Manufacturing Ltd. Produced STSJ-4 digital high-frequency vibrating sieve machine to test pieces of broken pieces of sieving and use the balance to weigh the mass of its broken pieces under different sieve holes. The statistics of the sieving experimental results are summarized in Table 2. The variation in average particle size of sandstone specimens in dynamic compression test fragments after corrosion with different pH solutions versus pH is shown in Figure 12.

As it is shown in Figure 12, the average particle size of fragments after impact decreases as a quadratic polynomial when the pH increases, i.e., the more alkaline the solution is, the more serious the corrosion damage of the sandstone specimen is, which results in the aggravation of the impact

damage to the specimen and the smaller the average grain diameter size of the fragments.

#### 4. Conclusions

For the purpose of studying the dynamic mechanical property changes of sandstone corroded by alkaline solutions, solutions with pH 7~12 were prepared to corrode the sandstone specimens, and then, the dynamic impact compression test under the same air pressure was carried out using the SHPB device, and the resulting specimens were sieved to obtain the following three conclusions:

- (1) As corrosion time extends, the pH value of strong alkali solution (pH = 11,12) decreases continuously and tends to be neutral; the pH value of weak alkali solution (pH = 8) increases slightly; the alkaline solution and neutral aqueous solution with pH 9 and 10 change less and are relatively stable.
- (2) With the increase of solution pH,  $\sigma_d$  and  $E_d$  of sandstone corroded specimens presented varying extent of deterioration, with a maximum decrease of 17.11% and 38.45%, respectively, and  $\varepsilon_d$  as well as  $\dot{\varepsilon}$  increased accordingly. Among them, the kinetic macroscopic parameters of the specimens deteriorated the most after the corrosion of strong alkali solution and the least after the corrosion of neutral solution.
- (3) The effect of chemical corrosion on sandstone specimens was strengthened with the rise of solution pH. The larger the pH, the more serious the impact damage. The average particle size of specimen fragments was also reduced, and the average particle size of fragments showed a quadratic polynomial decreasing relationship with the rise of solution pH value.

In this study, only the air pressure of 0.5 MPa was used for the impact compression experiment of sandstone under corrosion, while strain-rate effects are commonly found in the kinetic properties of rocks, so in-depth research and analysis are still needed in the subsequent tests.

#### Data Availability

The data supporting the results of this study can be obtained from the corresponding author upon request.

## Conflicts of Interest

The authors declare that there are no conflicts of interest with the publication of this paper.

## Acknowledgments

This research was funded by the National Natural Science Foundation of China (nos. 52074005 and 52074006), Anhui Provincial Natural Science Foundation (no. 1808085ME134), Anhui Postdoctoral Science Foundation (no. 2015B058), and Anhui University of Science and Technology Graduate Innovation Fund Project (no. 2021CX2032). The authors thank the Engineering Research Center of Underground Mine Construction, Ministry of Education, and Anhui University of Science and Technology, State Key Laboratory of Mining Response and Disaster Prevention and Control in Deep Coal Mine, for providing the experiment conditions.

## References

- [1] C. B. Zhou, Y. F. Chen, Q. H. Jiang, and W. Lu, "On generalized multi-field coupling for fractured rock masses and its application to rock engineering," *Chinese Journal of Rock Mechanics and Engineering*, vol. 27, no. 7, pp. 1329–1340, 2008.
- [2] Y. S. Liu, X. H. Diao, and Z. L. Chen, "Dynamic mechanical properties of surrounding rock under chemical corrosion," *Journal of Nanjing Forestry University (Natural Sciences Edition)*, vol. 38, no. 6, pp. 175–178, 2014.
- [3] Q. Ping, M. J. Wu, and P. Yuan, "Experimental study on dynamic mechanical properties of high temperature sandstone under impact loads," *Chinese Journal of Rock Mechanics and Engineering*, vol. 38, no. 4, pp. 782–792, 2019.
- [4] X. N. Li, X. Y. Wu, and S. M. Gao, "Experiment study on uniaxial compression acoustic emission characteristics of red-bed soft rock in chemical environment," *Journal of Railway Science and Engineering*, vol. 12, no. 6, pp. 1336–1340, 2015.
- [5] Y. K. Fu, Y. K. Yang, and Y. K. Guo, "Corrosion mechanism of lamprophyre under water chemistry," *Journal of Taiyuan University of Technology*, vol. 51, no. 3, pp. 404–410, 2020.
- [6] R. K. Huo, F. Han, and S. G. Li, "Experimental study on physicochemical and mechanical properties of acid-corroded sandstone," *Journal of Xi'an University of Architecture and Technology*, vol. 51, no. 1, pp. 21–26, 2019.
- [7] W. X. Ding, J. P. Chen, and T. Xu, "Mechanical and chemical characteristics of limestone during chemical erosion," *Rock and Soil Mechanics*, vol. 36, no. 7, pp. 1825–1830, 2015.
- [8] S. X. Ling, X. Y. Wu, and C. W. Sun, "Experimental study of chemical damage and mechanical deterioration of black shale due to water-rock chemical action," *Journal of Experimental Mechanics*, vol. 31, no. 4, pp. 511–524, 2016.
- [9] S. J. Miao, M. F. Cai, and D. Ji, "Damage effect of granite's mechanical properties and parameters under the action of acidic solutions," *Journal of China Coal Society*, vol. 41, no. 4, pp. 829–835, 2016.
- [10] L. F. Shen, X. T. Feng, and P. Z. Pan, "Experimental research on mechano-hydro-chemical coupling of granite with single fracture," *Chinese Journal of Rock Mechanics and Engineering*, vol. 29, no. 7, pp. 1379–1388, 2010.
- [11] Q. Zhou and Y. L. Chen, "The experimental study on mechanical properties of granite after acid solution corrosion," *Journal of Water Resources and Water Engineering*, vol. 29, no. 1, pp. 225–231, 2018.
- [12] W. Yuan, X. R. Liu, and Y. Fu, "Chemical thermodynamics and chemical kinetics analysis of sandstone dissolution under the action of dry-wet cycles in acid and alkaline environments," *Bulletin of Engineering Geology and the Environment*, vol. 78, no. 2, pp. 793–801, 2019.
- [13] X. X. Liu, Y. Li, and Z. J. Fan, "Research on energy evolution and failure characteristics of single fissure carbonaceous shale under drying-wetting cycles," *Rock and Soil Mechanics*, vol. 43, no. 7, pp. 1–12, 2022.
- [14] L. Y. Yu, Z. Q. Zhang, and J. Y. Wu, "Experimental study on the dynamic fracture mechanical properties of limestone after chemical corrosion," *Theoretical and Applied Fracture Mechanics*, vol. 108, 2020.
- [15] Q. Ping, M. J. Wu, and Q. Y. Ma, "Comparison and analyses on reasonable loading waveform in SHPB experiment," *Chinese Journal of Underground Space and Engineering*, vol. 13, no. 6, pp. 1499–1505, 2017.
- [16] M. Li, L. Qiao, and Q. W. Li, "Energy dissipation analysis of precast single jointed rock SHPB splitting test under high strain rate," *Journal of Engineering*, vol. 39, no. 7, pp. 1336–1343, 2017.
- [17] P. Yuan and R. Q. Ma, "Split Hopkinson pressure bar tests and analysis of coal mine sandstone with various moisture contents," *Chinese Journal of Rock Mechanics and Engineering*, vol. 34, no. S1, pp. 2888–2893, 2015.
- [18] G. L. Li, L. Y. Yu, and H. J. Su, "Dynamic properties of corroded limestone based on SHPB," *Chinese Journal of Rock Mechanics and Engineering*, vol. 37, no. 9, pp. 2075–2083, 2018.
- [19] Z. Q. Zhang, L. Y. Yu, and G. L. Li, "Experimental research on dynamic tensile mechanics of limestone after chemical corrosion," *Chinese Journal of Geotechnical Engineering*, vol. 42, no. 6, pp. 1151–1158, 2020.
- [20] S. S. Li, L. Y. Yu, and G. L. Li, "Experimental study on dynamic tensile strength of limestone after acid corrosion," *Jiangsu Construction*, vol. 6, pp. 88–92, 2018.
- [21] Q. Ping, C. Wang, Q. Gao et al., "Experimental study on dynamic mechanical properties of sandstone corroded by strong alkali," *Applied Sciences*, vol. 12, no. 15, p. 7635, 2022.
- [22] G. L. Feng, X. T. Feng, Y. X. Xiao et al., "Characteristic microseismicity during the development process of intermittent rockburst in a deep railway tunnel," *International Journal of Rock Mechanics and Mining Sciences*, vol. 124, Article ID 104135, 2019.
- [23] Chinese Society for Rock Mechanics and Engineering, "T/CSRME 001-2019 Technical specification for testing method of rock dynamic properties [EB/OL], 2019, <http://www.ttbz.org.cn/Home/Show/10253>.
- [24] The National Standards Compilation Group of Peoples Republic of China, *GB/T 2 3561-2 010 Methods for Determining the Physical and Mechanical Properties of Coal and Rock*, Standards Press of China, Beijing, China, 2010.
- [25] X. B. Li and D. S. Gu, *Rock Impact Dynamics*, pp. 2–93, Central South University of Technology Press, Changsha, China, 1994.
- [26] L. L. Wang, *Foundation of Stress Waves*, pp. 39–64, National Defense Industry Press, Beijing, China, 2nd edition, 2010.
- [27] X. Z. Feng, N. Qin, and L. Z. Cui, "Experimental study on triaxial creep and fine view damage of sandstone under the action of water-chemical-freeze-thaw cycles," *Chinese Journal of Applied Mechanics*, vol. 38, no. 4, pp. 1383–1391, 2021.

- [28] P. Wang, *Impact of Chemistry- Temperature- Stress Coupling on Mechanical Properties of Rocks*, University of Shanghai for Science and Technology, China, Shang Hai Shi, 2014.
- [29] N. Zhang, S. B. Wang, and C. G. Yan, "Pore structure evolution of hydration damage of mudstone based on NMR technology," *Journal of China Coal Society*, vol. 44, no. S1, pp. 139–146, 2019.
- [30] T. L. Han, J. P. Shi, and Y. S. Chen, "Laboratory investigations on the mechanical properties degradation of sandstone under the combined action between water chemical corrosion and freezing and thawing cycles," *Journal of Hydraulic Engineering*, vol. 47, no. 5, pp. 644–655, 2016.
- [31] Q. Ping, C. L. Zhang, and H. J. Sun, "Experimental study on dynamic characteristics of sandstone after different high temperature cyclings," *Journal of Mining & Safety Engineering*, vol. 38, no. 5, pp. 1015–1024, 2021.



## Research Article

# Study on Strength Enhancement Factors of Cement-Stabilized Recycled Aggregate

Congcong Su <sup>1</sup> and Lihui Li <sup>1,2</sup>

<sup>1</sup>School of Civil Engineering, Xuchang University, Xuchang 461000, China

<sup>2</sup>The Scientific Research Innovation Team of Xuchang University (2022CXTD008), Xuchang, China

Correspondence should be addressed to Lihui Li; [12007062@xcu.edu.cn](mailto:12007062@xcu.edu.cn)

Received 19 July 2022; Revised 22 August 2022; Accepted 29 August 2022; Published 10 September 2022

Academic Editor: Guang-Liang Feng

Copyright © 2022 Congcong Su and Lihui Li. This is an open access article distributed under the Creative Commons Attribution License, which permits unrestricted use, distribution, and reproduction in any medium, provided the original work is properly cited.

With the rapid development and urbanization, huge amounts of construction and demolition (C & D) waste are produced. In order to protect the environment and conserve natural resources, promoting renewable materials, with C & D waste as raw materials, is imperative. However, the poor mechanical properties of recycled aggregate hinder its applicability in projects. In this study, two kinds of recycled aggregates, that is, concrete and brick slag, were strengthened with polyvinyl alcohol (PVA) solution, and the optimal strengthening time and soaking concentration were determined. Recycled mixed aggregate and brick slag were designed with two kinds of graded recycled aggregate. Recycled cement-stabilized crushed stone specimens were prepared for a 7-day unconfined compression and freeze-thaw cycle test. The results showed that the recycled aggregate strength was improved to a certain extent, while the improvement of brick slag aggregate was more pronounced. The recycled mixture with less cement-stabilized brick slag can be used for the base course of heavy traffic secondary highways before strengthening. Cement-stabilized unreinforced brick slag has shown low strength, so it is not suitable to be used as a base on heavy traffic roads. The strengthened cement-stabilized recycled mixture and cement-stabilized brick slag could meet the requirements of heavy traffic class I and class II highways, respectively. When the cement grade, dosage, and grading type were kept the same, the strength of cement-stabilized crushed stone prepared with larger aggregates was slightly lower. After the freeze-thaw cyclic test, the strength loss of the recycled stable gravel was low, and its durability did not significantly improve after the reinforcement of recycled aggregate.

## 1. Introduction

The exploitation of natural sand causes great damage to the local environment. Sand mining can change the landform of the riverbed, reduce the visibility of water bodies, destroy the living environment of aquatic organisms and the ecosystem of the whole river, and change the overall local environment [1, 2]. Stone mining also causes great damage to the surrounding environment. A series of byproducts such as dust, wastewater, noise, and waste residue are produced during stone mining and processing, damaging the construction and the surrounding living environment [3–5]. It requires new sand and stone resources. In order to ensure the project's quality, new sand and stone will be used to partially or completely replace natural aggregates to alleviate the

contradiction between the supply and demand of natural sand and stone. Construction of urban infrastructure, demolishing rural houses, urban waste buildings, and abandoned overpasses produce a lot of construction and demolition (C & D) waste, accounting for 30%–40% of the total urban waste [6–9].

Construction waste treatment has always been a problem faced by the world [10]. Recyclable green building materials are produced through different processing techniques, such as the crushing and sieving of solid waste, which can achieve the sustainable development of building materials. Such techniques have been recognized and supported by the global construction industry [11, 12]. The types of C & D waste are mainly affected by urban construction, demolition, and new construction, including concrete, glass, ceramics,

bricks, wood, coal gangue, rubber, and roof tiles [13]. In addition, the composition of construction waste in demolishing old buildings is closely related to the type and structural form of buildings. For example, in the old brick-concrete structure, bricks, tiles, and concrete account for 80% of the total, and the rest are lime, wood, broken glass, and slag. Kadir and Mohajerani [14] reviewed the current research progress in the production of sintered clay bricks using various wastes. It was shown that adding different materials to bricks had different effects on the mechanical and physical properties of bricks. It has now been found that most of the various wastes added to the production of sintered clay bricks positively affect the performance of bricks.

Cement concrete is the most commonly used material in infrastructure, such as roads, buildings, and bridges [15]. Structures reaching the end of their service life, housing demolition, and highway reconstruction result in a great amount of waste concrete being generated [16]. Recycling concrete waste is of great help to society, and it has considerable economic benefits in reducing the accumulation of building materials, vehicle transportation costs, and soil resources [17]. Cement concrete is a mixture of cement, stone, and water in certain proportions [18]. Using waste concrete to produce recycled concrete can reduce the use of quarried stones and carbon dioxide emissions while ensuring the balance of the ecological environment. Doušová and Ritterman [19] performed ion adsorption experiments in batches by adding concrete mud waste (CSW) at a laboratory temperature of 20°C and observed the experimental data. It was found that the modified concrete mud waste (CSW) enhanced the adsorption selectivity of anions in polluted water bodies, and the percentage of improvement was about 20%.

Governed by the increasing shortage of mineral resources and the concept of green and sustainable road construction, recycling technology has been used in different road structural layers. Many waste concrete blocks are produced in the reconstruction and expansion projects of traditional cement concrete roads, and the recycled aggregates can be obtained by crushing and processing them. Some of its properties can meet the requirements of road aggregate. Using recycled aggregate in the cement-stabilized crushed stone base can ensure the adequate mechanical properties of the base and can promote the recycling of waste mineral resources. However, due to the high crushing value of recycled aggregate and the significant amount of adhered mortar, it is difficult to achieve a breakthrough in improving the aggregate recycling rate.

Many researchers have conducted experimental studies on improving the mechanical properties of cement-stabilized macadam materials. It is believed that the relevant admixture of modifier materials can improve the properties of cement-stabilized macadam to a certain extent. Saccani et al. [20] developed composites using the wastes derived from recycling carbon fiber/epoxy composites. The short fibers were added to the Portland cement, and its processability, porosity, microstructure, and physical and mechanical properties were studied. It was found that the

resulting flexural strength and toughness were improved. Thus, the waste from epoxy resin-carbon fiber composites can be used as reinforcement in building materials.

Recycled aggregate is loose, porous, rough, and light in texture. Part of the aggregate surface has adhered mortar. However, the natural aggregate surface is smooth, and the particle size distribution is uniform [21]. At present, the recycling of waste concrete is the focus of researchers all over the world. Recycled concrete is the most valuable, cost-effective recycling, and the most widely used concrete in research studies [22]. Many researchers have used different proportions of recycled aggregates in concrete, and the resulting physical, mechanical, and durability properties have been studied [23]. Due to the high porosity, low strength, and other inferior properties of recycled concrete, different improvement measures such as mixing ratio, mixing process, and recycled aggregate transformation on the aggregate surface have been suggested, leading to a greater replacement level of natural aggregates with recycled aggregates. The corresponding results have shown satisfactory performance [24]. Recycled cement refers to using limestone in waste concrete as calcium hydride in cement to produce cement clinker or cement mixture, which is added to it [25]. Through the statistics and analysis of Shenzhen's 2010–2015 information data on demolition waste from generation to disposal, Wu et al. [26] found that Shenzhen produces tens of millions of tonnes of construction waste every year and shows a continuous upward trend in the future. Thus, by maximizing the recycling of construction waste, the benefits will be substantial.

A cement-stabilized macadam base is widely used in highway engineering because of its high mechanical strength, durability, frost resistance, and good water stability. Since the strength of brick slag is lower than that of natural stone, the research and applications of construction waste with brick slag as the main component in the cement-stabilized crushed stone base are less. Previous research studies have primarily focused on waste concrete aggregates. However, due to the demolition of a large number of brick-concrete structures, a large amount of brick slag is produced. Therefore, the mixed recycled aggregate containing bricks and pure recycled brick aggregate are taken as the research objects in this study. The reinforcement effect of recycled cement-stabilized aggregate and its influencing factors are analyzed through the mix proportion design and corresponding strength and durability tests. The study serves as the technical support for expanding the applicability of recycled cement-stabilized aggregate.

## 2. Materials and Methods

### 2.1. Materials

*2.1.1. Recycled Aggregate.* The recycled aggregate used in the tests and research was provided by Xuchang Jinke Resources Recycling Co., Ltd. Recycled aggregate used in the study is the waste generated from demolishing old buildings, obtained through crushing, impurity removal, screening, grading, and other treatments. It is mainly composed of concrete, mortar,

and brick aggregate. The proportion of each component is related to the source. If the source is a demolished brick concrete structure, brick aggregate is the main component of recycled aggregate; if the source is another structural type, the brick aggregate composition is relatively small. Brick aggregate mainly comes from sintered clay brick, and its strength is lower than that of concrete aggregate. Since the brick aggregate proportion in recycled aggregate significantly impacts the strength of recycled aggregate, two kinds of recycled aggregate were selected in this study to make the research more meaningful and applicable. One is the mixed recycled aggregate (RC), which is composed of concrete and contains about 20% brick aggregate and mortar, as shown in Figure 1. The other kind of recycled aggregate is the recycled brick aggregate (RB) separated from mixed recycled aggregate, as shown in Figure 2. RB and RC represent recycled aggregate from demolished brick and concrete buildings and other buildings.

Aggregate crushing value is the performance index of aggregate resistance to crushing. It is used to measure the mechanical properties of aggregate. The crushing value test is shown in Figure 3. The test procedure for determining the aggregate crushing value is as follows. Recycled aggregate was sieved, and an aggregate of particle size ranging from 9.5 mm–13.2 mm was oven dried. A 9 kg sample of aggregate was evenly put into the metal cylinder, placed in the press, and was pressurized. It reached 400 kN within 10 minutes. After stabilizing for 5 seconds, the sample was removed and passed through the 2.36 mm sieve. The mass passing through the sieve divided by the total mass multiplied by 100% was obtained, representing the aggregate crushing value. The crushing value reflects the mechanical properties of the aggregate under pressure; that is, the greater the aggregate strength, the lower the crushing value. The crushing value test results are shown in Table 1. The crushing values of RC and RB were found to be 31.8% and 41.9%, respectively, which are lower than the strength of natural gravel and do not meet the strength requirements of aggregate crushing value  $\geq$  30% of class II highways specified in the Technical Guidelines for Construction of Highway Roadbases (JTJ F20-2015). Therefore, without strengthening treatment, these aggregates cannot be used in class II and above highway cement-stabilized macadam bases.

The recycled aggregate from the construction waste recycling company was divided into coarse, medium, and fine aggregates, which were sieved, respectively, to obtain the aggregate gradation, as shown in Table 2.

**2.1.2. The Stabilizing Material.** PO 42.5 cement was used as the stabilizing material for cement-stabilized recycled aggregate. The physical and mechanical properties of cement were tested, and the setting time, stability, strength, and other technical indexes were determined. It can be used for cement-stabilized recycled aggregate mix proportion and strength tests.

**2.1.3. Reinforcing Material.** At present, the strengthening methods of recycled aggregate mainly include chemical and physical strengthening methods. The chemical strengthening method mainly improves the internal defects of the



FIGURE 1: Mixed recycled aggregate.



FIGURE 2: Recycled brick aggregate.

aggregate by soaking it in a suitable concentration of chemical solution to improve the strength of recycled aggregate. In this investigation, through the analysis of the effect of the strengthening test, the immersion strengthening method of polyvinyl alcohol (PVA) solution was tested (Figure 4). PVA is a high molecular polymer with good water solubility. It is soluble in water at high temperatures. Its aqueous solution has good adhesion. Studies have shown that soaking recycled aggregate in PVA solution with a certain concentration and consistency can improve its strength [27]. It is proposed to use the solution prepared from PVA type bp-05 to strengthen the recycled aggregate. The solution prepared from BP-05 PVA is used to strengthen the recycled aggregate.

## 2.2. Experimental Procedures

**2.2.1. Recycled Aggregate Strengthening.** Recycled aggregate is crushed, graded, and sieved during its production process. Some pore cracks might be produced during these processes, resulting in low strength and poor working performance. In order to obtain the best strengthening effect, the recycled aggregate was soaked in different concentrations of PVA and at different soaking times. The aggregate was then dried. The solution infiltrated the cracks and pores of the recycled aggregate and was solidified and hardened to provide a strengthening effect. The best concentration and strengthening time are determined according to the crushing value improvement effect. Then, the physical indexes are measured. SRC and SRB represent reinforced RC and RB.

The strengthening process of recycled aggregate is as follows. First, a PVA solution with a concentration of 6%–12% was prepared. Then, the weighed PVA particles and

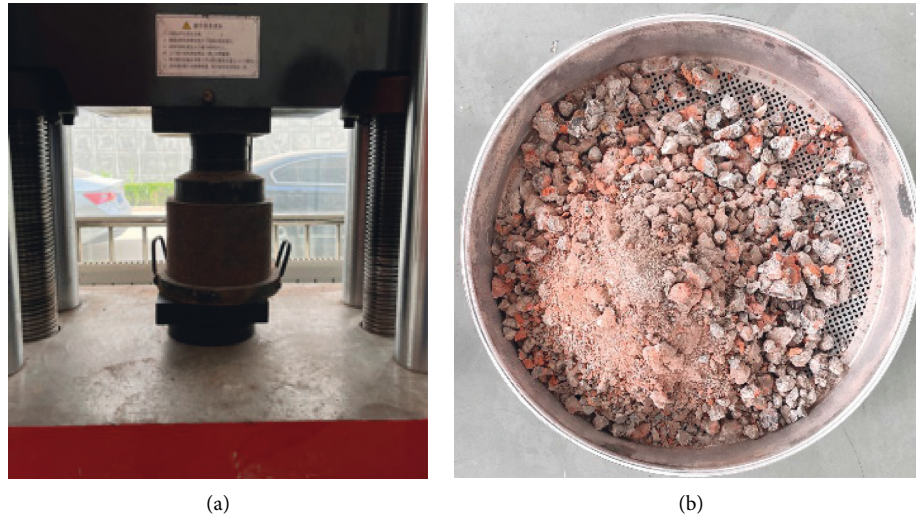


FIGURE 3: Crushing value test. (a) Aggregate crushing and (b) crushed aggregate screening.

TABLE 1: Physical and mechanical indexes of two recycled aggregates before and after strengthening.

Recycled aggregate type	Apparent density		Water absorption		Crushing value	
	Apparent density/kg/m <sup>3</sup>	Compared with before enhancement	Water absorption/%	Compared with before enhancement	Crushing value/%	Compared with before enhancement
SRC	2507	Reduce 1.1%	7.06	Reduce 2.8%	24.59	Reduce 23.0%
SRB	2514	Reduce 5.2%	11.91	Reduce 6.51%	29.40	Reduce 30.1%

TABLE 2: Gradation of three aggregates.

Mesh size/mm	Mass percentage passing through square sieve/%							
	37.5	31.5	19.0	9.50	4.75	2.36	0.6	0.075
Coarse aggregate	100	90.3	42.1	5.2	1.3	1.1	1.0	0
Medium aggregate			100	71.8	32.1	18.2	13.7	0
Fine aggregate				100	98.2	63.5	27.1	11.8

water were poured into a clean iron container, which was subsequently put into an electric blast drying oven for heating. The oven temperature was set to 110°C, and the mixture was heated until PVA was completely dissolved in water. The container containing PVA was taken out, and a mixer was used to stir it to accelerate the dissolution. The prepared recycled aggregate mixture of size more than 5 mm was poured into the PVA solution container, as can be seen in Figure 5, and soaked for 24 h–72 h. After the soaking period, the PVA solution was drained, and the mixture was washed with clean water. The mixture was then put on an iron plate for drying for subsequent use in tests.

**2.2.2. Mix Proportion and Specimen Fabrication.** The design aggregate grading refers to the grading range of cement-stabilized aggregate specified in the construction guidelines. RC and RB are designed with grading A and B, respectively.



FIGURE 4: PVA.



FIGURE 5: PVA solution soaking recycled aggregate.

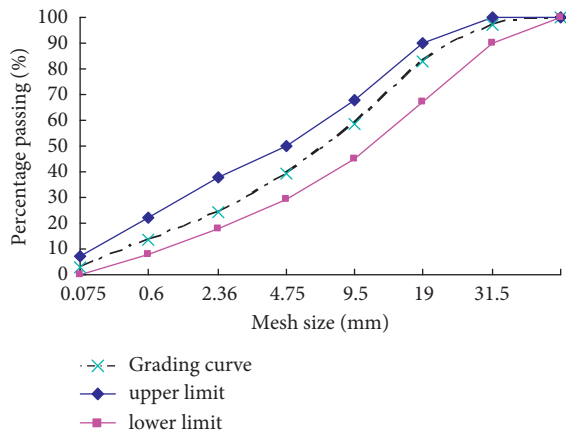


FIGURE 6: Grading RCA.

The proportion of coarse aggregate in grading B is relatively high. Two gradings of RC aggregate (hereinafter referred to as RCA and RCB) are shown in Figures 6 and 7. The proportions of the coarse, medium, and fine aggregates of RCA and RCB are 30%, 45%, and 25% and 40%, 40%, and 20%, respectively. The RB aggregate was screened, and then the aggregates with different particle sizes were selected to prepare aggregates with two grades A and B (hereafter referred to as RBA and RBB), as shown in Figures 8 and 9. The RBA grading curve was close to the median value of the grading range, and the RBB grading curve was close to the lower limit.

According to the design proportion, the recycled aggregate of each particle size was evenly weighed and mixed. Then, half of the required water was added, and the mixture was thoroughly mixed again and allowed to stand for 4 hrs. Cement was subsequently added along with the remaining half of the mixing water. The mixture was evenly mixed again. The duration for each mix was 90 seconds.

The methods of making cement-stabilized macadam specimens include compaction, vibration, and static

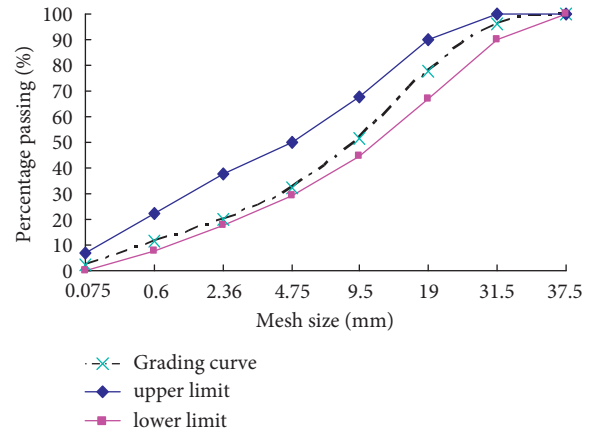


FIGURE 7: Grading RCB.

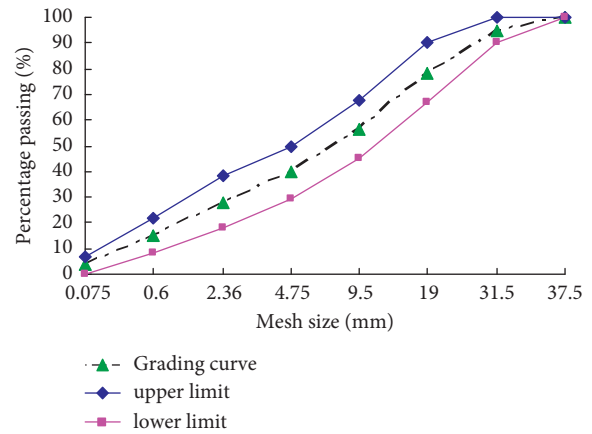


FIGURE 8: Grading RBA.

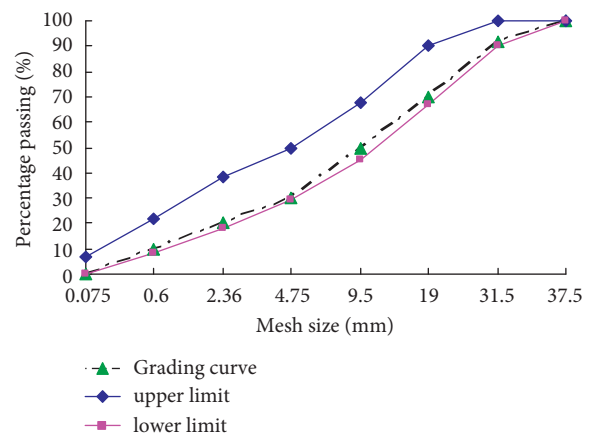


FIGURE 9: Grading RBB.

pressure. The unconfined compression strength test specimens were cylindrical specimens with a diameter and a height of 150 mm. In the beginning, the compaction method was used for molding. It was found that part of the brick aggregate was struck during the compaction process, and the

molded specimens were incomplete. It was easier to form the test piece by vibration, compaction, and static pressure methods, and the integrity of the test piece was better. After comparison, the two methods were used to form the specimens in subsequent tests.

The vibration, compaction, and static pressure methods were used to make the test specimens. The mixture was evenly loaded into the test molds in three layers and gently tamped with a tamping rod. A vibration compactor was used to compact the specimens. The surface pressure and vibration frequency were set as 0.1 MPa and 28–30 Hz, respectively. The universal testing machine was used to apply the static pressure to form the test piece. The loading rate of 1 mm/min (strain-controlled action) was selected. The load was applied until all the specimens were pressed into the mold, and the pressure was maintained for 2 minutes. Afterwards, the specimens were demolded and cured in a standard curing chamber for six days. The specimens were later soaked in water for 24 h. The unconfined compressive strength for 7 days was then subsequently measured.

Four kinds of recycled aggregate were added with 5% PO42.5 cement, respectively, to form four different mixtures. Each mixture was added with mixing water at a 0.5% water consumption interval, and five groups of specimens with different water content were made by vibration compaction and the static pressure method. The water content was measured for the control group, and the corresponding dry density was calculated as a reference for the optimal water content. After the 7 d curing of the specimens with different gradations and moisture contents, the 7 d unconfined compressive strength was measured. The water content of the specimens with the maximum compressive strength was taken as the optimal water content. The test setup is shown in Figure 10.

**2.2.3. Unconfined Compressive Strength Test.** After six days of standard curing and 24 h of immersion in water, the specimens were tested for a 7-day unconfined compressive strength. The test specimens were removed from the water, and the surface water was wiped off. The specimen was placed in the universal testing machine and was aligned with the indenter. Then, the test machine was started to make the indenter of the testing machine come into contact with the specimen. The pressure tester was adjusted to run at 1 mm/min. The pressure was recorded when the specimen started showing damage, and the unconfined compressive strength was calculated. The number of specimens in each group will be at least 3. If the unconfined compressive strength difference of the same group of test pieces was greater than 15%, then double the number of test pieces had to be made and retested. The test process is shown in Figure 11.

**2.2.4. Freeze-Thaw Cyclic Test.** The minimum temperature in winter in Central China is lower than 0°C, and the minimum temperature is about -15°C, which has certain requirements on the frost resistance of pavement base materials. The freeze-thaw test can be used to test the frost resistance of recycled cement-stabilized macadam at low temperatures. After 7 days

of curing, the surface moisture of the test specimens was wiped. The specimens were weighed, measured, and then placed in the freeze-thaw chamber for the freeze-thaw cycles, as shown in Figure 12. In order to adapt to the characteristics of the Central Plains region, the freezing and thawing cycle were set at a low temperature of -18°C, a normal temperature of 20°C, a low temperature of 16 hours, a normal temperature of 8 hours, and a freezing and thawing cycle time of 7 days. Six test specimens in each group were tested, and the number of specimens used for each index test before and after the freeze-thaw cycle was at least three. The test indicators include the unconfined compressive strength of the specimen before and after the freeze-thaw cycle. The strength ratio was calculated, and then the durability of recycled cement-stabilized macadam was evaluated.

### 3. Results

**3.1. Strengthening Effect and Influencing Factors of PVA.** The strength of the two kinds of recycled aggregates soaked in PVA solution of different concentrations with different soaking durations is shown in Figures 13 and 14. Table 1 shows the changes in physical and mechanical properties of recycled aggregate strengthened with the optimal soaking concentration and time.

The test results show that when RC and RB are strengthened with PVA of different concentrations and soaked for different durations, the corresponding strength increases, whereas the crushing value decreases to varying degrees. The optimal soaking concentration of RC and RB is found to be 10%, while the optimal soaking time is determined as 24 h and 60 h, respectively. RB requires a longer soaking time than RC. The crushing values of reinforced RC and reinforced RB are 24.95% and 29.40%, respectively, which meet the strength requirements of cement-stabilized macadam base for heavy traffic class I highways and class II highways, respectively.

**3.2. Strength of Cement-Stabilized Recycled Aggregate.** Unconfined compressive strength is an important index of road performance for cement-stabilized macadam. Highway traffic shows a significant growth trend of overloaded and overweight vehicles, which has become an important factor in pavement structure damage. Therefore, the 7 d unconfined compressive strength of cement-stabilized material base course for the heavy traffic of class I highways and class II highways required in the construction rules are 4 MPa ~5 MPa and 3 MPa ~5 MPa as the strength design goal of cement-stabilized recycled aggregate. The optimum water content is determined according to the principle that the cement-stabilized recycled aggregate made according to the design mix proportion has the best molding effect and the maximum compressive strength. The unconfined compressive strength test results are shown in Table 3.

The unconfined compressive strength test results of cement-stabilized recycled aggregate (before and after strengthening) show that the unconfined compressive strength of cement-stabilized SRC prepared with PO42.5

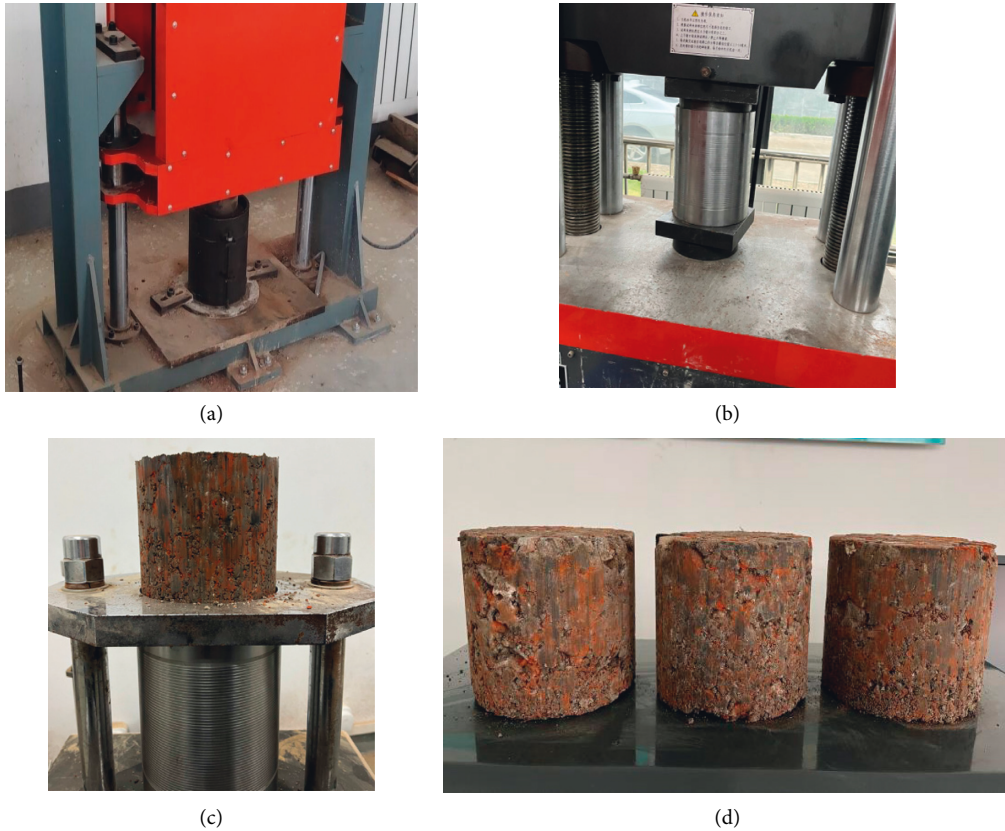


FIGURE 10: Specimen preparation. (a)Vibratory compaction, (b)static pressure, (c) specimen demolding, and (d) specimen after demolding.



FIGURE 11: Unconfined compression test: (a)Unconfined compression test starts and (b)specimen is crushed.

cement meets the design requirements of class I highway. The strength increases by 18%~22% than that of before strengthening. The cement-stabilized RB prepared with PO42.5 cement has low unconfined compressive strength before strengthening, which only meets the class II highway subbase requirements. After strengthening, the strength is increased by 36~39%, which can meet the technical requirements of class II highway heavy traffic base, and the scope of application is expanded. Compared with cement-

stabilized SRC, cement-stabilized SRB has a more significant effect on the strength improvement of the two kinds of recycled aggregates after strengthening treatment. The reason is that compared with recycled concrete aggregate, brick slag has lower strength and larger pores. After PVA solution strengthening treatment, the internal structural defects are filled and strengthened to improve their strength. The effect of cement-stabilized SRB strength improvement is more significant.



FIGURE 12: Freeze-thaw cycle test.

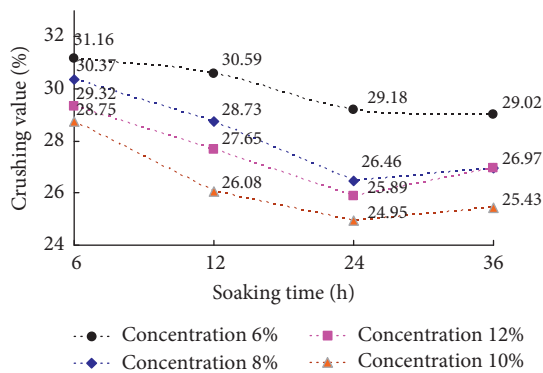


FIGURE 13: Crushing value of SRC.

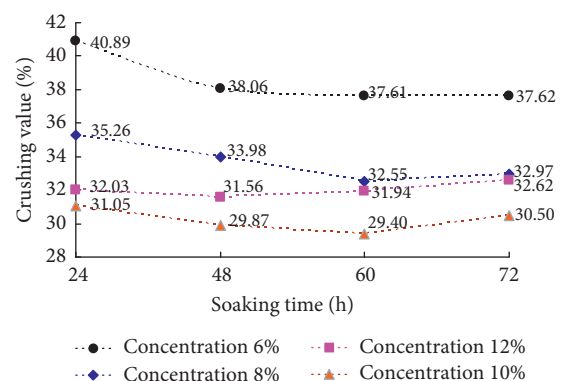


FIGURE 14: Crushing value of SRB.

**3.3. Freeze-Thaw Cyclic Test Results.** The freeze-thaw test can detect the water damage resistance of pavement structures. It is also an important index to evaluate the durability of cement-stabilized macadam. The test specimen of cement-stabilized recycled mixture made by adding 5% cement to grade A aggregate was subjected to the freeze-thaw cycle test. The test results are shown in Table 4.

The test results show that after the freeze-thaw cycle test, the strength loss of the cement-stabilized recycled mixture is less, reaching more than 70% of the design strength, indicating excellent durability. The durability of the cement-stabilized recycled mixture after strengthening is not significantly improved.

#### 4. Discussion

It is seen from the results of the unconfined compressive strength test of unreinforced cement-stabilized recycled aggregate that the optimum moisture content of RCA, RCB, RBA, and RBB specimens made by vibratory compaction and static pressure is the same, which is 11.0%, 10.5%, 16.5%, and 16.0%, respectively. The optimum moisture content of

RBA and RBB was significantly higher than that of RCA and RCB. The optimum moisture content of RCA was slightly higher than that of RCB. The optimum moisture content of RBA was slightly higher than that of RBB. The reason is that the water absorption of brick slag in recycled aggregate is the highest. After adding water and cement, more water will be absorbed during mixing and stewing, so the optimal water content of RCA and RCB is significantly lower than that of RBA and RBB. The larger the particle size of recycled aggregate, the smaller the water absorption in a certain period. Therefore, the optimal water content of RCB and RBB is slightly lower than that of RCA and RBA.

From the unconfined compressive strength test results of reinforced cement-stabilized recycled aggregate, it can be seen that the optimum water content of SRCA, SRCB, SRBA, and SRBB is 10.5%, 10.0%, 15.5%, and 15.0%, respectively. Compared with the recycled cement-stabilized macadam prepared with unreinforced aggregate, the optimum water content decreased in varying degrees, and SRBA and SRBB decreased more, reaching 1%. The reason is that after



TABLE 3: Unconfined compressive strength test results.

Aggregate type	Pressing methods	Optimum water content/%	Maximum unconfined compressive strength/MPa	Aggregate type	Pressing methods	Optimum water content/%	Maximum unconfined compressive strength/MPa
RCA	Vibratory compaction	11.0	3.41	RBA	Vibratory compaction	16.5	2.31
	Static compaction		3.49		Static compaction		2.46
SRCA	Vibratory compaction	10.5	4.08	SRBA	Vibratory compaction	15.5	3.13
	Static compaction		4.25		Static compaction		3.41
RCB	Vibratory compaction	10.5	3.38	RBB	Vibratory compaction	16.0	2.18
	Static compaction		3.39		Static compaction		2.34
SRCB	Vibratory compaction	10.0	4.01	SRBB	Vibratory compaction	15.0	3.06
	Static compaction		4.07		Static compaction		3.19

TABLE 4: Freeze-thaw cycle test results.

Mixture type	Test piece without freeze-thaw cycle		Test specimen after 7-day freeze-thaw cycles	
	Unconfined compressive strength $R_0$ (MPa)		Unconfined compressive strength $R_3$ (MPa)	Strength ratio = $R_3/R_0$ (%)
RCA	3.49		2.85	81.7
SRCA	4.25		3.37	79.3
RBA	2.46		1.98	80.5
SRBA	3.41		2.68	78.6

soaking in PVA solution, the pores of recycled aggregate are filled, the water absorption of aggregate is reduced after condensation, and the water consumption is reduced. The brick in recycled aggregate has the highest water absorption, the strength of the brick is low, and it is easier to produce more microcracks in the crushing process. Therefore, the optimal water content of SRBA and SRBB is significantly higher than that of SRCA and SRCB. The larger the particle size of recycled aggregate, the smaller the water absorption in a certain period. Therefore, the optimal water content of SRCB and SRBB is slightly lower than that of SRCA and SRBA.

The unconfined compressive strength test results of the cement-stabilized recycled aggregate of the same type and different gradations show that cement-stabilized RC and RB are within the upper and lower gradation limits. Also, the strength of the gradation composition close to the lower limit is slightly lower. Since the recycled aggregate has large pores, the internal structural defects are filled and strengthened after the PVA solution strengthening treatment. This is why the strength has significantly improved. Grade A, which is close to the median value of the grading range, is similar to the dense suspension structure, while grade B, which is close to the lower limit, is similar to the dense skeleton structure. The coarse aggregate content in

dense suspension structures is less, and its strength mainly comes from the binding of cement and fine aggregate. The dense skeleton structure contains a large amount of coarse aggregate, and their strength is mainly composed of the impaction of coarse aggregate and the cementation of cement and fine aggregate. Due to the low strength of recycled coarse aggregate-containing bricks, the skeleton function of the structure is insufficient. The aggregate is crushed by vibratory compaction and static pressure forming, which impacts the strength.

The comparison of the strengths of cement-stabilized recycled aggregate formed by different forming methods reveals that the strength of the specimen made by static pressure forming is higher than that by vibration forming. In constructing a cement-stabilized macadam base, the compaction process includes initial compaction  $\rightarrow$  re-compaction  $\rightarrow$  final compaction. Static pressure, vibration compaction, and static pressure are adopted, respectively, which is more than the single forming method in the laboratory. In theory, the compaction effect is better, and it should not be lower or even higher than the strength of the test specimen made by the single static pressure or vibration forming method in the laboratory. Therefore, the strengthening scheme obtained in the laboratory can be applied in road engineering.

## 5. Conclusions

The following conclusions can be drawn from the study on the strengthening method of recycled aggregate and the grading, mix proportion design, strength, and durability test of cement-stabilized recycled aggregate.

- (1) After the recycled aggregate is strengthened by PVA solution, the strength is improved to a certain extent, and RB is more significantly improved than RC.
- (2) When RB and RC are stabilized by cement, the optimum moisture content of the former is higher than that of the latter; the optimum moisture content of grade A is slightly lower than that of grade B.
- (3) After PVA strengthening treatment, the strength of RC and RB can meet the requirements of aggregate for the cement-stabilized crushed stone base of heavy traffic class I highways and class II highways. Moreover, relatively higher strengths can be obtained by adopting grade A and the static pressure method.
- (4) After the freeze-thaw cycle test, the strength loss of the stabilized recycled aggregate is small, and the durability is good; the durability of recycled aggregate is not significantly improved after strengthening.

## Data Availability

The data supporting the current study are given in the article.

## Conflicts of Interest

The authors declare that there are no conflicts of interest.

## Acknowledgments

The authors would like to acknowledge financial support from the Henan Science and Technology Research Project of China (Grant no. 18102310746).

## References

- [1] M. Bendixen, I. Overeem, M. T. Rosing et al., "Promises and perils of sand exploitation in Greenland," *Nature Sustainability*, vol. 2, no. 2, pp. 98–104, 2019.
- [2] M. D. Gavriletea, "Environmental impacts of sand exploitation. Analysis of sand market," *Sustainability*, vol. 9, no. 7, p. 1118, 2017.
- [3] Y. Li, L. Liu, C. Liu, J. Sun, Y. Ye, and Q. Chen, "Sanding prediction and sand-control technology in hydrate exploitation: a review and discussion," *Marine Geology Frontiers*, vol. 32, no. 7, pp. 36–43, 2016.
- [4] N. Wu, Y. Li, Q. Chen et al., "Sand production management during marine natural gas hydrate exploitation: review and an innovative solution," *Energy & Fuels*, vol. 35, no. 6, pp. 4617–4632, 2021.
- [5] Q. Yin, J. Y. Wu, Z. Jiang et al., "Investigating the effect of water quenching cycles on mechanical behaviors for granites after conventional triaxial compression," *Geomechanics and Geophysics for Geo-Energy and Geo-Resources*, vol. 8, no. 2, p. 77, 2022.
- [6] A. Koutamanis, B. van Reijn, and E. van Bueren, "Urban mining and buildings: a review of possibilities and limitations," *Resources, Conservation and Recycling*, vol. 138, pp. 32–39, 2018.
- [7] K. Specht, R. Siebert, I. Hartmann et al., "Urban agriculture of the future: an overview of sustainability aspects of food production in and on buildings," *Agriculture and Human Values*, vol. 31, no. 1, pp. 33–51, 2014.
- [8] M. Carpio, J. Roldán-Fontana, R. Pacheco-Torres, and J. Ordóñez, "Construction waste estimation depending on urban planning options in the design stage of residential buildings," *Construction and Building Materials*, vol. 113, pp. 561–570, 2016.
- [9] M. Arora, F. Raspall, L. Cheah, and A. Silva, "Buildings and the circular economy: estimating urban mining, recovery and reuse potential of building components," *Resources, Conservation and Recycling*, vol. 154, Article ID 104581, 2020.
- [10] V. W. Tam and C. M. Tam, "A review on the viable technology for construction waste recycling," *Resources, Conservation and Recycling*, vol. 47, no. 3, pp. 209–221, 2006.
- [11] E. O. Wong and R. C. Yip, "Promoting sustainable construction waste management in Hong Kong," *Construction Management & Economics*, vol. 22, no. 6, pp. 563–566, 2004.
- [12] M. Z. Gao, B. G. Yang, J. Xie et al., "The mechanism of microwave rock breaking and its potential application to rock-breaking technology in drilling," *Petroleum Science*, vol. 19, no. 3, pp. 1110–1124, 2022.
- [13] J. Solís-Guzmán, M. Marrero, M. V. Montes-Delgado, and A. Ramírez-de-Arellano, "A Spanish model for quantification and management of construction waste," *Waste Management*, vol. 29, no. 9, pp. 2542–2548, 2009.
- [14] A. A. Kadir and A. Mohajerani, "Bricks: an excellent building material for recycling wastes—a review," in *Proceedings of the IASTED International Conference On Environmental Management And Engineering (EME 2011)*, pp. 4–6, Calgary, AB, Canada, July, 2011.
- [15] F. Xu, M. Zhou, J. Chen, and S. Ruan, "Mechanical performance evaluation of polyester fiber and SBR latex compound-modified cement concrete road overlay material," *Construction and Building Materials*, vol. 63, pp. 142–149, 2014.
- [16] R. Lukpanov, D. Dyusembinov, Z. Shakhmov, D. Tsygulov, Y. Aibuldinov, and N. I. Vatin, "Impregnating compound for cement-concrete road pavement," *Crystals*, vol. 12, no. 2, p. 161, 2022.
- [17] E. K. Anastasiou, A. Liapis, and I. Papayianni, "Comparative life cycle assessment of concrete road pavements using industrial by-products as alternative materials," *Resources, Conservation and Recycling*, vol. 101, pp. 1–8, 2015.
- [18] N. T. Chuc, L. T. Van, and B. I. Bulgakov, "Designing the composition of concrete with mineral additives and assessment of the possibility of cracking in cement-concrete pavement," *Materials Science Forum*, vol. 931, pp. 667–673, 2018.
- [19] B. Doušová and P. Riterman, "Recycling of powdered building wastes in environmental technologies," *Proceedings of the SGEM*, vol. 19, 2019.
- [20] A. Saccani, S. Manzi, I. Lancellotti, and L. Lipparini, "Composites obtained by recycling carbon fibre/epoxy composite wastes in building materials," *Construction and Building Materials*, vol. 204, pp. 296–302, 2019.

- [21] C. S. Poon and D. Chan, "The use of recycled aggregate in concrete in Hong Kong," *Resources, Conservation and Recycling*, vol. 50, no. 3, pp. 293–305, 2007.
- [22] V. W. Tam, C. M. Tam, and Y. Wang, "Optimization on proportion for recycled aggregate in concrete using two-stage mixing approach," *Construction and Building Materials*, vol. 21, no. 10, pp. 1928–1939, 2007.
- [23] V. W. Tam, M. Soomro, and A. C. J. Evangelista, "A review of recycled aggregate in concrete applications (2000–2017)," *Construction and Building Materials*, vol. 172, pp. 272–292, 2018.
- [24] J. M. Khatib, "Properties of concrete incorporating fine recycled aggregate," *Cement and Concrete Research*, vol. 35, no. 4, pp. 763–769, 2005.
- [25] J. Xiao, W. Li, Y. Fan, and X. Huang, "An overview of study on recycled aggregate concrete in China (1996–2011)," *Construction and Building Materials*, vol. 31, pp. 364–383, 2012.
- [26] H. Wu, H. Duan, L. Zheng, J. Wang, Y. Niu, and G. Zhang, "Demolition waste generation and recycling potentials in a rapidly developing flagship megacity of South China: prospective scenarios and implications," *Construction and Building Materials*, vol. 113, pp. 1007–1016, 2016.
- [27] S. C. Kou and C. S. Poon, "Properties of concrete prepared with PVA-impregnated recycled concrete aggregates," *Cement and Concrete Composites*, vol. 32, no. 8, pp. 649–654, 2010.